UTS UNIVERSITY OF TECHNOLOGY SYDNEY

Precise Indoor Positioning With Sensor Fusion of Ultra-Wideband and Odometer

by Ang Liu

Thesis submitted in fulfilment of the requirements for the degree of

Doctor of Philosophy

under the supervision of Dr Jianguo Wang and Dr Xiaoying Kong

University of Technology Sydney
Faculty of Engineering and Information Technology

January 2025

Certificate of Original Authorship

I, *Ang Liu*, declare that this thesis is submitted in fulfilment of the requirements for the award of *Doctor of Philosophy*, in the School of Civil and Environmental Engineering, Faculty of Engineering and IT, at the University of Technology Sydney.

This thesis is wholly my own work unless otherwise referenced or acknowledged. In addition, I certify that all information sources and literature used are indicated in the thesis.

This document has not been submitted for qualifications at any other academic institution.

This research is supported by the Australian Government Research Training Program.

Signature:

Production Note:
Signature removed prior to publication.

Date: 16/1/2025

Dedication

For my family, who have always fully supported and loved me.

Acknowledgements

During my PhD journey, I have received countless kindnesses and help. First of all, I would like to thank my supervisor, Dr. Janguo Wang, who has been a very responsible supervisor in giving me valuable advice on my academic research. His academic rigour and seriousness will always be an example for me. I would also like to thank my co-supervisor, Dr Xiaoying Kong, whose support has allowed me to start my academic journey. Her wise advice and invaluable assistance at many turning points in my life have enabled me to make the right choices at critical moments. I am deeply grateful to my supervisory panel for their generosity and patience in guiding me in my growth and development. I would also like to thank my research collaborator, Dr Shiwei Lin, for her smart advice, which often inspired me when I hit a bottleneck in my research. Thanks to Professional editor Dr John McAndrew for copyediting and proofreading services.

I would like to thank the love of my life, Ms. Yu Zhang, for being with me all the way. Her love was like a warm light that supported me through the dark moments. No matter the challenges, she was always by my side, giving me strength and courage. Her understanding and encouragement are the pillars of my perseverance, and I am deeply grateful for her selfless dedication and consistent love.

My sincerest thanks go to my parents, Mr. Yongsheng Liu and Mrs. Jing Zhang, who never gave up on me and supported me unreservedly. They have taught me responsibility, optimism, and strength. Their selfless love and endless encouragement allow me to move forward steadfastly in the face of challenges. Also, thanks to Mrs Tingting Liu for taking so much external pressure off me so that I could concentrate on my research. Mr Loki, you made me realise the purest trust and beauty in the world.

List of Publications

Related to the Thesis:

1. **A. Liu**, S. Lin, X. Kong, J. Wang, G. Fang, and Y. Han, "Development of low-cost indoor positioning using mobile-UWB-anchor-configuration approach," in *Parallel Architectures, Algorithms and Programming (PAAP 2020),* Shenzhen, China: Singapore: Springer, 2021, pp. 34-46.

2. **A. Liu**, S. Lin, J. Wang, and X. Kong, "A method for non-line of sight identification and delay correction for UWB indoor positioning," in *The 17th IEEE Conference on Industrial Electronics and Applications (ICIEA 2022),* Chengdu, China: IEEE, 2022.

3. **A. Liu**, S. Lin, J. Wang, and X. Kong, "A succinct method for non-line-of-sight mitigation for ultra wideband indoor positioning system," *Sensors*, vol. 22, no. 21, 2022, DOI: 10.3390/s22218247.

4. **A. Liu**, S. Lin, J. Wang, and X. Kong, "A novel loosely coupling fusion approach of ultra-wideband and wheel odometry for indoor localisation," *Electronics*, vol. 12, no. 21, p. 4499, 2023.DOI:10.3390/electronics12214499.

5. **A. Liu**, S. Lin, J. Wang, and X. Kong, " A tightly coupled UWB and wheel odometry based on a dynamic UKF for Indoor Localisation," *Electronics*, vol. 13 Issue 8 p. 1518, 2024. DOI: 10.3390/electronics13081518

Others:

6. S. Lin, **A. Liu**, J. Wang, and X. Kong, "A review of path-planning approaches for multiple mobile robots," *Machines*, vol. 10, no. 9, p. 773, 2022. [Online]. Available: https://www.mdpi.com/2075-1702/10/9/773.

7. S. Lin, X. Kong, J. Wang, **A. Liu**, G. Fang, and Y. Han, "Development of a UAV path planning approach for multi-building inspection with minimal cost," in *Parallel and Distributed Computing, Applications and Technologies (PDCAT 2020)*, Shenzhen, China, Springer International Publishing, 2021, pp. 82-93.

8. S. Lin, X. Kong, J. Wang, and **A. Liu**, "Helix-HPSO approach for UAV path planning in a multi-building environment," *Journal of Reliable Intelligent Environments*, vol. 9, no. 4, p. 371, Nov. 2022, DOI: 10.1007/s40860-022-00196-z.

9. S. Lin, **A. Liu**, J. Wang, and X. Kong, "An intelligence-based hybrid PSO-SA for mobile robot path planning in warehouse," *Journal of Computational Science*, vol. 67, p. 101938, Mar. 2023, DOI: https://doi.org/10.1016/j.jocs.2022.101938.

10. S. Lin, **A. Liu**, X. Kong, and J. Wang, "Development of swarm intelligence leader-Vicsek-model for multi-AGV path planning," in *2021 20th International Symposium on Communications and Information Technologies (ISCIT)*, Tottori, Japan, IEEE, 2021, pp. 49-54, DOI: 10.1109/ISCIT52804.2021.9590578.

11. S. Lin, **A. Liu**, and J. Wang, "A dual-layer weight-leader-Vicsek model for multi-AGV path planning in warehouse," *Biomimetics*, vol. 8, no. 7, p. 549, 2023.

12. J. Wang, S. Lin, and **A. Liu**, "Bioinspired perception and navigation of service robots in indoor environments: A review," *Biomimetics,* vol. 8, no. 4, p. 350, 2023.

13. S. Lin, **A. Liu**, J. Wang, and X. Kong, "An improved fault-tolerant cultural-PSO with probability for multi-AGV path planning," *Expert Systems with Applications*, vol. 237, p. 121510, 2024.

Table of Contents

List of Figures

List of Tables

Glossary

AGV	Automatic guided vehicle
AOA	Angle-of-arrival
BLE	Bluetooth low energy
CIR	Channel impulse response
DDF	Dynamic dimension fusion
DS-TWR	Double-sided two-way ranging
EKF	Extended Kalman filter
FCC	Federal Communications Commission
GNSS	Global navigation satellite system
GPS	Global positioning system
HDOP	Horizontal dilution of precision
IMU	Inertial measurement unit
IoT	Internet of Thing
IPS	Indoor positioning system
IVMs	Imported vector machines
KF	Kalman filter
KNN	K-nearest neighbour
LOS	Line-of-sight
LSTM	Long and short-term memory
MB-OFDM	Multi-band orthogonal frequency division multiplexing
MEMS	Micro-electromechanical system
MIL	Multiple-input learning
ML	Maximum likelihood
NLOS	Non-line-of-sight
OLS	Ordinary least squares
PF	Particle filter

RF	Radio frequency
RHA	Relative heading angle
RMSE	Root mean square error
RNN	Recurrent neural networks
RSSI	Received signal strength indicator
SS-TWR	Single-sided two-way ranging
SVM	Support vector machine
TDOA	Time difference of arrival
TOA	Time-of-arrival
TOF	Time-of-flight
TWR	Two-way ranging
UKF	Unscented Kalman filter
UWB	Ultra-wideband
VR	Virtual reality
WLLS	Weighted linear least squares
WLS	Weighted least squares

Abstract

Ultra-wideband (UWB) is a promising indoor positioning technology with high accuracy and low energy consumption. The current research uses UWB, assisted by wheeled odometers, to develop a stable centimetre-level indoor positioning system (IPS) to address smart industry needs.

The research initially investigates the limitations of UWB-only IPS and identifies non-line-of-sight (NLOS) errors caused by signal occlusion as the primary factor affecting positioning accuracy. The main goal of this research phase is to identify and reduce NLOS errors accurately. We propose a sliding window algorithm that can identify about 90% of NLOS errors by this very simple algorithm in a very harsh experimental environment. This algorithm can accurately identify NLOS by analyzing only the variation of ranging values within a sampling window without analysing parameters such as signal strength or channel impulse response (CIR). The algorithm is simple and can be applied to most UWB devices. Additionally, we present a method for modelling NLOS errors induced by walls based on wall thickness, material properties, and UWB signal incidence angle to mitigate such errors effectively within room structures. Experimental verification demonstrates that accurate identification and modelling of NLOS errors can significantly improve UWB-only IPS accuracy under NLOS conditions close to line-of-sight (LOS) levels. Furthermore, our research explores strategies to reduce the cost of UWB hardware in large-area scenario applications by proposing a method to convert fixed anchors into moving ones.

In flexible, variable, and complex indoor environments, achieving accurate positioning with UWB alone is difficult. This research combines low-cost wheeled odometers and UWB to form a multi-sensor fusion localisation system. We proposed a loosely coupled method that fuses UWB and odometry. The first step

is to identify the NLOS using the sliding window method and then optimise the positioning of the UWB system by deleting ranges that contain NLOS errors. Finally, the absolute position of the optimised UWB is selected to correct the cumulative error in the direction and displacement of the odometer for precise positioning. The fused system can achieve a positioning accuracy of less than 10 cm RMSE in complex environments. Loose coupling requires subsystems to realise localisation independently, which may not be possible for UWB systems in harsh NLOS environments, affecting the fused system's accuracy. The final phase of the research proposes a tight coupling method based on the dynamic Unscented Kalman filter (UKF), which assists the UWB in identifying and mitigating the NLOS errors and calculates the Horizontal dilution of precision (HDOP) value through the position information provided by the odometer. The parameters and inputs of the UKF are dynamically adjusted according to the NLOS state, HDOP value, and motion state to achieve stable and accurate positioning with RMSE less than 10 cm in strong NLOS environments.

1. Chapter 1 Introduction

1.1 Research Background and Objectives

Eighty per cent of human work and life occurs in indoor environments [1]. With the development of science and technology in recent decades, smart devices, including wearable devices [2], autonomous mobile robots, virtual reality (VR), and other technologies have greatly facilitated people's lives. At the same time, applying robots in smart factories and smart warehouses in the industry can improve production efficiency and reduce production costs. Using unmanned equipment in other dangerous scenarios, such as indoor fire rescue and mine rescue, can also improve the rescue efficiency and reduce the risk [3-5]. These technologies and scenarios are realised based on high-precision indoor positioning systems (IPSs).

An outdoor environment global navigation satellite system (GNSS) can provide the target location information. For example, the commonly used global positioning system (GPS) has a wide range of applications in the military, for agricultural use, vehicle positioning, and other fields [6]. However, GNSS is not suitable for indoor environments. In indoor environments, which often require high accuracy, the obstruction of buildings to the communication between the satellite and the terminal equipment leads to a large positioning error. Researchers are exploring new techniques and algorithms to achieve centimetre-level positioning accuracy in indoor environments.

A review paper [7] defines an indoor position system (IPS) as a system that achieves accuracy within 3 metres at a range of 20 metres. An IPS is usually judged by accuracy, robustness, cost, energy consumption, and coverage.

Common IPS solutions are classified into non-radio frequency and radio frequency (RF) technologies, depending on the sensors used. Non-radio frequency includes IMU, LiDAR, ultrasonic sensors, and cameras. RF technologies use wireless communication technologies, such as UWB, Wi-Fi, Bluetooth, and RFID [8]. The advantages of LiDAR or Camera are that it can realise map building, obstacle identification, and path planning, but its positioning accuracy is highly related to hardware costs. At the same time, WiFi, Bluetooth, and RFID accuracy is difficult to achieve at the centimetre level. The main purpose of this study is to realise a low-cost centimetre-level positioning system, so UWB becomes the preferred sensor in this study. The odometer has the advantages of low cost, simple structure and high short-term accuracy, which makes it very suitable as the auxiliary sensor of UWB.

According to the analysis in a review paper [9], UWB is a low-cost, sub-metre accuracy, and multipath-resistant sensor, compared with other methods, which is well suited for constructing high-precision IPS. The complexity of indoor environments causes IPS to face greater challenges than outdoor positioning [10]. Walls, tables, chairs, and even human bodies can be obstacles, and the relative positions of these obstacles and the target to be localised often change, increasing the randomness of the errors. The disadvantages of UWB IPS in such complex indoor environments are also obvious. The principle of UWB IPS is similar to that of GPS, which is based on measuring the distance between a target tag and several fixed anchors to achieve the tag's localisation. The range information is calculated by measuring the time-of-flight (TOF) of the signal between the tag and the anchor points [11]. When an obstacle between a tag and a fixed anchor point in a UWB system obscures the line of sight (LOS) communication, the measured range value contains a non-line of sight (NLOS) error. This NLOS error results in the measured range value being tens of centimetres or even metres larger than the real distance, greatly affecting the positioning accuracy. Therefore, how to

identify and mitigate the effect of NLOS error on positioning accuracy is an important and current research topic in UWB IPS.

This research project aims to construct a low-cost, high-precision IPS based on UWB that can stably achieve centimetre-level positioning in complex indoor environments, especially when affected by NLOS. The specific objectives of this research are as follows:

1. Develop a UWB IPS deployment scheme to reduce hardware costs.
2. Propose a simple, fast and accurate algorithm to identify which ranges are affected by NLOS errors in UWB-only IPS systems.
3. Propose modelling of NLOS errors caused by walls and achieve centimetre-level positioning accuracy in UWB-only IPS without sufficient LOS measurements.
4. Propose a loose-coupling approach to fuse UWB and a wheeled odometer to improve the positioning accuracy and robustness of the system when UWB is affected by NLOS.
5. Propose a dynamic UKF tight-coupling approach to fuse UWB and wheeled odometers to achieve stable centimetre-level positioning under strong NLOS errors.

1.2 Thesis Structure

Figure 1.1 shows the structure of the research. Chapter 2 is a literature review of UWB IPS, including the advantages and disadvantages of UWB IPS, localisation algorithms, and the fusion of UWB with other sensors proposed by other researchers. Chapter 3 is an improvement scheme for UWB-only IPS, including the identification algorithm for NLOS error, the mitigation of NLOS error using the wall error model to improve the positioning accuracy and a UWB IPS positioning system with movable anchors. In Chapter 4, a loosely coupled

algorithm is proposed to improve the positioning accuracy of IPS by fusing wheeled odometers under the influence of strong NLOS errors in UWB. In Chapter 5, based on the previous work, a dynamic UKF tight-cornering algorithm is proposed to identify and correct the NLOS of the UWB system by the odometer. At the same time, the cumulative error of the odometer is corrected by using the range information of the UWB. The proposed system can provide centimetre-level positioning accuracy even in a strong NLOS environment with only one LOS anchor point. Chapter 6 summarises the project and gives directions for future research. The following is a detailed overview of the chapters.

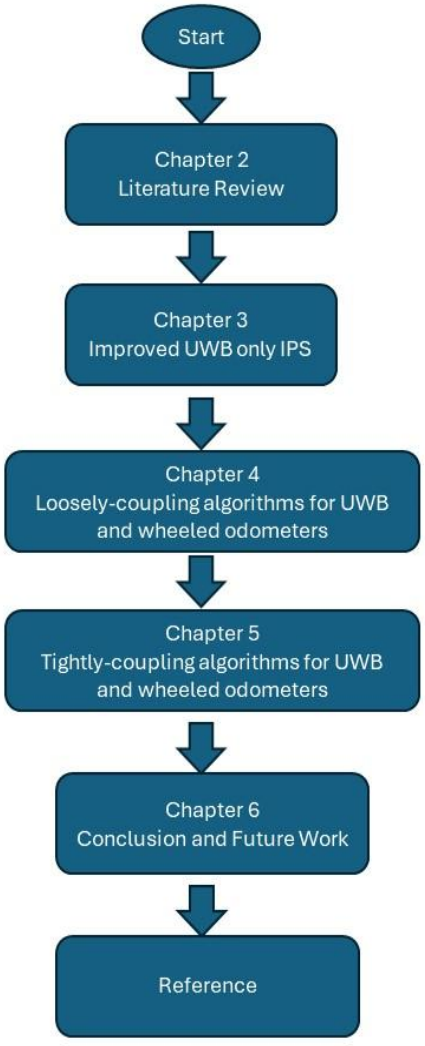

Figure 1.1 Thesis structure

1.2.1 Overview: Chapter 2 Literature Review

With the rapid development of the Internet of Things (IoT), robotics and wearable devices, researchers have been working to improve the accuracy and robustness of indoor IPSs. UWB has the advantages of high accuracy, low energy consumption, and high multipath resolution. It is considered one of the important future development directions of indoor positioning. This chapter firstly introduces the advantages and disadvantages of UWB IPS, including the identification and mitigation of NLOS errors; secondly, it introduces the commonly used positioning algorithms of UWB IPS, including time-of-arrival (TOA), time difference of arrival (TDOA) and angle-of-arrival (AOA); thirdly, it introduces the algorithms for combining UWB with other sensors and accuracy comparison; finally, it proposes that the identification and mitigation of NLOS errors are crucial to improve the positioning accuracy of UWB IPS, and this problem can be solved effectively by multi-sensor fusion.

1.2.2 Overview: Chapter 3 Improved UWB-Only IPS

This chapter on the study of UWB-only IPS is divided into three parts:

1. UWB has a centimetre-level positioning accuracy for indoor use and is one of the most promoted indoor positioning technologies. However, when a wall or other objects block UWB signals, NLOS happens, which reduces the signal-noise ratio and causes signal transmission delay. As NLOS introduces large distance measurement errors, UWB positioning accuracy is dramatically degraded. Because the appearance of NLOS causes abrupt changes in the ranging values, this section proposes a simple and accurate algorithm for identifying NLOS. The NLOS between a UWB anchor and a moving tag is identified by analysing the variance of the change of UWB measured distance in adjacent samples.

A 2D delay estimation model corrects the NLOS distance error caused by walls. Experimental results show that UWB NLOS identification accuracy can reach more than 90%, and the delay estimation model can effectively correct distance measurement errors and make positioning accuracy with NLOS appearance comparable to the LOS situation.

2. Building on the previous part of the study, in this part, the wall model is further upgraded to 3D, and a weight calculation model is proposed to give different weights to the ranging values in different cases by NLOS identification. All the distance measurements, including LOS and NLOS, are used to calculate the mobile UWB tag position with ordinary least squares (OLS) or weighted least squares (WLS). Experimental results show that with correct NLOS indentation and the delay model, the proposed method can achieve positioning accuracy in NLOS environments close to the level of LOS. Compared with OLS, WLS can further optimise the positioning results. Correct NLOS indentation, accurate delay model, and proper weights in the WLS are the keys to accurate UWB positioning in NLOS environments.
3. UWB communication distance is limited, and obstacles easily block the signal. When UWB IPS is used in large indoor environments, such as factories and airports, it must be installed with many fixed anchors to ensure positioning accuracy. In this section, a mobile-UWB-anchor-network approach is proposed for the first time. We change the fixed anchors in the UWB system into moving anchors to reduce the number of anchors in the area and the cost of the system. This new approach is verified using experiments.

1.2.3 Overview: Chapter 4 Loosely-Coupling Algorithms for UWB and Wheeled Odometers

As mentioned, UWB systems promise centimetre-level accuracy for indoor positioning, yet they remain susceptible to NLOS errors due to complex indoor environments. A fusion mechanism that integrates the UWB with an odometer

sensor is introduced to address this challenge and achieve a high positioning accuracy. A sliding window method is applied to identify NLOS anchors effectively. The modified UWB-only positioning has an average error under 13 cm with an RMSE of 16 cm. Then, a loosely coupled approach named dynamic dimension fusion (DDF) is designed to mitigate the odometer's cumulative errors, achieving a remarkable average error and RMSE of around 7 cm, notably superior to established unscented Kalman filter (UKF) fusion techniques. DDF utilises UWB data to correct the one-dimensional heading error of the odometer when the robot moves in a straight line and to correct both heading and distance travelled in two dimensions when the robot is turning. Comprehensive real-world experimental evaluations underscore the efficacy and robustness of this novel approach.

1.2.4 Overview: Chapter 5 Tightly-Coupling Algorithms for UWB and Wheeled Odometers

UWB has attracted significant attention among the various technologies in IPSs due to its centimetre-level accuracy. However, the precision of UWB positioning is severely compromised by NLOS conditions arising from complex indoor environments. Conversely, wheel odometry exhibits a simple structure and has witnessed substantial improvements in accuracy and sampling frequency with advancements in optoelectronic technology, rendering it widely applicable to indoor wheeled robots. This study proposes a tightly coupled and dynamic UKF fusion method that utilises odometry to assist in identifying and mitigating NLOS effects on UWB systems while introducing horizontal dilution of precision (HDOP) as a measure for assessing the impact of geometric distribution between robots and UWB anchors on accuracy. The proposed method dynamically adjusts UKF parameters based on NLOS identification, HDOP values, and robot motion status to achieve optimal positioning results. By employing this fusion method, effective mitigation of NLOS impact on UWB systems can be achieved along with

reduced cumulative errors in odometry measurements. Remarkably, high-precision positioning can be attained even when only one LOS anchor point is available within the UWB system. Experimental verification conducted under severe NLOS conditions demonstrates that the fused system's RMSE reaches approximately 7cm. Furthermore, robustness and accuracy are maintained even when LOS anchor points continuously change within the UWB system.

1.2.5 Overview: Chapter 6 Conclusion and Future Work

This chapter focuses on summarising this research project and suggesting future research directions.

1.3 Contributions and Publications

1.3.1 Main Contributions and Publications

Chapter 3 presents a variety of algorithms, including a mobile anchor point method to reduce hardware costs, an NLOS recognition algorithm, a wall error correction model in 2D and 3D, and a weighted positioning algorithm. Related publications are as follows.

- A. Liu, S. Lin, X. Kong, J. Wang, G. Fang, and Y. Han, "Development of low-cost indoor positioning using mobile-UWB-anchor-configuration approach," in *Parallel Architectures, Algorithms and Programming*, (PAAP 2020), Shenzhen, China, Singapore: Springer, 2021, pp. 34-46.
- A. Liu, S. Lin, J. Wang, and X. Kong, "A method for non-line of sight identification and delay correction for UWB indoor positioning," in *The 17th IEEE Conference on Industrial Electronics and Applications (ICIEA 2022),* Chengdu, China: IEEE, 2022, pp. 9-14.
- A. Liu, S. Lin, J. Wang, and X. Kong, "A succinct method for non-line-of-sight mitigation for ultra wideband indoor positioning system," *Sensors*, vol. 22, no. 21, 2022, DOI: 10.3390/s22218247.

Chapter 4 proposes a new DDF algorithm to fuse wheel odometry and UWB in a loose-coupling method to improve the positioning accuracy and robustness of the system in real and variable indoor environments. Relevant publications are as follows:

- Liu, S. Lin, J. Wang, and X. Kong, "A novel loosely coupling fusion approach of ultra-wideband and wheel odometry for indoor localisation," *Electronics*, vol. 12, no. 21, p. 4499, 2023.

Based on the research problems in the previous section, Chapter 5 proposes a method of fusion of UWB and a wheeled odometer through dynamic UKF so that the system can provide accurate positioning even when there is only one LOS anchor point, and the algorithm dynamically adjusts the UKF through the different states of the ranging value so that the system can achieve centimetre-level positioning accuracy.

- Liu, S. Lin, J. Wang, and X. Kong, " A tightly coupled UWB and wheel odometry based on a dynamic UKF for Indoor Localisation," *Electronics*, vol. 13 Issue 8 p. 1518, 2024.

1.3.2 Additional Research Contributions

The research contributions in this section are mainly as a team member in path planning for single and multiple robots in indoor environments, providing accurate localisation support during experiments, and as a co-author in reviewing and revising relevant publications. The publications are as follows:

- S. Lin, X. Kong, J. Wang, A. Liu, G. Fang, and Y. Han, "Development of a UAV path planning approach for multi-building inspection with minimal cost," in *Parallel and Distributed Computing, Applications and Technologies (PDCAT 2020)*, Shenzhen, China, Singapore: Springer International Publishing, 2021, pp. 82-93.

- S. Lin, X. Kong, J. Wang, and A. Liu, "Helix-HPSO approach for UAV path planning in a multi-building environment," *Journal of Reliable Intelligent Environments*, vol. 9, no. 4, p. 371, Nov. 2022, DOI: 10.1007/s40860-022-00196-z.

- S. Lin, A. Liu, J. Wang, and X. Kong, "An intelligence-based hybrid PSO-SA for mobile robot path planning in warehouse," *Journal of Computational Science*, vol. 67, p. 101938, Mar. 2023, DOI: https://doi.org/10.1016/j.jocs.2022.101938.

- S. Lin, A. Liu, X. Kong, and J. Wang, "Development of swarm intelligence leader-Vicsek-model for multi-AGV path planning," in *2021 20th International Symposium on Communications and Information Technologies (ISCIT)*, Tottori, Japan, IEEE, 2021, pp. 49-54, DOI: 10.1109/ISCIT52804.2021.9590578.

- S. Lin, A. Liu, and J. Wang, "A dual-layer weight-leader-Vicsek model for multi-AGV path planning in warehouse," *Biomimetics*, vol. 8, no. 7, p. 549, 2023.

- J. Wang, S. Lin, and A. Liu, "Bioinspired perception and navigation of service robots in indoor environments: A review," *Biomimetics,* vol. 8, no. 4, p. 350, 2023.

- S. Lin, A. Liu, J. Wang, and X. Kong, "An improved fault-tolerant cultural-PSO with probability for multi-AGV path planning," *Expert Systems with Applications*, vol. 237, p. 121510, 2024.

2. Chapter 2 Literature Review

2.1 Introduction

The widespread adoption of smart devices in recent years has brought both convenience and challenges in terms of technology. The emergence of the IoT and robotics has significantly increased the number of devices that can be accessed indoors. These devices include personal smartphones, wearable devices [2], floor-cleaning robots, AGVs, and location tags used in various industrial contexts, such as intelligent warehousing, smart grids, and smart hospitals. These devices are used to manage people in complex indoor environments. Accurate location tracking is crucial for safely operating these devices within a room [12]. The significance of indoor positioning is evident in various applications. Firstly, it can aid in navigation within complex indoor environments, like airports, hospitals, and shopping malls, providing convenience to people's lives. Secondly, it can be helpful in emergency and safety applications [3], such as locating people in building fires [4] and mines [5], resulting in shorter rescue response times. In addition, IPSs are crucial for intelligent management systems, such as smart warehouses [13], that can track the location of parcels and AGV [14]. Providing real-time location information not only increases efficiency but also reduces costs. Furthermore, accurate location information is essential for emerging wearables, virtual reality, and augmented reality markets, as it enhances user interaction. However, providing stable centimetre-level positioning in complex indoor environments remains a significant challenge and a research goal at this stage.

The GNSS has been refined over decades to provide accurate positioning in most outdoor environments, typically within a margin of error of a few meters. However, buildings can obstruct satellite signals in complex indoor environments, leading to signal fading, multipath, and NLOS errors. As a result,

the accuracy of GNSS positioning is seriously degraded, and it is impossible to achieve high positioning accuracy in indoor environments using GNSS [15]. Therefore, researchers are actively exploring the use of other sensors to achieve stable centimetre-level positioning accuracy in indoor environments.

Indoor positioning technologies utilise sensors to determine a device's or user's location within indoor spaces [16]. As mentioned, these technologies can be categorised into two groups based on the type of sensors used. The first group includes non-radio frequency technologies, such as IMU, LiDAR, ultrasonic sensors, and cameras. The second group includes wireless communication technologies, such as UWB, Wi-Fi, and Bluetooth [8].

Both different sensors have their advantages and disadvantages. For example, the IMU can output position information without relying on external information. However, while the positioning accuracy of IMU is high in the short term, the measurement error accumulates over time, causing the IMU to drift over a long period [17, 18]. LiDAR technology can produce a comprehensive map of the surrounding environment and accurately locate the carrier [19]. However, harsh weather conditions, such as rain, snow, fog, and dust, can cause scattering or absorption of laser pulses, thus reducing accuracy in outdoor environments [20-23]. Although indoor environments reduce the interference of these factors, it is essential to note that glass in indoor environments can severely affect the accuracy of LiDAR.

RF-based indoor positioning techniques tend to provide greater coverage and lower cost. For example, Wi-Fi and Bluetooth hardware costs are very low, and fingerprint-based algorithms can also provide target location information, but accuracy is difficult to reach at the centimetre level [24-27]. RFID is cheaper but is usually used in situations that only need to identify the target object's

presence and do not require high positioning accuracy, such as people and object management. Achieving centimetre-level accuracy in RFID positioning is still a challenge [28].

UWB technology was initially developed for military use in radar, imaging, and high-speed communications. In 2002, the U.S. Federal Communications Commission (FCC) approved the limited commercial use of UWB [29]. As semiconductor technology evolved over the same period, UWB transceiver designs were improved, resulting in reduced size, lower power consumption, and improved ranging accuracy, enhancing the applicability of UWB for precise indoor positioning. Mainstream companies in different industries have begun to apply UWB technology in their latest products. Apple, Samsung [30] and other companies use UWB for spatial sensing and positioning in their smart terminals, and BMW and other automobile manufacturers use digital keys installed with UWB chips [31].

UWB operates over a wide frequency range, typically between 3.1 GHz and 10.6 GHz, so the data transmission rate of UWB will also be very high [32, 33]. Based on MB-OFDM (multi-band orthogonal frequency division multiplexing) communication technology, the UWB communication rate is expected to reach 480 Mbit/s [34].

UWB technology employs sporadic pulse signalling for data transmission, characterised by notably brief pulse durations typically ranging from 0.2 to 1.5 nanoseconds. This attribute significantly contributes to the minimisation of system power consumption. In comparison to conventional wireless devices, the power requirements of civilian UWB devices are markedly lower, approximating merely 1% of that of mobile phones and around 5% of Bluetooth devices. In a seminal study conducted by Zhao [35], a UWB transmitter was

developed, exhibiting both low power consumption and high data transmission rates. The findings from Zhao's experimental research indicated that the maximum power consumption of this UWB transmitter, when operating at a transmission rate of 250 Mbps, was a mere two milliwatts, with the energy expenditure per pulse recorded at only eight picojoules. Consequently, UWB devices demonstrate substantial superiority over other wireless technologies in terms of battery longevity and reduced electromagnetic radiation emissions.

At the same time, this wide bandwidth provides high resolution in time-domain measurements, enabling UWB systems to resolve multipath components efficiently and accurately determine the TOF of signals [36]. The commonly used ranging-based positioning algorithms are TOA, TDOA, and AOA. Although UWB can also calculate position information by fingerprinting algorithms, the positioning accuracy will be degraded to a similar level to Wi-Fi Bluetooth, so fingerprinting algorithms are not usually used [36].

Based on the review and analysis of recent literature, this chapter is structured as follows. Section 2.2 discusses the fundamentals of UWB ranging algorithms. Section 2.3 discusses positioning algorithms typically used in UWB systems. Section 2.4 focuses on identifying and mitigating the effects of NLOS errors. Section 2.5 discusses the multi-sensor systems in which UWB is fused with other sensors.

2.2 UWB Ranging Principle

Accurate measurement of the distance between a tag and a fixed anchor point is the foundation of UWB IPS, and this section introduces several well-known algorithms for UWB ranging. The fundamental principle underlying UWB ranging involves determining distance by measuring the TOF of the signal

between the anchor and tag, which is then multiplied by the speed of light, as articulated in Equation 2.1.

$$\boldsymbol{d_n = t_{TOF} * C} \qquad (\mathbf{2.1})$$

where $\boldsymbol{t_{TOF}}$ is the TOF of the signal, $\boldsymbol{C}$ is the speed of light, and $\boldsymbol{d_n}$ is the distance between the anchor and tag.

2.2.1 Single-Sided Two-Way Ranging

Single-sided two-way ranging (SS-TWR) is a simple ranging method that calculates the distance by counting the time of flight of the signal for one round trip between the tag and the anchor point. This is shown in Figure 2.1.

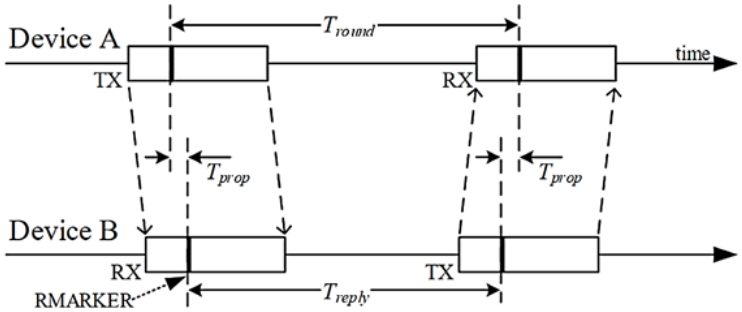

Figure 2.1 SS-TWR [37]

The following equation calculates the TOF of the signal.

$$\boldsymbol{t_{ToF}} = \frac{\boldsymbol{t}_{\text{round}} - \boldsymbol{t}_{\text{reply}}}{\mathbf{2}} \qquad (\mathbf{2.2})$$

where $\boldsymbol{t}_{\text{round}}$ is the time needed for this round of communication, $\boldsymbol{t}_{\text{reply}}$ is the time interval between receiving the message and replying on the receiving end.

This method uses the local clocks of the tags and anchors when calculating the time difference by subtraction, so it requires strict clock synchronisation of all anchors and tags within the system. However, the clock offsets of each device are different, which can greatly affect the accuracy of the distance measurement. Even a time error of 1 ns can result in a range error of 30 cm when multiplied by the speed of light [38]. Therefore, this method is difficult to use in practice.

2.2.2 Double-Sided Two-Way Ranging

In order to solve the problem of SS-TWR, which is difficult to achieve clock synchronisation, the algorithm of double-sided two-way ranging (DS-TWR) has been proposed, which calculates the time of flight by measuring the back and forth of the two rounds of signals at the tag and anchor points. Figure 2.2 demonstrates DS-TWR using four messages.

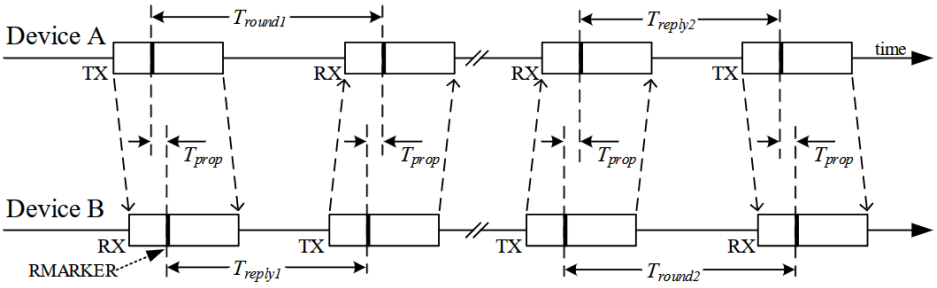

Figure 2.2 DS-TWR with four messages [37]

DS-TWR requires that both the tag and the anchor point act as the sender and the receiver of the signal for one complete round of communication, and this method reduces the requirement of clock synchronisation between different devices. Based on the above method, the communication steps can be further simplified. As shown in Fig. 2.3, the reply of the first communication is sent as the start of the second communication so that only three messages are needed to complete the DS-TWR.

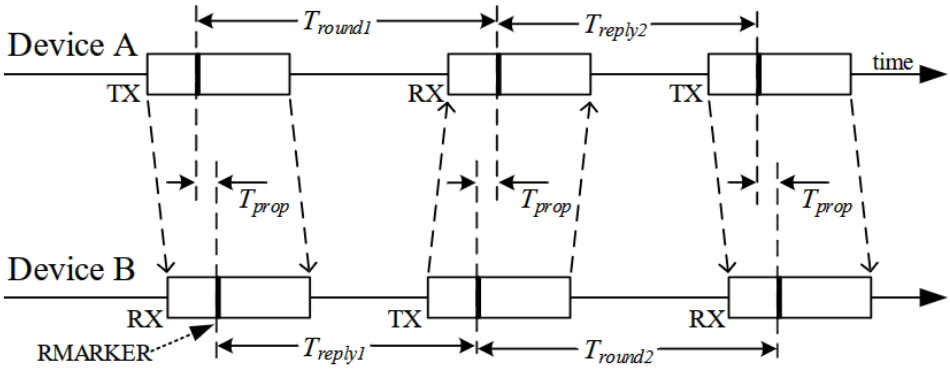

Figure 2.3 DS-TWR with three messages [37]

Regardless of whether three or four messages are used, there are two complete communications between the tag and the anchor point, and the time of flight of the signals can be calculated using Equation 2.2 below.

$$t_{\text{ToF}} = \frac{\left(t_{\text{round 1}} \times t_{\text{round 2}} - t_{\text{reply 1}} \times t_{\text{reply 2}}\right)}{\left(t_{\text{round 1}} + t_{\text{round 2}} + t_{\text{reply 1}} + t_{\text{reply 2}}\right)} \quad (2.3)$$

Through this calculation method, strict time synchronisation between the tag and the anchor point is no longer required, greatly improving the UWB's practicality and significantly reducing the distance measurement error. In Decawave's description of its DW1000 chip, it is claimed that even if the clock difference between the two devices is 20 ppm, the range error calculated by the DS-TWR method is only 2.2 mm at a distance of 100 m [37].

2.3 Positioning Algorithms

This section introduces several positioning algorithms commonly used in indoor positioning, including triangulation based on the range principle, including TOA, TDOA, and AOA. And the fingerprint algorithm.

2.3.1 TOA

As illustrated in Figure 2.4, the TOA algorithm entails the tag communicating with multiple base stations and measuring the signal's TOF. At least three anchor ranges are required to determine the tag's position in a two-dimensional (2D) plane. However, an additional set of ranges is necessary to ascertain the vertical dimension or height of the tag.

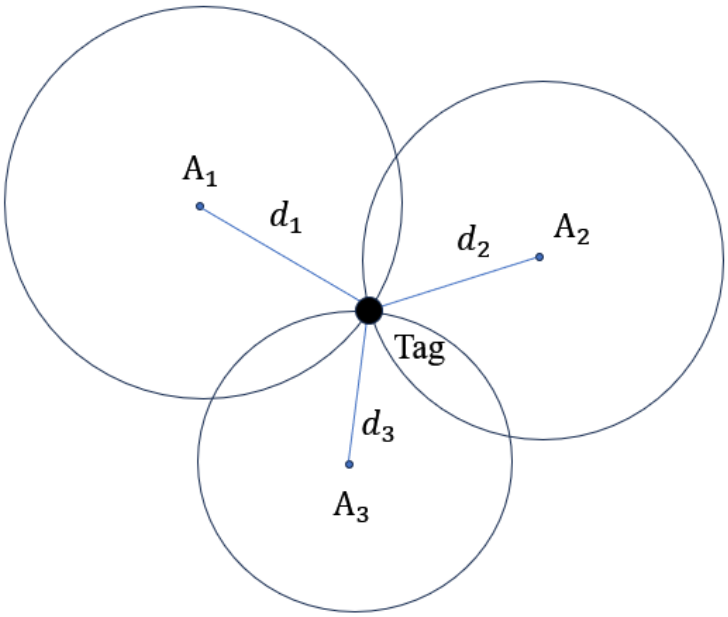

Figure 2.4 TOA

Equation 2.4 describes the relationship between the range, base station coordinates, and tag coordinates [39].

$$\boldsymbol{d_i = \sqrt{(x_i - x)^2 + (y_i - y)^2 + (z_i - z)^2} + \varepsilon} \qquad (\mathbf{2.4})$$

where $\boldsymbol{x_i = [x_i, y_i, z_i]^T}$ represents the known base station coordinates, $\boldsymbol{d_i}$ represents the corresponding range value, $\boldsymbol{x = [x, y, z]^T}$ represents the tag coordinates to be calculated, and $\boldsymbol{\varepsilon}$ is the distance measurement error.

In an ideal state where the ranging error is equal to zero, these circles will intersect at a point that is the exact position of the tag. However, in the real state, due to the presence of ranging error, these circles will intersect in a region [40, 41]. The algorithms used to find the most probable position of the tag from the intersecting region are least squares (LS), maximum likelihood (ML) and weighted linear least squares (WLLS). Krishnaveni et al. [42] pointed out that ML and WLLS are the two algorithms with higher localisation accuracy by

comparing experimental results. The TOA algorithm requires all tags and anchors to be time synchronised, which requires more costly hardware and higher energy consumption [43, 44].

2.3.2 TDOA

TDOA calculates the target coordinates by using the time difference of the signal arriving at different receiving ends [45]. It is mainly based on the hyperbolic principle. The distance difference between the target and anchor points can be calculated by the time difference between the UWB signal reaching different anchor points. According to the distance difference, a hyperbola with these anchor points as the focus and the distance difference as the long axis can be drawn. When there are four known anchor points, three sets of hyperbola can be drawn, and the intersection of the three sets of hyperbola is the position of the target point. The principle of TDOA is shown in Figure 2.5 below.

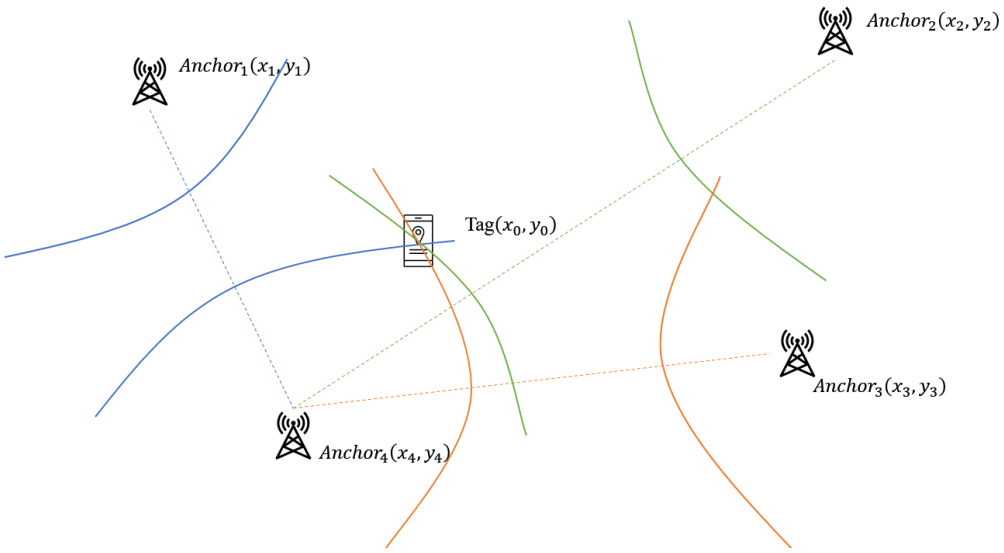

Figure 2.5 TDOA

The UWB anchor coordinates are Anchor $_1(\boldsymbol{x_1}, \boldsymbol{y_1})$, Anchor $_2(\boldsymbol{x_2}, \boldsymbol{y_2})$, Anchor $_3(\boldsymbol{x_3}, \boldsymbol{y_3})$, Anchor $_4(\boldsymbol{x_4}, \boldsymbol{y_4})$. t1, t2, t3, and t4, respectively, represent the time when the UWB signal sent by the tag reaches the four anchor points;

C represents the speed of light. The following three sets of equations can be obtained from the hyperbola properties. The coordinates of the target point (x_0, y_0) can be calculated by the following equations.

$$\begin{aligned}
&\sqrt{(x_0 - x_1)^2 + (y_0 - y_1)^2} - \sqrt{(x_0 - x_4)^2 + (y_0 - y_4)^2} = C(t_1 - t_4) \\
&\sqrt{(x_0 - x_2)^2 + (y_0 - y_2)^2} - \sqrt{(x_0 - x_4)^2 + (y_0 - y_4)^2} = C(t_2 - t_4) \\
&\sqrt{(x_0 - x_3)^2 + (y_0 - y_3)^2} - \sqrt{(x_0 - x_4)^2 + (y_0 - y_4)^2} = C(t_3 - t_4)
\end{aligned} \tag{2.5}$$

The most significant advantage of TDOA is that there is no need for reciprocating communication between the tag and the anchor point. The tag only needs to transmit a UWB signal to each anchor point. In this way, the number of communications for one positioning is significantly reduced, and energy consumption is also reduced. Moreover, TOA requires synchronisation between the transmitter and receiver, whereas TDOA only requires synchronisation between the receivers, making TDOA easier to implement and more accurate [46].

2.3.3 AOA

The core of the AOA system is the antenna array, which usually consists of two or more antenna arrays distributed at different locations. When applied to UWB IPS, the UWB signals from the tag to different anchor points will have different times or phases. These differences can be used to calculate the angle of arrival of the signal, and after obtaining multiple angles of arrival, the geometric relationship can be used to calculate the position of the tag. Figure 2.6 shows a simplified AOA algorithm in 2D space.

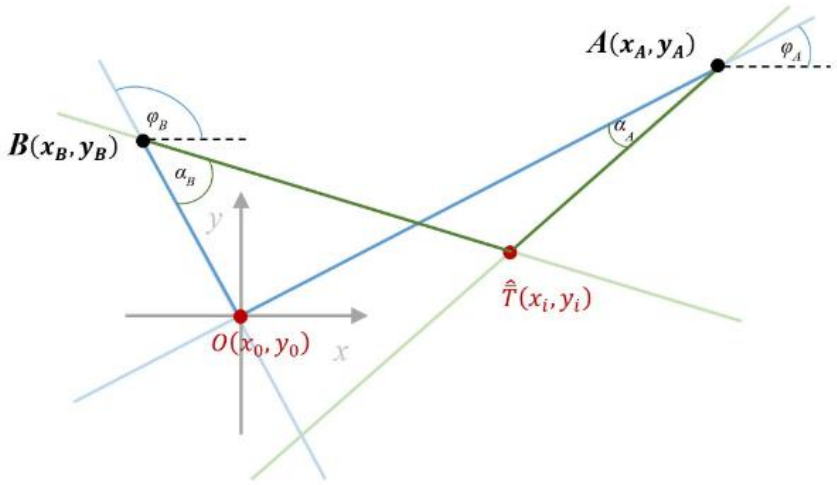

Figure 2.6 AOA [47]

In Equations 2.6 and 2.7, $\boldsymbol{\varphi_A}$ and $\boldsymbol{\varphi_B}$ are the calibration angles between the abscissa or horizontal axis, O ($\boldsymbol{x_0}$, $\boldsymbol{y_0}$) is the calibration point, and A and B represent two fixed-position antennas.

$$\boldsymbol{\varphi_A = \tan^{-1}\frac{y_A - y_0}{x_A - x_0}} \qquad (\mathbf{2.6})$$

$$\boldsymbol{\varphi_B = \tan^{-1}\frac{y_B - y_0}{x_B - x_0}} \qquad (\mathbf{2.7})$$

Each antenna array will provide the angle of arrival of the signal ($\boldsymbol{\alpha_A}$ ***and*** $\boldsymbol{\alpha_B}$), the tag coordinates can be calculated using Equation 2.8 [48].

$$\begin{bmatrix} \boldsymbol{x_i} \\ \boldsymbol{y_i} \end{bmatrix} = \begin{bmatrix} \boldsymbol{\tan(\alpha_A + \varphi_A)} & \boldsymbol{-1} \\ \boldsymbol{\tan(\alpha_B + \varphi_B)} & \boldsymbol{-1} \end{bmatrix}^{-1} \begin{bmatrix} \boldsymbol{x_A \cdot \tan(\alpha_A + \varphi_A) - y_A} \\ \boldsymbol{x_B \cdot \tan(\alpha_B + \varphi_B) - y_B} \end{bmatrix} \qquad (\mathbf{2.8})$$

Establishing a positioning system using the AOA algorithm usually requires multiple antennas that can provide the signal's angle of arrival, increasing the hardware cost. Accurate antenna array calibration is important for an AOA system and requires regular maintenance, as minor timing differences can seriously affect positioning accuracy. Most importantly, in complex indoor

environments, NLOS and multipath effects can significantly impact the angle of arrival of the signals, resulting in large errors in positioning [49]. The experimental results of Xinning et al. [50] show that the root square error is still 21cm with the proposed three-dimensional (3D) LS positioning technique. For some precise indoor positioning needs, this error is still unacceptable.

2.4 NLOS Identification and Mitigation

In UWB IPS, regardless of whether the positioning algorithms are based on ranging or the signal's angle of arrival, the error caused by NLOS is an important factor affecting positioning accuracy. The difficulty of the indoor environment is caused by the complexity of the objects in the positioning space, including fixed walls and movable people, tables, and chairs [51]. Moreover, the occlusion of the signal by these objects can lead to different degrees of error. In our experimental measurements, the NLOS caused by the human body usually increases the measurement distance by several tens of centimetres, while the error caused by a concrete wall or an iron gate can even exceed 1 m. The identification and mitigation of NLOS errors are essential for high-precision UWB IPS.

Identifying NLOS errors and mitigating the effects of such errors are often two consecutive steps. The methods summarised in the literature can be broadly classified into three categories: channel impulse response (CIR), ranging, and other sensor-assisted approaches.

The first method involves analysing the CIR of UWB signals. The principle of the technique is that NLOS conditions significantly change the characteristics of the CIR compared to LOS conditions. In LOS conditions, the energy of the first path is much larger than the delay path, but when NLOS is present and

most of the paths are delayed, this difference is reduced. NLOS and LOS scenarios can be distinguished by examining parameters such as amplitude, delay, and signal shape. Recent advances have seen the combination of various machine learning algorithms to improve the effectiveness of this approach. For example, as reviewed in the literature [52], deep learning techniques can recognise complex patterns indicative of NLOS conditions in CIR data.

Similarly, K-nearest neighbours (KNNs), support vector machines (SVMs) [53], and imported vector machines (IVMs) [54] provide powerful frameworks for the classification of signal features to more accurately identify NLOS situations. However, these methods require a large workforce and time for feature extraction and parameter adjustment [55]. Moreover, CNN [52] is known for sophisticated proficiency in handling spatial data and does not need to manually extract and adjust the feature parameters [56, 57]. Literature [58] proposed an NLOS recognition method based on a multiple-input learning (MIL) neural network model. Through experiments, it is verified that the recognition accuracy of NLOS errors caused by five kinds of objects, including wooden doors, concrete walls, metal plates, the human body, and glass windows, is about 90%, while the positioning accuracy of 7.35cm is obtained by using the WLS method.

The second method for identifying NLOS is based on distance measurement. Under NLOS conditions, the propagation path of UWB signals changes due to signal reflection and diffraction, resulting in an increased flight time and distance measurement. Effective identification of NLOS can be achieved by employing statistical techniques, such as outlier detection algorithms and probability models. For instance, Dwek [59] successfully selected distance measurements with less than 50cm error in 70% of cases using an outlier detection algorithm based on confidence intervals and threshold values.

Literature [60] proposed a methodology for NLOS identification by analysing the residuals of distance measurements and constructing a weighted matrix to enhance accuracy under NLOS conditions.

Furthermore, advancements in artificial intelligence algorithms have facilitated the recognition of abnormal distance data. SVM, for example, can handle high-dimensional data and perform classification tasks effectively. SVM can be trained to extract features from distance data, such as signal strength, arrival time, and signal-to-noise ratio, to identify NLOS errors. Reference [61] achieved a 94% probability of correctly identifying NLOS using SVM while reducing distance measurement errors by 10%. In reference [62], a combination approach involving SVM and CNN analysis was employed to recognise and mitigate NLOS signals through parameter analysis, including distance measurements, noise levels, and measurement errors. CNN can continuously improve its detection capabilities through continuous learning in new NLOS scenarios, enhancing its classification accuracy and flexibility.

The final approach involves utilising assisted sensors to identify and mitigate NLOS, leveraging the benefits of various sensing technologies to compensate for UWB system limitations in NLOS scenarios. IMUs, optical sensors, or LiDAR can provide a more comprehensive understanding of the surrounding environment and motion, enabling more accurate recognition of NLOS. Sensor fusion algorithms can integrate these different data sources to produce more precise position estimates and correct UWB measurement errors caused by NLOS. In reference [63], SVM analyses acceleration and velocity information from IMU and ranging information from UWB to detect NLOS, and improved EKF and LS algorithms achieve positioning accuracy up to 9 cm. Additionally, SLAM technology (especially optical or LIDAR data) enhances the system's real-time environment mapping. In reference [64], combining LIDAR-SLAM with UWB through tight coupling forms an IPS that identifies NLOS using point

cloud maps from LIDAR; then, the position is computed by a localisation model, achieving positioning accuracy as high as 0.094m while improving the robustness of the system. Multi-sensor fusion systems offer better accuracy and stability; fusing different kinds of sensors enables UWB to overcome challenges posed by NLOS for a versatile IPS.

2.5 Multi-Sensor Fusion for UWB

Each type of sensor possesses its inherent advantages and disadvantages, and the approach of multi-sensor fusion capitalises on the complementary strengths of diverse sensing technologies to establish a more robust positioning system. This section is divided into two parts: the first introduces some commonly employed sensors for forming a fusion system with UWB, and the second describes widely used sensor fusion algorithms.

2.5.1 Sensors Fused with UWB

IMU

With the emergence of MEMS (micro-electromechanical system) technology, integrating mechanical components, sensors, and electronics on a single microchip has significantly reduced in size and weight. This miniaturisation, combined with streamlined manufacturing processes, has substantially decreased the cost of IMUs, enabling their utilisation in a broader range of applications. MEMS IMUs' compactness and ability to continuously provide carrier pose data have rendered them indispensable for indoor navigation systems, particularly in scenarios involving small carriers like robotic platforms, AGVs (automatic guided vehicles), and personal wearable devices. Both traditional and MEMS-based IMUs rely on the fundamental principle of combining orthogonally arranged accelerometers and gyroscopes. Accelerometers measure 3D linear acceleration, while gyroscopes track angular

velocity to offer information about carrier direction and speed. Although IMU boasts advantages, such as high sampling frequency and short-term positioning accuracy, it is prone to drift errors if left uncorrected over time, leading to degradation in positioning accuracy.

Due to its self-sustained nature, the IMU is widely preferred as a complementary sensor in multi-sensor fusion systems. Consequently, numerous researchers have utilised IMUs and UWBs to establish an IPS. In reference [65], a complementary Kalman filter fusion method is proposed, which enhances positioning accuracy by adaptively adjusting the weights of measurements from UWBs, magnetometers, and accelerometers through adaptive algorithms. The experiments are conducted in both LOS and mild NLOS environments, demonstrating improved accuracy and trajectory smoothness. Following this algorithm, the residuals of the four UWB anchor points range between 10 to 20 cm. Literature [66] presents an adaptive extended Kalman filter based on the dynamic weight function (DWF-MAEFF) strategy for fusing IMUs and UWBs to locate UGVs; experiments simulate NLOS conditions through occasional occlusion of UWB anchor points. Results indicate that although the accuracy is 60% higher than that achieved with the adaptive extended Kalman filter approach, errors persist at approximately 15-20cm in both east and north directions. In reference [67], the error-state Kalman filter (ESKF) is employed to enhance the accuracy of an IMU/UWB IPS system within a real mine environment; positioning accuracy within 10cm is achieved despite slight NLOS interference.

Odometer

Common odometers include wheeled, inertial, visual, and laser odometers [68]. Wheeled odometers are extensively utilised in UGVs and small-wheeled robots. They consist of a code disc with evenly spaced cutouts flanked by optical and electrical signal sensors. The disc is coaxially mounted with the wheel and rotates

along with it, enabling the optical sensors to detect variations in light passing through the cutouts on the disc. These variations are then converted into electrical signals represented as pulses associated with wheel rotation [69, 70]. This mechanism facilitates precise tracking of the wheel's motion, which is crucial for accurate indoor navigation and localisation.

Wheeled odometers have received limited attention from researchers compared to other methods due to hardware limitations and challenges, such as wheel slippage and surface texture variations, which can affect measurement accuracy. The literature proposes the dynamic window-based PF (DWBPF) algorithm [68] to mitigate cumulative error in odometers and the impact of NLOS on UWB, claiming a positioning accuracy of 0.06m. To address difficulties in identifying errors, like skidding in wheeled odometers, researchers often incorporate additional sensors, such as the fusion of three sensors: odometer, UWB, and IMU. Odometers offer more direct and prompt speed information compared to inertial measurement units (IMUs), reducing integration errors caused by IMUs. The fusion system achieves localisation accuracies of 0.13m and 0.26m in 3D space using TOA and AOA algorithms for UWB, respectively [71]. Another study employing these three sensors utilises an extended Kalman filter (EKF) for fusion, claiming a high accuracy with root mean square error (RMSE) equal to 3.29cm [72]. However, this accuracy is based on full LOS conditions for UWB mentioned in the literature; even when only UWB is present under similar circumstances, the accuracy achieves 4.66cm.

Cameras

Cameras for indoor positioning have attracted significant attention in recent years. Compared to conventional sensors, such as IMU and odometry, cameras provide a more comprehensive perception of the surrounding environment.

Various camera types, including monocular, stereo, RGB-D, and fisheye, are available based on precision and cost requirements [73].

Visual SLAM maps the surrounding environment and locates the carrier using feature points, corners, or edges. However, it offers a lower sensor cost than LiDAR [74]. The camera provides the system with more detailed image information, which can be combined with artificial intelligence technology to recognise the surrounding environment better. CNNs [75-78] have demonstrated significant potential in enhancing the accuracy and reliability of feature point extraction. Moreover, R-CNNs or recurrent neural networks (RNNs) [79, 80] can better understand the surrounding scene, improving system localisation accuracy and enabling more reliable map optimisation during closed-loop detection. In visual odometry, RNNs, long and short-term memory (LSTM) networks, or transformer-based models can be effectively employed for modelling camera motion over time, resulting in more precise motion estimation [80, 81]. Deep learning models hold promise for facilitating semantic mapping creation by generating context-aware maps with richer information [82, 83].

IMUs are also usually needed when forming an IPS with a camera and a UWB. Reference [84] combines a monocular camera, six IMUs and only one uwb anchor to form an IPS by tight coupling, which has achieved 10 to 20 cm positioning accuracy in several experimental validations. The literature [85] uses a resilient tightly coupling approach combining three sensors: stereo camera, IMU, and UWB, and experimentally validates it in a flat and an office scenario, both of which achieve a positioning error of about 10 cm. The experiments show that the absolute position provided by the UWB is instrumental in vision system failures, closed-loop detection and suppression of drift errors.

Wi-Fi and Bluetooth

Wi-Fi and Bluetooth are both RF-based positioning. Wi-Fi employs the IEEE 802.11 wireless local area network standard for data transmission in indoor environments [86]. Wi-Fi operates in the 2.4GHz and 5GHz bands, each with distinct characteristics. Bluetooth technology was initially designed to enable personal local area networks with low power consumption and data communication rates [87] using the IEEE 802.15.1 standard, operating within the frequency range of 2.402GHz to 2.480GHz. Bluetooth low energy (BLE) possesses several advantages, such as low power consumption, cost-effectiveness, extended communication range, prolonged lifespan, compact size, and a simplified communication protocol [88], making it suitable for deployment in small-scale carriers. Additionally, Bluetooth supports mesh network topologies that facilitate collaboration among multiple devices to expand coverage, rendering it an ideal choice for large-scale implementation in extensive indoor environments [89].

There are also many research findings on using Wi-Fi or Bluetooth with UWB to form a fused positioning system. Reference [90] utilises the ML approach for fused positioning based on RSS features for both Wi-Fi and UWB, which has an RMSE of 94cm for positioning in realistic experiments. Reference [91] uses a fingerprinting algorithm, UWB and BLE integrated by EKF, to locate people in a real flat environment, with an average localisation error of around 0.6m. Literature [92] demonstrates a hybrid UWB and Wi-Fi positioning system, and four base stations are used in the experiment. Under the premise that the total number of base stations remains unchanged, the number of UWB base stations is gradually increased, and from the results of the comparison experiments, it can be seen that the system's positioning accuracy increases with the increase of the number of UWB base stations. So, in the LOS environment, UWB can help Wi-Fi or BLE IPS to improve the positioning accuracy, but if UWB is the subject of research, Wi-Fi and BLE will be counterproductive and reduce the accuracy.

2.5.2 Overview of Sensor Fusion Algorithms

Due to different sensors' inherent strengths and weaknesses, relying solely on a single sensor to obtain accurate data is not recommended. Sensor fusion algorithms are commonly employed to overcome this limitation, and they will be introduced in this section.

Kalman Filter (KF)

The Kalman filter is a recursive algorithm that employs a state model to estimate the state of a linear system by manipulating input and measurement data. It effectively suppresses sensor noise for individual sensors and is a widely adopted approach for multi-sensor fusion.

The KF only applies to linear systems, and the following two equations describe the system's process model and observation equation.

$$x_n = Fx_{n-1} + Gu_{n-1} + w_{n-1} \tag{2.9}$$

$$z_k = Hx_n + v_n \tag{2.10}$$

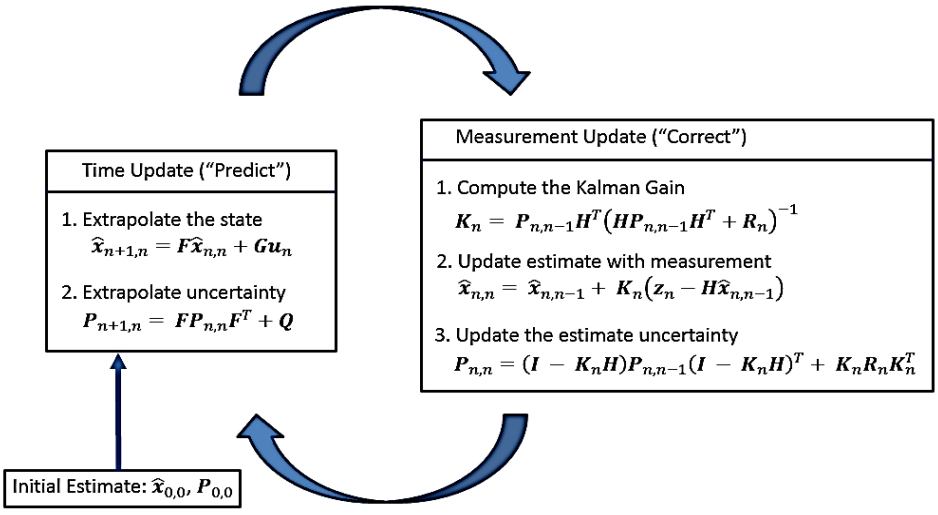

Figure 2.7 Kalman filter (KF) [93]

The KF consists of two components comprising five fundamental equations. The first component is the time update equation, also called prediction, and the

second is the measurement update equation, also known as correction. Figure 2.7 visually depicts this iterative process, wherein upon inputting the system's initial state, the KF estimates the subsequent moment.

Extended Kalman Filter (EKF)

The KF is restricted to linear systems; thus, its application to non-linear systems may yield scattered prediction results. However, object motion states are often described non-linearly in IPSs, necessitating a filter specifically designed for non-linear systems. The EKF addresses this issue by linearising the non-linear system through a first-order Taylor expansion and iteratively updating predicted values using a predicted and correct approach similar to the KF. This process is illustrated in Figure 2.8.

The following two equations can describe the state transition model and observation model for a non-linear system.

$$\boldsymbol{x}_k = f(\boldsymbol{x}_{k-1}, \boldsymbol{u}_k) + \boldsymbol{w}_k \tag{2.11}$$

$$\boldsymbol{z}_k = h(\boldsymbol{x}_k) + \boldsymbol{v}_k \tag{2.12}$$

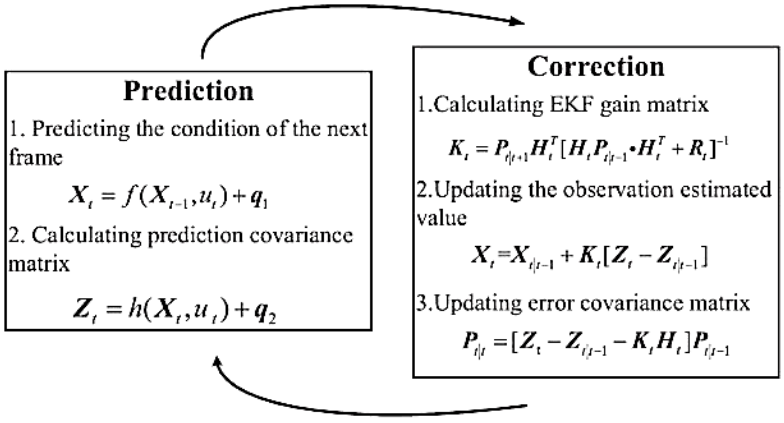

Figure 2.8 EKF [94]

While the EKF serves as a valuable tool for addressing non-linear systems, it is crucial to acknowledge that its utilisation entails linearisation errors arising from

neglecting higher-order terms in the Taylor expansion. In scenarios characterised by high nonlinearity, employing EKF may lead to imprecise state estimation and even divergence [95].

Unscented Kalman Filter (UKF)

The UKF method uses an unscented transformation to represent the probability distribution of a non-linear system's state through a set of sigma points without linearising the system [96]. Compared to the EKF, the UKF is more accurate and robust in handling strongly non-linear systems [97]. The computation of the UKF can be described using the following equation.

Step 1: Set the initial value of UKF:

$$\hat{X}_0 = E(X_0) \tag{2.13}$$

$$P_0 = E[(X - X_0)(X - X_0)^T] \tag{2.14}$$

The $\hat{X}_0$ is the initial state estimation vector, P_0 is the initial covariance matrix.

Step 2: Calculate sigma points:

$$X_k^{(0)} = \hat{x}_k \tag{2.15}$$

$$X_k^{(i)} = \hat{x}_k + (-1)^i \sqrt{(n+\lambda)P_{k_i}}\ for\ i = 1,2,\dots,2n \tag{2.16}$$

The corresponding weights are

$$W_0^{(m)} = \frac{\lambda}{n+\lambda} \tag{2.17}$$

$$W_0^{(c)} = \frac{\lambda}{n+\lambda} + (1 - \alpha^2 + \beta) \tag{2.18}$$

$$W_i^{(m)} = W_i^{(c)} = \frac{1}{2(n+\lambda)}\ for\ i = 1,\dots,2n \tag{2.19}$$

$$\lambda = \alpha^2(n+\kappa) - n \tag{2.20}$$

where n is the dimension of the state vector, and α and κ are used to adjust the distribution of sigma points.

Step 3: Sigma point propagation:

$$X_k^{(i)} = f\left(X_{k-1}^{(i)}, u_k\right) \tag{2.21}$$

Sigma points spread through the state transition function f, u_k is the control input.

Step 4: Predictions:

The predicted values of the state vector ($\hat{x}_k^-$) and covariance matrix (P_k^-) can be calculated using sigma points:

$$\hat{x}_k^- = \sum_{i=0}^{2n} w_m^{(i)} X_k^{(i)} \tag{2.22}$$

$$P_k^- = \sum_{i=0}^{2n} w_c^{(i)} \left[X_k^{(i)} - \hat{x}_k^-\right]\left[X_k^{(i)} - \hat{x}_k^-\right]^T + Q \tag{2.23}$$

where $w_m^{(i)}$ represents the weight of the mean, $w_c^{(i)}$ represents the weight of covariance, and Q is the covariance of process noise.

Step 5: Update:

- Sigma points propagate through observational models

$$Z_k^{(i)} = h\left(X_k^{(i)}\right) \tag{2.24}$$

h is the observational model.

- Calculate the prediction and covariance of the observations.

$$\hat{y}_k = \sum_{i=0}^{2n} w_m^{(i)} Z_k^{(i)} \tag{2.25}$$

$$S_k = \sum_{i=0}^{2n} w_c^{(i)} \left[Z_k^{(i)} - \hat{y}_k\right]\left[Z_k^{(i)} - \hat{y}_k\right]^T + R \tag{2.26}$$

R is the observed noise covariance.

- Kalman gain

$$K_k = P_{xy} S_k^{-1} \tag{2.27}$$

$$P_{xy} = \sum_{i=0}^{2n} w_c^{(i)} \left[X_k^{(i)} - \hat{x}_k^-\right]\left[Z_k^{(i)} - \hat{y}_k\right]^T \tag{2.28}$$

- Update state vector and covariance.

$$\hat{x}_k = \hat{x}_k^- + K_k(y_k - \hat{y}_k) \tag{2.29}$$

$$P_k = P_k^- - K_k S_k K_k^T \tag{2.30}$$

Various studies have demonstrated that the UKF and EKF exhibit comparable performance in systems with weak nonlinearities [97, 98], and Alfonso et al. [99] claimed that in the case of solid nonlinearities, the estimates of the EKF and covariance are accurate to the first order. In contrast, the estimates of the UKF can reach the third order, and the covariance can be estimated to the second order.

Particle Filter (PF)

The PF is a recursive Bayesian filter that offers valuable assistance in the state estimation of non-linear or non-Gaussian systems. It effectively represents the probability density function of a system by employing a discrete set of particles, each encapsulating a hypothesis regarding the current system state and assigning distinct weights to reflect their correctness throughout the recursive process. These weights are updated via resampling, leading to an enhanced and more accurate state estimate. The specific algorithm employed is illustrated in Figure 2.9 below.

1. Initialization:
   Generate sample set $\{\mathbf{x}_0^i\}_{i=1}^N$ from the initial distribution $p(\mathbf{x}_0)$, set $k=1$.
2. Prediction:
   Draw predicted sample $\mathbf{x}_k^i \sim p(\mathbf{x}_k \mid \mathbf{x}_{k-1}^i)$, $i=1,\ldots,N$
3. Update:
   Once the observation data $\mathbf{z}_k$ is measured, evaluate weight of sample $\tilde{w}_k^i = w_{k-1}^i p(\mathbf{z}_k \mid \mathbf{x}_k^i)$, and normalize $w_k^i = \tilde{w}_k^i \Big/ \sum_{q=1}^N \tilde{w}_k^q$, $i=1,\ldots,N$.
4. Resampling:
   Generate new sample set $\{\mathbf{x}_k^j\}_{j=1}^N$ by resampling (with replacement) N times from $\{\mathbf{x}_k^i\}_{i=1}^N$, where $\Pr(\mathbf{x}_k^j = \mathbf{x}_k^i) = w_k^i$, and set weight $w_k^j = 1/N$.
   - Set $k = k+1$ and go back to step 2.

Figure 2.9 Particle filter (PF) [100]

While RF may be less computationally intensive than EKF and UKF [96], it still requires significant computational resources to maintain a large number of particles when dealing with high-dimensional systems. Additionally, the particle set may degrade over time, resulting in the loss of many particles with small weights and a subsequent decrease in estimation accuracy.

2.6 Conclusion

This part focuses on studying IPS with UWB as the main body, including the principle of UWB ranging, positioning algorithms, and the fusion trend with other sensors and algorithms. The following three main conclusions can be made based on reviewing the existing literature and comparing different technologies. Firstly, the accuracy of UWB is better than that of WIFI and BLE in RF-based positioning systems; secondly, IMU is still an indispensable component in many sensor fusion systems; and thirdly, AI is increasingly recognised for its powerful data processing capability in sensor fusion. Table 2.1 below lists the technical details and positioning accuracy of UWB with different sensor fusion systems

Table 2.1 Comparing different fusion solutions with UWB

Reference	Sensors	Fusion Algorithm	LOS Or NLOS	Accuracy (cm)
[65]	IMU, UWB	CKF	Weak NLOS	UWB ranging: 10-20
[101]	IMU, UWB	KF	Hard NLOS	RMSE : 30–40
[66]	IMU, UWB	DWF-MAEFF	Weak NLOS	East: 19.8 North:.15.6

[102]	IMU, UWB	KF	Weak NLOS	Average error: 7.58
[67]	IMU, UWB	ESKF	Weak NLOS	<10
[3]	IMU, UWB	Adaptive KF	Weak NLOS	<10
[103]	IMU, UWB	Cascaded KF	Weak NLOS	< 13
[104]	IMU, UWB	UKF	LOS	UWB only: 5 UWB+IMU:1.5
[63]	IMU, UWB	EKF	Weak NLOS	Mean error< 50
[68]	UWB,Odometer	DWBPF	Weak NLOS	6.1
[105]	UWB, IMU, LiDAR	Error state KF (ESKF)	Weak NLOS	RMSE X: 10 Y: 10 Z:30
[71]	IMU, UWB, Odometer	ESKF	LOS	TOA: 13 AOA: 26
[72]	IMU, UWB, Odometer	EKF	LOS	RMSE:3.29
[106]	UWB, binocular VO	KF	LOS	Mean error X: 39.93 Y: 27.69
[84]	UWB, IMU, monocular	Tightly coupling	LOS	10-20
[85]	Stereo camera, IMU , UWB	Resilient tightly coupling	LOS	Around 10
[90]	Wi-Fi, UWB	ML	Weak NLOS	RMSE: 94
[107]	Wi-Fi, UWB	None	LOS	Mean error: 109

[91]	BLE, UWB	EKF	LOS	Average error:60
[108]	UWB, INS, Map	EKF	Weak NLOS	RMSE: 0.27m

The table shows that the accuracy of UWB in LOS environments is mostly within 10 cm, but even slight NLOS can seriously degrade the positioning accuracy of UWB IPS. Moreover, most literature does not address UWB-only positioning systems in depth. Multi-sensor fusion is an effective method to improve the positioning accuracy of UWB IPS under NLOS conditions. Therefore, in this study, the UWB-only IPS is first thoroughly investigated so that the UWB system itself can provide more accurate positioning accuracy under severe NLOS conditions. Then, the robustness and accuracy of the system can be further improved through the fusion with wheeled odometers. This study aims for a low-cost centimetre-level IPS based on UWB in harsh NLOS environments.

3. Chapter 3 Improved UWB-Only System

The main objective of the research in this chapter is to explore the problems and identify research directions for UWB-Only IPSs. The first part describes the algorithm for UWB NLOS identification via sliding windows and proposes a simple 2D NLOS error modelling algorithm for walls when the anchor point and tag are in the same plane. Based on the previous research, the tag is placed in a different plane from the anchor point to construct a complex 3D NLOS error model in the second part. That is more in line with practical use, and to further improve the positioning accuracy by proposing a weighted least-squares method that adjusts the weights of the measured values according to the angle of incidence of the UWB signals. The final section proposes a mobile anchor deployment scenario to explore ways to reduce hardware costs when deploying UWB IPS.

3.1 NLOS Identification Algorithm by Sliding Window and an NLOS Mitigation Algorithm for A 2D Wall Error Model

3.1.1 Introduction

UWB is a new wireless communication technology that uses a narrow nanosecond pulse to transmit data. It has good anti-interference performance, high data transmission rate, low energy consumption, high positioning accuracy and multipath robustness [109]. Therefore, UWB is considered the most promising indoor positioning technology. Some major smartphone manufacturers, such as Apple and Samsung, have launched models supporting UWB positioning. It can be predicted that indoor positioning using UWB technology will be widely used

in wearable equipment, intelligent homes, extended reality and mobile robots [110]. At the same time, UWB's positioning also has a wide range of industrial applications, such as intelligent manufacturing and warehouse. A UWB IPS consists of fixed anchor points and mobile tags that need to be located.

UWB positioning often uses TOA [111] or TDOA [112] algorithms, which have higher positioning accuracy than fingerprint positioning based on the received signal strength indicator (RSSI). However, those algorithms estimate a UWB tag's position by measuring the distance between the anchor points and the tag. The distance is measured by counting the time of UWB signal transmission. In the case of NLOS, the UWB signal can only reach a tag by penetrating obstacles or reflection, so compared to LOS, there is a transmission delay [113]. In indoor environments, obstacles such as walls and the human body often appear, leading to NLOS. If the distance error caused by NLOS is not corrected, the positioning accuracy of UWB in an indoor environment will be heavily degraded [51]. Therefore, identifying NLOS and reducing the ranging error caused by it is a major focus in UWB positioning research.

Many researchers have proposed methods to identify NLOS and correct its errors. NLOS identification methods can be classified into three categories [51]. The first category is based on statistical channel characteristics. Jiang et al. [51] proposed an NLOS recognition algorithm that combines CNN and LSTM, which extracts channel impulse response features of UWB signals through CNN recognition and outputs them to LSTM for classification. The recognition accuracy of NLOS error can reach 81.56%. Cui et al. [114] proposed a method to identify NLOS based on Morlet wavelet transform and CNN. Its identification accuracy can reach 95% in different environments. Kai et al. [115] proposed a method that uses signal characteristic analysis for NLOS identification and fuzzy theory for error mitigation. It can reduce the measurements' RMSE from 0.77 to 0.33 meters.

The second category is based on the analysis of ranging measurements. The basic principle of this method is to analyse the ranging information in both LOS and NLOS and correct the meandering in the NLOS environment to improve positioning accuracy. For example, Dong [116] uses the Fresnel zone and simple prior knowledge to identify NLOS and has a recognition accuracy of 96.41%. However, there is still a critical problem with this method. When verifying whether the tag is in the NLOS environment through this method, the tag position must be in the first Fresnel zone of the two fixed anchors. This leads to a severe limitation of the range of the tag movement. Therefore, this method cannot be applied to most indoor positioning scenarios.

The third category is to identify NLOS by combining other measurement data. For example, Tiwari et al. [117] and Zuo et al. [118] proposed successfully identifying LOS/NLOS paths by combining RSS and TOA with an accuracy of NLOS determination of over 75%.

A new method to identify NLOS in UWB indoor positioning, based on analysing the variance of distance variation at two adjacent moments, is proposed here. The UWB ranging variations from a tag to the same anchor at two adjacent moments should be similar when the tag moves smoothly. However, due to NLOS delay, the distance measurement has a sharp jump from LOS to NLOS and a sharp drop from NLOS to LOS. The variance of the distance difference can be used to detect whether a ranging measurement contains NLOS error.

After identifying which measurements have NLOS errors, there are a few ways to process these measurements. If an NLOS delay estimation model is available to correct the error, the corrected measurements can be used for UWB indoor positioning. If there is no proper delay estimation model to correct the NLOS

errors, the NLOS measurements' weight is lighter than the LOS measurements during the position calculation. The results of UWB indoor positioning tests show that the proposed method can effectively identify and mitigate NLOS errors and dramatically improve UWB positioning accuracy in instances involving NLOS.

The rest of this section is structured as follows. The second section introduces the proposed method to identify NLOS. The third section discusses the NLOS delay correcting model for walls. The fourth section shows the indoor positioning results with corrected NLOS measurements. The last section offers a conclusion and briefly considers potential future research.

3.1.2 Proposed Method for NLOS Identification

The Method to Identify NLOS

The principle of the proposed method to identify NLOS is based on the fact that when there is a switch between NLOS and LOS cases for a tag and an anchor point, the ranging measurement of this anchor point will change abruptly.

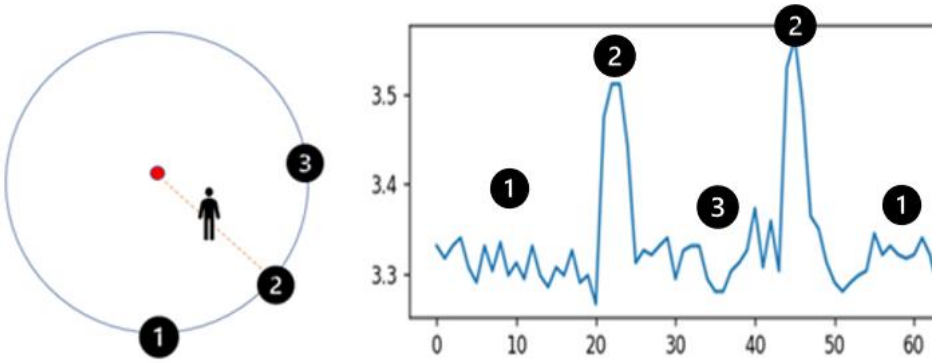

Figure 3.1 NLOS error caused by the human body

A preliminary verification test is shown in Figure 3.1. The left figure shows the experimental scene setting. The red dot in the figure is the position of the fixed anchor point, and the black dots are the mobile tag's positions. In the test, a tag

moves in a circle at a constant speed from position 1 to 3 and then back to position 1 from 3. A human body blocks the signal when the tag passes through position 2, and NLOS occurs. The distance measurements are shown in the right figure. The X-axis represents time, and the Y-axis represents the distance measurements between the tag and the anchor. The distance measurement suddenly changed when the tag was in position 2, which is NLOS. The NLOS error caused by the human body is about 20cm.

The proposed NLOS identification method is designed as Algorithm 1.

Algorithm 1 NLOS Identification

Input: Distance sequence $\{d_n\}$, $n = 1, 2, 3, \ldots$
Output: Classification of LOS or NLOS
Step 1: Compute Distance Differences
for $n \leftarrow 2$ to N **do**
  $\Delta d_n \leftarrow |d_n - d_{n-1}|$
end for
Step 2: Calculate Threshold
$threshold \leftarrow Var(\Delta d_n(LOS))$
Step 3: Classify LOS or NLOS
if $Var(\Delta d_n) > threshold$ **then**
  Classification $\leftarrow NLOS$
else
  Classification $\leftarrow LOS$
end if
return Classification

The distance between the tag and anchor measured at the moment n is d_n, and at the previous moment is d_{n-1}. Then, the distance change in the adjacent sampling times is shown in Equation 3.1.

$$\Delta d_n = |d_n - d_{n-1}| \cdots (\mathrm{n} \cdot =\cdot 2{,}3 \ldots) \tag{3.1}$$

$$threshold = Var\big(\Delta d_n(LOS)\big) \tag{3.2}$$

$$\mathrm{Var}(\Delta d_n)\begin{cases} \cdots > \text{ threshold } \cdots \rightarrow \text{ NLOS} \\ \leq \text{ threshold } \rightarrow \text{ LOS} \end{cases} \tag{3.3}$$

AGVs operating in an indoor environment have a consistent moving speed of around 1m/s during operation. When an AGV moves in the LOS environment, a

UWB tag continuously measures the distance to anchor points, the distance variation. Δd_n is small and relatively stable. But when NLOS occurs, Δd_n will shake violently. Based on these characteristics, a method to identify NLOS errors is designed, as shown in Equations 3.1 to 3.3. Using the variance of Δd_n in the LOS as the threshold when the variance of Δd_n in real-time measurement exceeds this threshold, NLOS occurs. This method is simple but can accurately identify whether a ranging data contains NLOS error.

Experimental design

Figure 3.2 shows the UWB module used in our experiment, which uses the DW1000 UWB chip. The UWB sampling rate is 3Hz, and its average positioning error is less than 10cm in an LOS environment. The experimental scene and the floor plan are shown in Figure 3.3. Two experiments were conducted. The first experiment used three fixed anchor points, and the second experiment used four fixed anchor points.

According to the algorithm proposed in the previous section, a segment of Tag's LOS data in the experimental environment will be collected first to calculate the threshold value. In further experiments, Tag will move according to a certain path, and from the map, it can be seen that multiple walls in the experimental environment will block the communication between Tag and different anchors. In this process, the NLOS/LOS status of different anchors is unknown, and according to the algorithm in the previous section, the variance of the difference between the ranging values of all the anchors is continuously monitored, and when there is an outlier larger than the threshold, it can be assumed that this outlier contains the NLOS error.

Figure 3.2 UWB module

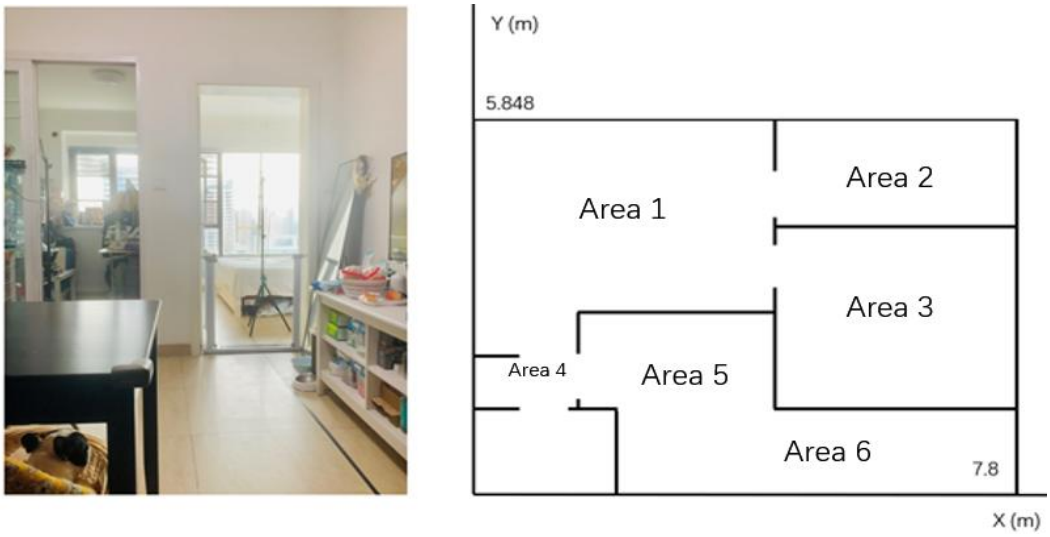

Figure 3.3 The experiment site and ichnography

Experiment 1

Figure 3.4 shows the anchor's setting, the tag's real trajectory and measured position, and the NLOS appearance of each anchor. Yellow squares represent the three anchor points. The UWB tag moves from Area 3 along the red track and passes through Areas 1 and 4 to the endpoint in Area 5. The purple trajectory is calculated using the TOA algorithm and the distance measurements to the three anchor points. It is observed that within Area 3, all Anchor 2 ranging measurements and most Anchor 0 ranging measurements contain NLOS errors. In Area 1, all anchors are in a LOS environment. After entering Area 4, Anchors 0 and 1 are still in the LOS environment, but Anchor 2 has NLOS errors. When in Area 5, all three anchor points are NLOS. From the purple trajectory, it can be

found that the NLOS error dramatically influences the accuracy of the UWB positioning.

The NLOS identification method proposed in this chapter can accurately identify which data of the three anchor points have NLOS errors. Figure 3.4 a) – c) shows the positioning corresponding to the three anchor points affected by NLOS. The blue dot indicates that the ranging measurement of the current position is affected by NLOS.

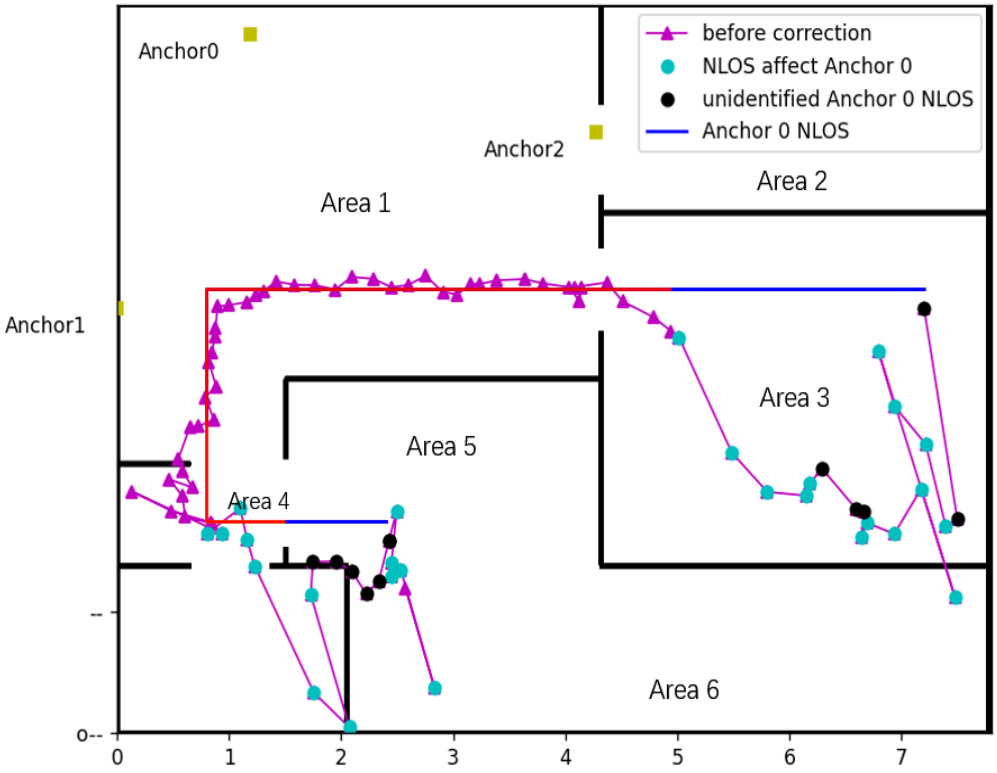

a) Anchor o NLOS

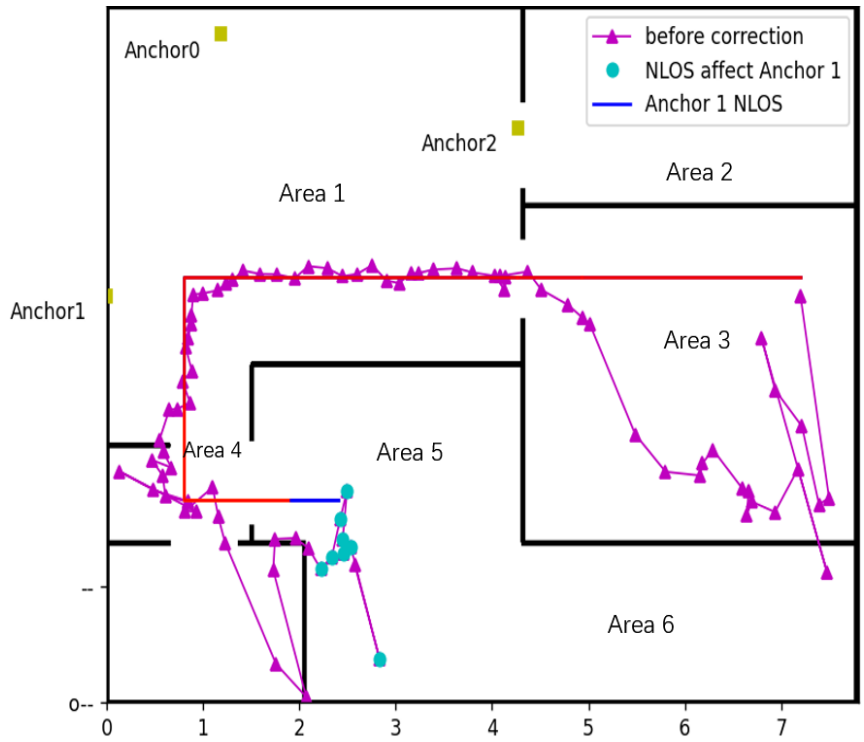

b) Anchor 1 NLOS

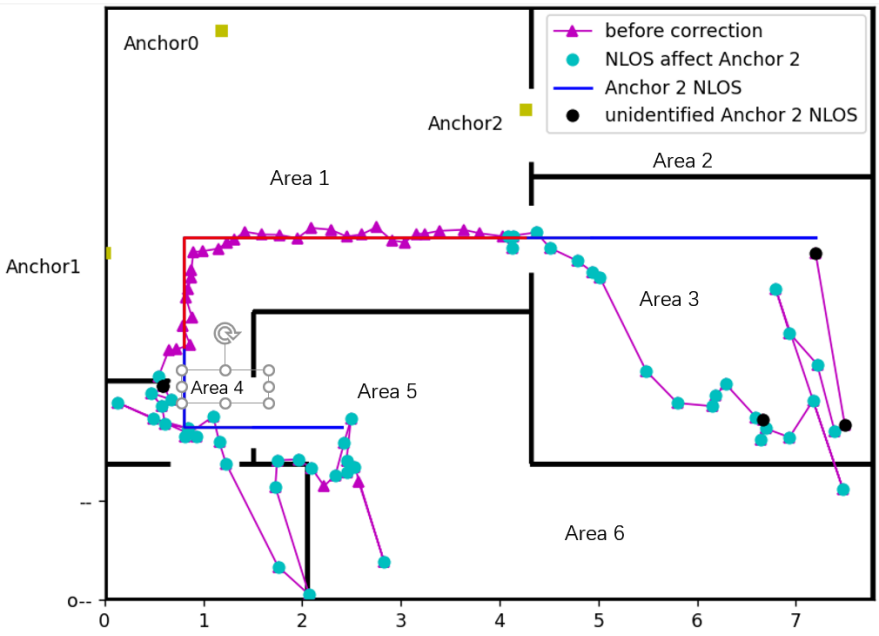

c) Anchor 2 NLOS

Figure 3.4 Tag position with NLOS (Experiment 1)

In the experimental environment, the NLOS identification rate is shown in Table 3.1. In this experimental environment, the identification of NLOS error is

accurate. The accuracy of Anchor 1 and Anchor 2 is greater than 95%, and the accuracy of Anchor 0 is close to 90%

Table 3.1 The success rate of NLOS identifications (Test 1)

Anchor	0	1	2
Identification rate	89.41%	100%	95.29%

Experiment 2

Experiment 2 uses four fixed anchor points, making the tag's trajectory more complex. It is designed to verify further the applicability of the method proposed in this part.

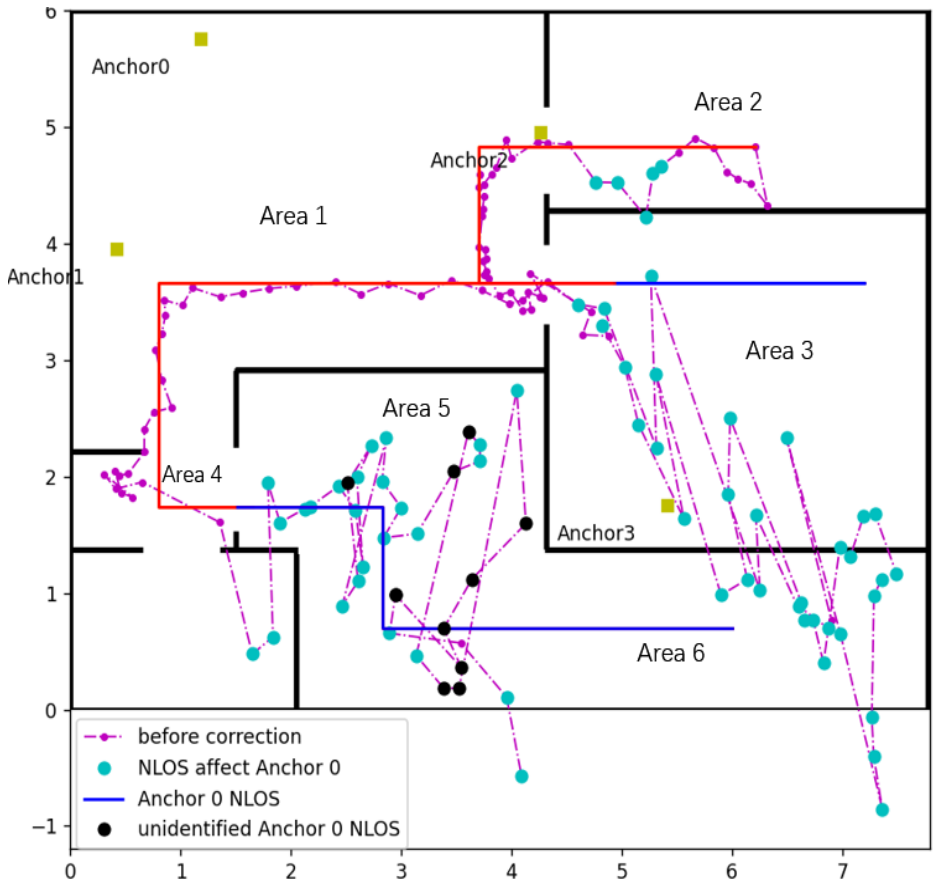

a) Anchor 0 NLOS

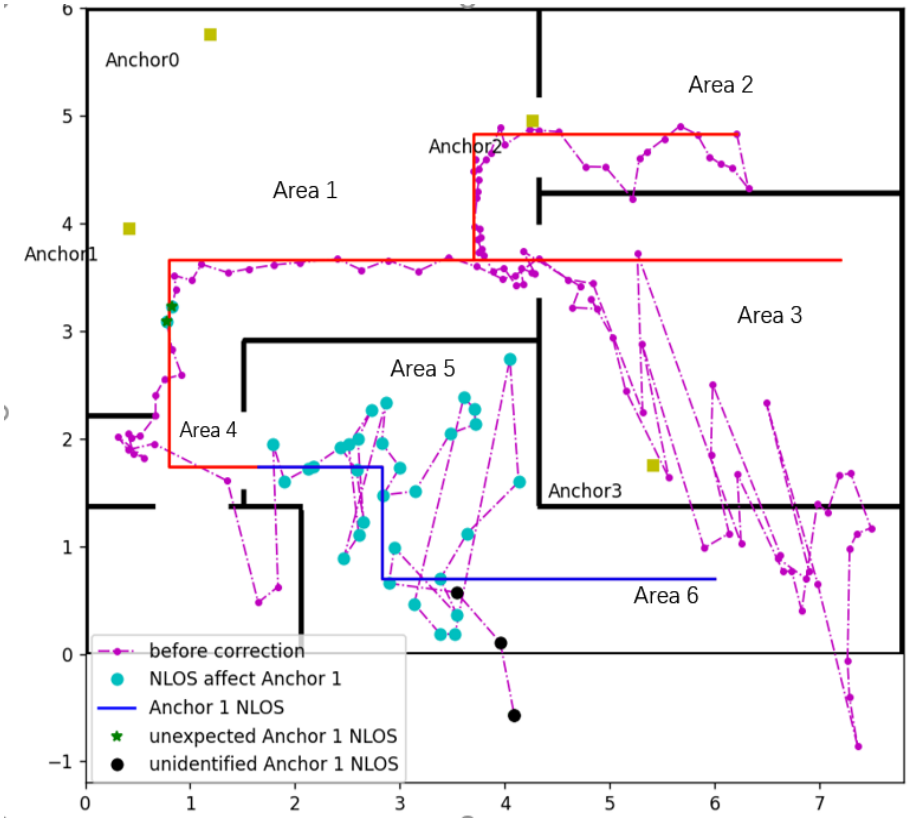

b) Anchor 1 NLOS

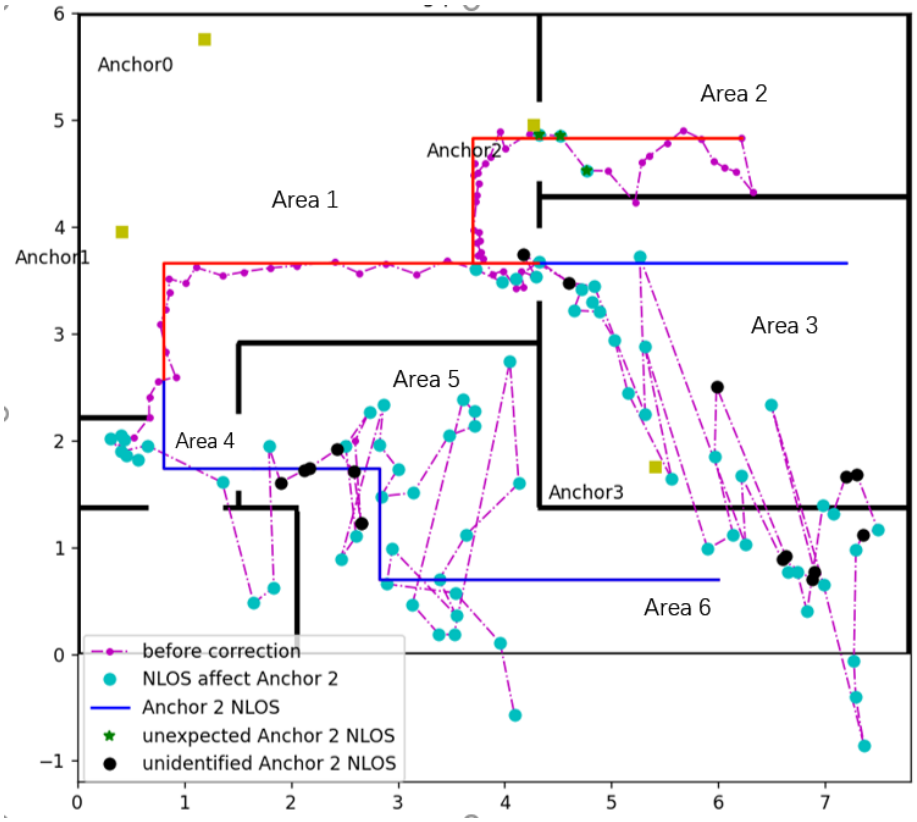

c) Anchor 2 NLOS

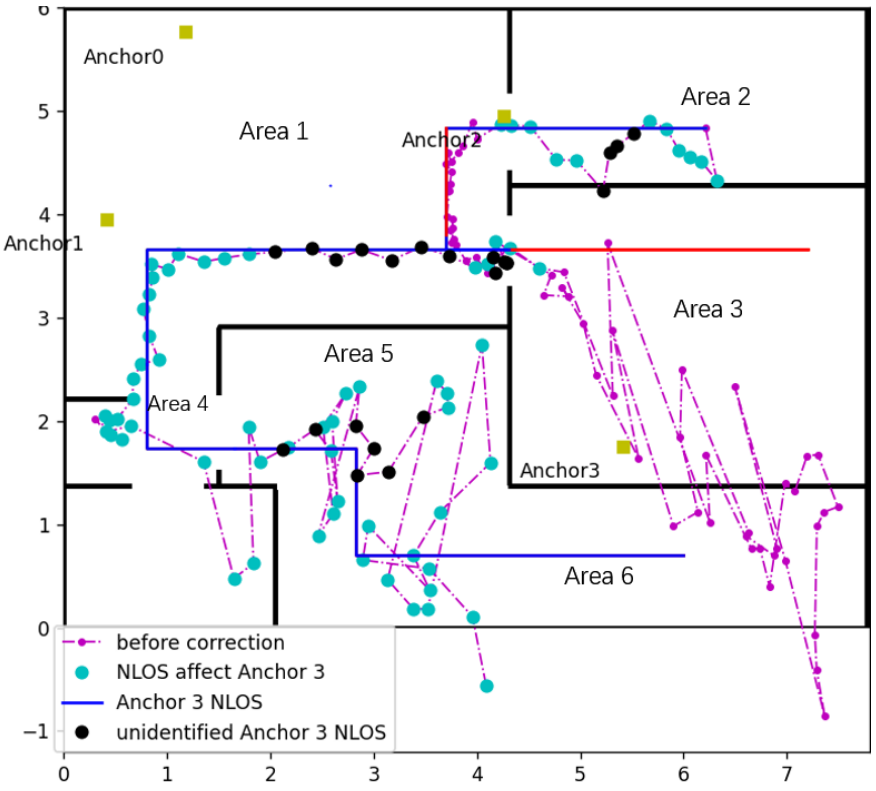

d) Anchor 3 NLOS

Figure 3.5 Tag position with NLOS (Experiment 2)

As shown in Figure 3.5, Anchor 3 is added in this experiment. The red dash line shows the actual trajectory of the mobile UWB tag. The tag starts from Area 2, passes through Area 1 to the marked point of Area 3, then starts from the marked point of Area 3 and follows the red trajectory through Areas 1, 4 and 5 to reach the endpoint in Area 6. The purple trajectory is calculated based on the ranging measurement of the anchor point without NLOS correction.

There are at least three anchor points in the LOS situation in Area 1, and the UWB positioning accuracy is very high. In other areas, at least two anchor points have NLOS, and the positioning accuracy without NLOS error correction is much worse than LOS in Area 1. In Area 6, all four anchor points are in an NLOS state, and only the signal from Anchor 3 penetrating one wall has a ranging measurement. Multiple walls block the UWB signals from the other three anchor

points, and the tag-received signals are too weak to measure the distances. Therefore, the tag's position cannot be obtained in Area 6.

Like Experiment 1, the test data is processed to identify if the distance measurements contain NLOS errors. Figure 3.5 a) to d) shows the calculated locations where the ranging measurement of the four anchor points are affected by NLOS. A few positions have unexpected or undetected NLOS, possibly due to undesired settings in the experiment. In the current Experiment 2 environment, the NLOS identification success rate is shown in Table 3.2.

Table 3.2 The success rate of NLOS identifications (Test 2)

Anchor	**0**	**1**	**2**	**3**
Identification rate	91.22%	95.27%	89.19%	85.46%

As can be seen from Table 3.2, the UWB tag's trajectory becomes more complex and covers more areas. The success rate of NLOS identification in Experiment 2 is slightly lower than in Experiment 1. Nevertheless, most NLOS cases can be correctly identified, with the overall success rate around 90%. Unexpected factors in the experiment caused some incorrect identification cases.

3.1.3 NLOS Error Correction Model

Geometric Model of UWB Signal Through a Wall

In UWB indoor positioning, NLOS is mainly caused by the occlusion of walls. A geometric model can estimate the UWB signal transmission delay caused by passing through walls, dramatically reducing positioning errors in the NLOS environment. The specific model is shown in Figure 3.6. A is a fixed anchor point, B is the tag position, and the grey area represents the wall causing NLOS. ACDB is the actual path of the signal from A to B.

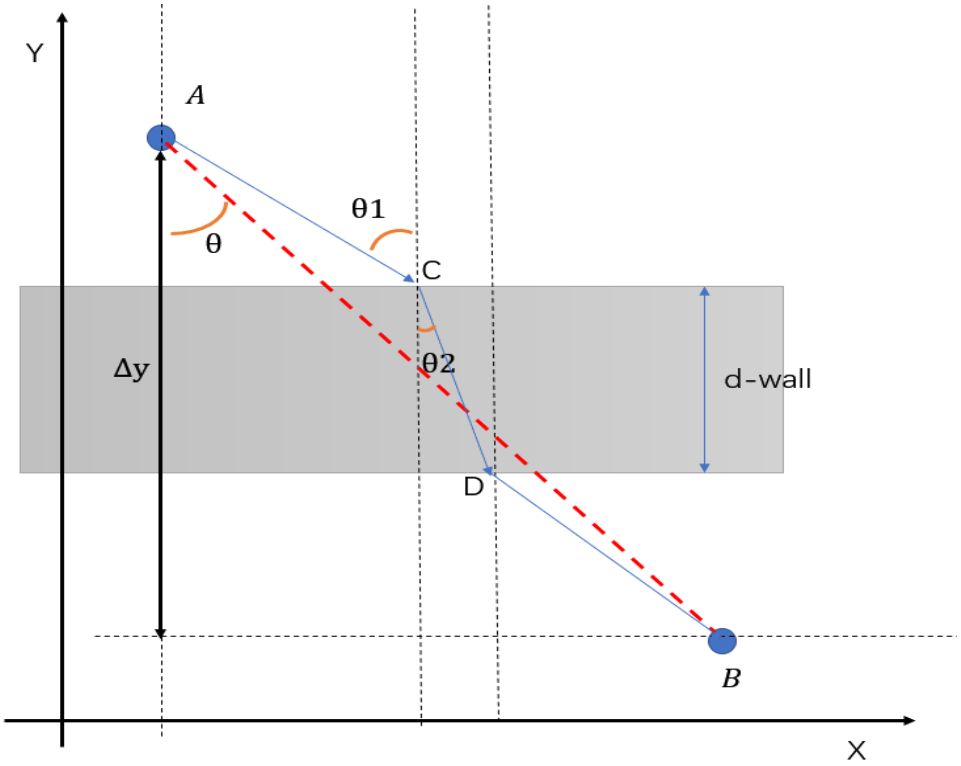

Figure 3.6 Geometric model of UWB signal passing through a wall.

$$d_{real} = d_{AC} + d_{CD} + d_{DB} \tag{3.4}$$

where d_{real} represents the actual distance the signal travels,

$$d_{AC} + d_{DB} = \frac{\Delta y - d_{wall}}{cos\theta_1} \tag{3.5}$$

$$\Delta y = d_{AB} * cos\theta \tag{3.6}$$

where d_{wall} represent the wall thickness, θ_1 is the incline angle of the signal to the wall, θ_2 is the angle of emergence, Δy is the distance difference along the Y-axis between points A and B, θ is the complementary angle between the line AB and the wall, and d_{AB} is the actual distance between A and B.

$$d_{CD} = \frac{d_{wall}}{cos\theta_2} \tag{3.7}$$

Because of the permittivity of the wall ε_{wall} is different from the air, the signal travels in the wall slower than in the air, resulting in additional time delay. The measured CD distance in practice should be the time of flight through the wall t_{wall} multiplied by the speed of light c, as calculated in the following formula.

$$d_{CD} = t_{wall} * c = \frac{d_{wall} * \sqrt{\varepsilon_{wall}}}{cos\theta_2} \tag{3.8}$$

So, the ranging delay is:

$$delay = d_{real} - d_{AB} \tag{3.9}$$

$$delay = d_{AB}\left(\frac{cos\theta}{cos\theta_1} - 1\right) + d_{wall}\left(\frac{\sqrt{\varepsilon_{wall}}}{cos\theta_2} - \frac{1}{cos\theta_1}\right) \tag{3.10}$$

where $sin\theta_2/sin\theta_1 = \sqrt{\varepsilon_{wall}}$ as the Snell's Law.

Equation 3.10 has two key elements: $e_1 = d_{AB}(cos\theta/cos\theta_1 - 1)$ and $e_2 = d_{wall}\left(\frac{\sqrt{\varepsilon_{wall}}}{cos\theta_2} - 1/cos\theta_1\right)$. In general, $d_{wall} \ll d_{AB}$ and $\theta_1 \approx \theta$, so e_1 is too small to affect NLOS delay. Therefore e_2 is the main factor affecting the NLOS delay. Then, the ranging delay can be approximately expressed by the following equation, Equation 3.11.

$$Delay \approx d_{wall}\left(\frac{{\varepsilon_{wall}}^{\frac{3}{2}}}{\sqrt{\varepsilon_{wall} - 1 + cos^2\theta_1}} - \frac{1}{cos\theta_1}\right) \tag{3.11}$$

According to Equation 3.11, the transmission delay is affected by the thickness and material of the wall and the incline angle. Therefore, an empirical model can be established for the wall-caused transmission delay.

$$Delay = K1 * \frac{d_{wall}}{cos\theta_1} + K2 \tag{3.12}$$

K1 and K2 can be determined by conducting a test for a wall, as shown in Tables 3.3 and 3.4, by measuring the actual and UWB measured distances at different incline angles.

The wall thickness between Areas 2 and 3 is 26 cm, and between Areas 5 and 1 is 16 cm. The fitting equation for K1 and K2 was calculated based on UWB-measured distances through a wall with NLOS delay, the real distance and the incline angle measurements are shown in Tables 3.3 and 3.4. The coefficients K1 and K2 for each wall are then fit into (15) to calculate the NLOS delay of each wall at different angles.

Table 3.3 Data for fitting equation (D_wall = 26cm)

d-uwb (m)	d-real (m)	Delay (m)	θ (°)	Modelling Delay(m)	Difference (m)
1.965	1.788	0.177	0°	0.352	0.175
1.545	1.322	0.223	8.52°	0.355	0.132
2.21	1.716	0.494	30°	0.384	0.110
3.378	3.042	0.336	54°	0.497	0.161
3.65	2.972	0.678	60°	0.559	0.119
7.18	5.983	1.197	70.16°	0.754	0.443

Table 3.4 Data for fitting equation (D_wall = 16cm)

d-uwb (m)	d-real (m)	Delay (m)	θ (°)	Modelling Delay(m)	Difference (m)
3.87	3.587	0.283	13.37°	0.213	0.060
4.01	3.823	0.187	31.1°	0.225	0.038
3.67	3.526	0.144	42.2°	0.240	0.096
4.34	3.99	0.35	57.01°	0.280	0.069
5.07	4.748	0.322	61.57°	0.303	0.019
5.07	4.419	0.651	80.597°	0.577	0.074

The K1 and K2 obtained from Tables 3.3 and 3.4 for the 26cm wall are K1= 0.7943 and K2 = 0.1459; for the 16cm wall, K1= 0.5934 and K2 = 0.128. These parameters can be applied in Equation 3.12 to calculate NLOS delay. The difference between the modelling delay and the actual delay is shown in the last column of Tables 3.3 and 3.4. It can be seen that only one data set has a large difference (0.443m), which may be due to unexpected factors; the rest of the difference is about 10cm. The results show that model Equation 3.12 can effectively predict the transmission delay of walls.

For a mobile UWB tag, the incline angle at a particular moment is calculated according to the tag position at the last moment and the motion state using Equation 3.13.

$$\theta_{1n} = tan^{-1}\left(\frac{abs(y_{n-1} + v_y * \Delta t - X_N)}{abs(x_{n-1} + v_x * \Delta t - Y_N)}\right) \tag{3.13}$$

where (x_{n-1}, y_{n-1}) are the coordinates of the tag at time n-1, (X_N, Y_N) are the coordinates of the anchor N, Δt is the sampling time, and v_x, v_y are the tag's velocity components along the X and Y axes during the sampling time.

If the ranging measurement of an anchor has NLOS delay, it can be corrected according to Equation 3.14.

$$d_{real} = d_{measure} - delay \tag{3.14}$$

This error modelling algorithm simplifies the NLOS error caused by a wall to be calculated by four quantities: K1, K2, wall thickness, and the angle of incidence of the signal. Although the algorithm needs to calculate two coefficients (K1, K2) for different obstructions, it is not very computationally intensive for relatively fixed indoor environments. Moreover, this algorithm proposes a general error model that can be generalized to the NLOS errors caused by different types of obstructions. The following sections' experiments verify whether this model can accurately calculate the NLOS error and improve the localisation accuracy under different wall thicknesses and incidence angles in a continuously changing movement process. Algorithm 2 demonstrates the proposed NLOS error correction model.

Algorithm 2 NLOS Delay Model (2D)

Input:

d_{AB} (Measured distance)
d_{wall} (Wall thickness)
ε_{wall} (Relative permittivity of the wall)
θ_1, θ_2 (Incident and refracted angles)
K_1, K_2 (Empirical coefficients for delay model)
v_x, v_y (Velocity components), Δt (Time interval)

Output:

d_{real} (Corrected real distance)
$delay$ (Total transmission delay)

Step 1: Calculate Δy

$\Delta y \leftarrow d_{AB} \cdot \cos(\theta)$

Step 2: Calculate d_{AC} and d_{DB}

$d_{AC} + d_{DB} \leftarrow (\Delta y - d_{wall}) / \cos(\theta_1)$

Step 3: Calculate d_{CD}

$d_{CD} \leftarrow d_{wall} / \cos(\theta_2)$

Step 4: Calculate Total Real Distance

$d_{real} \leftarrow d_{AC} + d_{CD} + d_{DB}$

Step 5: Calculate Delay Based on Transmission Model

$delay \leftarrow d_{AB} \cdot \left(\frac{\cos(\theta)}{\cos(\theta_1)} - 1\right) + d_{wall} \cdot \left(\frac{\sqrt{\varepsilon_{wall}}}{\cos(\theta_2)} - \frac{1}{\cos(\theta_1)}\right)$

Step 6: Simplify Delay Using Empirical Model

$delay \leftarrow K_1 \cdot \left(\frac{d_{wall}}{\cos(\theta_1)}\right) + K_2$

Step 7: Correct the Measured Distance

$d_{real} \leftarrow d_{measure} - delay$

return $d_{real}, delay$

3.1.4 Position Experiment Result

Experiment 1

Figure 3.7 shows the positioning results in experiment 1. The green trajectory in the figure is calculated using the NLOS correction data. The golden dots in the trajectory before correction and the golden lines in the real trajectory represent one NLOS at these positions, orange for two, and red for three NLOS. The positioning results before and after the correction are shown in Table 3.5. The data in Area 1 has three anchor points in the LOS environment as the control group.

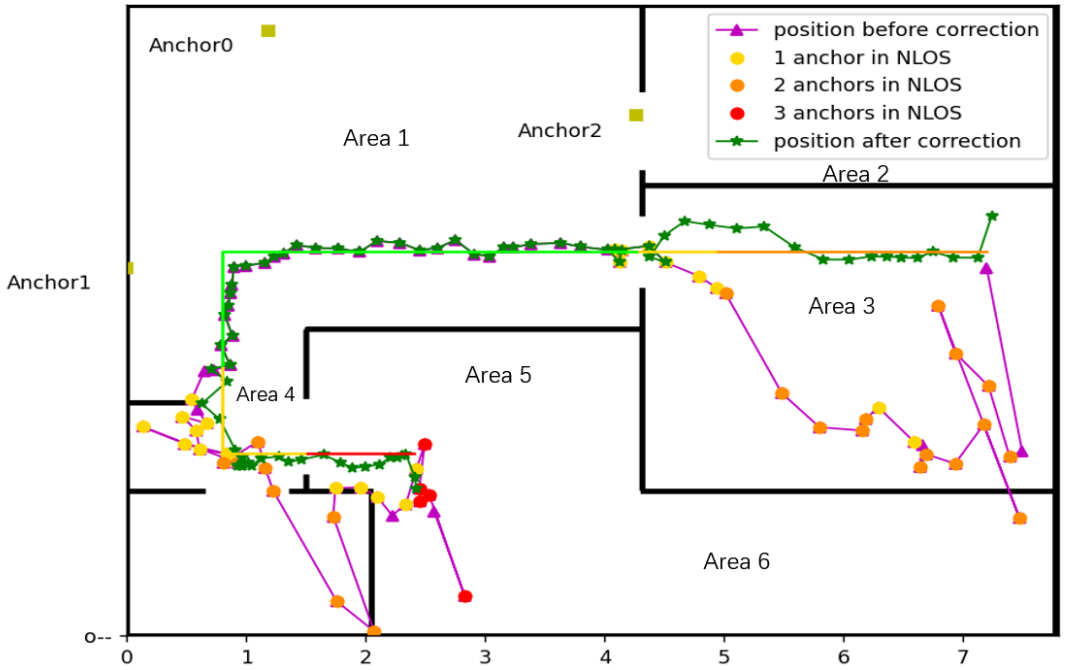

Figure 3.7 Tag position with correction (Experiment 1)

Table 3.5 Positioning analysis (Experiment 1)

Positioning Error (m)	**Area 1**	**Area 3 (2 NLOS)**		**Area 5 (3 NLOS)**	
	LOS	**Before**	**After**	**Before**	**After**
Max (m)	0.235	2.541	0.338	1.694	0.300
Min (m)	0.007	0.518	0.004	0.144	0.009
Average (m)	0.060	1.701	0.122	0.653	0.118
RMSE (m)	0.080	1.759	0.157	0.824	0.156

Test results in Table 3.5 show that the accuracy of the UWB IPS in the LOS environment is relatively high. The average error is only 0.06m, with a RMSE of 0.08m. As a comparison, in the NLOS environment in Area 3 with 2 NLOS anchors, the average error before the correction reaches 1.7m, with an RMSE of 1.759m. After the correction, the average error is reduced to 0.122m and RMSE to 0.157m. A similar result is presented for Area 5 with 3 NLOS anchors, with dramatic positioning improvement after the proposed NLOS error correction. These results show that NLOS error can cause a large error for the UWB indoor

positioning. The proposed NLOS error correction method can significantly reduce the error in the NLOS environment. Its positioning accuracy is close to that in the LOS environment.

Experiment 2

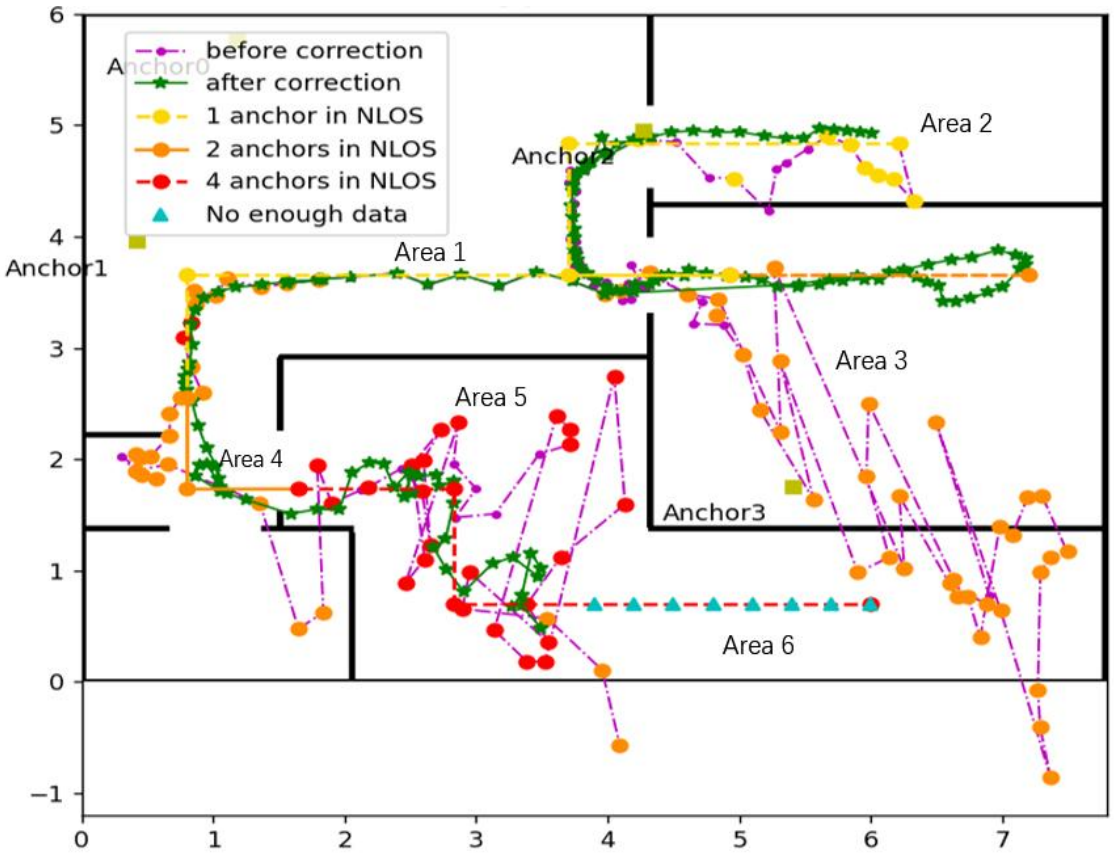

Figure 3.8 Tag position with correction (Experiment 2)

Figure 3.8 shows UWB positioning results for Experiment 2. The green trajectory is the calculated position using the measurements after the correction. The trajectory is much more accurate than the one before the correction, specifically in the NLOS areas. The yellow line for the actual tag trajectory means that one anchor point is affected by NLOS, the orange line for two NLOS anchor points, and the red line means all anchor points are in the NLOS environment. The cyan triangle in Area 6 indicates insufficient ranging information available for the position calculation. Table 3.6 shows the positioning results of experiment 2.

Table 3.6 Positioning analysis (Experiment 2)

Positioning Error	Area 1 (3 LOS)	Area 2 (2 NLOS)		Area 3 (2 NLOS)		Area 5 (4 NLOS)	
		Before	After	Before	After	Before	After
Max (m)	**0.177**	0.606	**0.133**	4.513	**0.247**	1.302	**0.454**
Min (m)	**0.002**	0.009	**0.102**	0.016	**0.003**	0.002	**0.003**
Average (m)	**0.063**	0.232	**0.082**	1.780	**0.080**	0.443	**0.142**
RMSE (m)	**0.081**	0.299	**0.090**	2.173	**0.111**	0.578	**0.181**

The UWB IPS can provide accurate and stable location information of the moving tag in the LOS environment, with an average error of 0.063m. However, the positioning accuracy in the NLOS environment is inferior before correction. The most significant average positioning error is in Area 3 at 1.78m due to a large incline angle of the wall, causing a large NLOS delay. In Areas 2 and 5, the NLOS delay is relatively small due to small incline angles. The positioning accuracy after the delay correction has been dramatically improved. The average positioning errors in the three NLOS areas are 0.082m, 0.08m, and 0.14m, respectively. Moreover, the corresponding RMSEs are 0.09m, 0.111m, and 0.181m, respectively.

It can be concluded that the accuracy of UWB positioning after NLOS error correction is close to the accuracy of positioning in the LOS environment. The proposed method can accurately identify NLOS errors and mitigate them by applying a correction model for wall-caused NLOS delays.

A problem is shown in Figure 3.8. When the tag moves to Area 6, the UWB system can no longer obtain the location information of the tag, so the tag trajectory in Area 6 is missing, as indicated by the blue triangle trace in Figure 3.8. This

problem occurs when the tag is in Area 6, apart from the UWB signal of Anchor 3, which reaches the tag through one wall. The signals of the other anchors, Anchor 0, 1, and 2, must pass through at least two walls to reach the tag. After the actual measurement, anchors 0, 1, and 2 could not obtain the ranging information of the tag, so only the ranging information of Anchor 3 could be used to calculate the position information of the tag through the TOA algorithm.

3.1.5 Conclusion and Future Work

The NLOS identification uses the variance of the difference between the tags ranging from the adjacent sampling times. The transmission delay correction for walls in the NLOS environment uses the geometric signal propagation model. The performance of the proposed method for NLOS identification and correction is evaluated using two experiments. Results of the experiments show that the method can effectively identify NLOS and dramatically improve UWB positioning accuracy in an NLOS environment. The accuracy of NLOS identification can reach more than 90%. For NLOS caused by walls, the proposed correction model can correct the UWB signal transmission delay. Test results show that the UWB positioning accuracy with the correction in the NLOS environment is close to the accuracy in the LOS environment. The proposed method can effectively improve UWB positioning accuracy in an NLOS environment.

Our experiments found a few potential ways to improve UWB positioning accuracy in a complex indoor environment with NLOS. Other objects than walls cause some NLOS, and their transmission delay correction model can be investigated. Their precision is lower for UWB measurements with NLOS errors than LOS. The position calculation with both LOS and NLOS measurements should count the precision difference between LOS and NLOS measurements. However, the UWB tag cannot get enough ranging measurements for its position in some locations. UWB needs to be combined with other positioning

technologies, such as odometer or IMU, to make indoor positioning more robust and reliable

3.2 3D NLOS error model and Weighted Least-Squares method

3.2.1 Introduction

Due to its properties, UWB is a feasible localisation and target-tracking technology. For instance, the UWB uses an extensive baseband to communicate between tags and anchors. The baseband pulse duration is nanoseconds, so the UWB has a high time resolution to tackle the problem of multipath and through-wall propagation [118]. UWB has the same virtues of low power consumption and hardware costs as Bluetooth and Wi-Fi but with greater accuracy.

TOA [119, 120], TDOA [121], AOA [120], and TWR [122] are the commonly used algorithms for UWB IPSs. The range measurements are derived from the signal's TOF between fixed anchors and mobile tags. So, any factors that affect the TOF measurement will impact the accuracy of the measured distance and the position, such as multipath, NLOS, rugged to synchronise between tags and anchors, and interference by other radio waves [123]. The range error caused by NLOS appears when the direct path of the signal between tags and anchors is blocked, and the measured TOF includes the extra time delay. The range error of NLOS is always an enlargement and can reach a few meters, which is the most significant factor harming the accuracy of UWB IPS. In addition, NLOS is unavoidable in real scenarios, so the reduction of NLOS error is of great importance.

Improving the performance of UWB IPS in the NLOS environment can be done in two steps: identification and mitigation. Many approaches have been proposed

to identify the NLOS and mitigate its error, which can be grouped into three categories which include analysing channel characteristics[124], using external constraints and a range error model to identify and mitigate NLOS errors and enhancing accuracy with auxiliary sensors like IMU [125], V-SLAM [126], and Lidar SLAM [64].

All the methodologies above have some inherent problems. For the first category, simulation results in [52] show the accuracy of identifying NLOS by different ML methods: 86.94% for CNN, 78.51% for stacked long short-term memory (stacked-LSTM), and 84% for combined CNN and LSTM. Some machine learning methods claim they can reach 90% accuracy, which positively correlates with the amount of the database. To get the above result in [52], analysing 126,000 channel impulse responses cost CNN 21.84s, stacked-LSTM over 200s and CNN+ LSTM over 15s. Due to the large amount of data and the high time cost, those methods are hard to apply to real-time locations and require fast reaction time. The second category has a better response time but still has some limitations. The experiment results in [116] show that over 90% of NLOS cases can be recognised by the Fresnel zone and threshold from prior knowledge. Still, the Fresnel zone has strict restrictions on the application that cannot be widely used in real scenarios. A consensus is that multisensor fusion can improve IPSs' accuracy, availability, and reliability [127], which will be the future research plan for this project.

The following sections propose a novel, succinct method to identify and mitigate the NLOS error in real-time. The identification step is based on the principle that the measured distance changes rapidly when a switch between NLOS and LOS happens for a moving tag. The variance of the difference of ranges observed from the same anchor between two adjacent time slots is relatively constant in LOS, and it will bump up when a range contains an NLOS error. By this method, NLOS can be distinguished. For NLOS error mitigation, a delay model to correct the

NLOS range error caused by a wall is proposed, which includes the factors of incident angle, wall thickness, and material used to calculate the delay. The delay model is derived from a significant amount of experimental data. The corrected range data by this model is then used to compute the coordinates of the mobile tag using OLS and WLS. Figure 3.9 shows a flowchart of the proposed method.

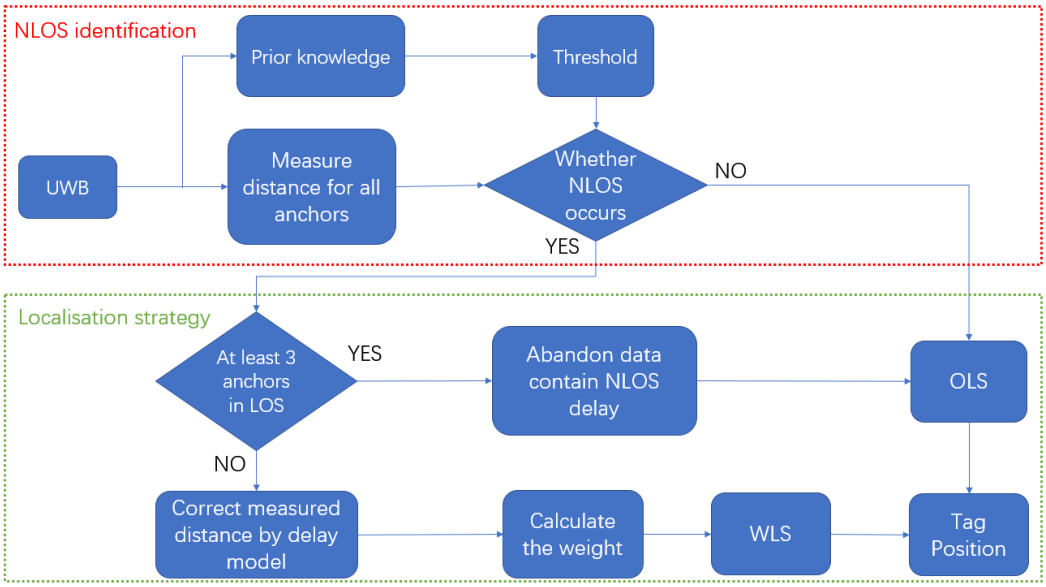

Figure 3.9 Flowchart for the proposed method

This flowchart illustrates the strategy proposed in this chapter to deal with NLOS. The first step is setting a threshold from prior experience to estimate whether NLOS occurs. If no measurement is affected by NLOS, the tag's position can be computed directly using the OLS range measurements. If UWB IPS has more than three fixed anchors, even if NLOS happens for some anchors, the OLS algorithm can still accurately position the tag when at least three anchors are in LOS. If the system cannot receive enough LOS range measurements, the delay estimation model will process the NLOS data. The delay model will correct those NOLS errors and estimate the uncertainty of the corrected ranges. Then, WLS is applied to calculate the position of the UWB tags.

The rest of this section is organised as follows. Section 2 presents the algorithms used in this part, including the sliding window method to identify NLOS, the delay model, and position algorithms. Section 3 gives the experiment design and results, which verify to what degree the delay model and WLS can improve the position accuracy. Section 4 discusses the limitation of IPS with only UWB and the future research plan. The last section offers a conclusion.

3.2.2 Algorithms and Modeling

OLS

OLS is the most common approach for mathematical optimisation. The core of this algorithm is minimising the residual to realise the optimal solution. Algorithm 3 demonstrates the OLS method.

Algorithm 3 Calculate Tag Coordinates Using OLS Method

Input:

Anchor coordinates (x_n, y_n) for $n = 1, 2, \ldots, N$

Measured distances $d_1, d_2, \ldots, d_n$

Output:

Tag coordinates (x, y)

Step 1: Construct Matrices

$$A \leftarrow \begin{bmatrix} -2x_1 & -2y_1 & 1 \\ -2x_2 & -2y_2 & 1 \\ \vdots & \vdots & \vdots \\ -2x_N & -2y_N & 1 \end{bmatrix}$$

$$B \leftarrow \begin{bmatrix} d_1^2 - r_1 \\ d_2^2 - r_2 \\ \vdots \\ d_N^2 - r_N \end{bmatrix} \text{ where } r = x^2 + y^2$$

Step 2: Compute Coordinates Using LS Method

$X \leftarrow (A^T A)^{-1} A^T B$

Step 3: Extract Tag Coordinates

$(x, y, r) \leftarrow X$

return (x, y)

Equation 3.15 describes the relationship between the anchors and tag coordinates and the distance between them when using the matrix.

$$\begin{bmatrix} -2x_1 & -2y_1 & 1 \\ \cdots & \cdots & \cdots \\ -2x_n & -2y_n & 1 \end{bmatrix} \begin{bmatrix} x \\ y \\ r \end{bmatrix} = \begin{bmatrix} d_1^2 - r_1 \\ \cdots \\ d_n^2 - r_n \end{bmatrix} \tag{3.15}$$

(x_n, y_n) $n = 1,2,3 \ldots n$ are the coordinates of the corresponding anchor points. d_1, d_2, d_3 represent the respective range measurements between the corresponding anchor points and the tag. The coordinate of the tag is (x,y)

$$r = x^2 + y^2 \tag{3.16}$$

$$AX = B \tag{3.17}$$

The tag coordinates can be obtained by the LS method:

$$X = (A^T A)^{-1} A^T B \tag{3.18}$$

The OLS algorithm treats all measurement values equally and can perform well in LOS environments due to the nearly identical noise level. The measurement noise in NLOS environments will interfere with the range value. Thus, the OLS may not perform well in NLOS. Contrapose that phenomenon, the WLS algorithm may be more suitable for UWB IPSs in NLOS environments.

WLS

This part uses WLS to calculate the tag's coordinate for further improvement in the NLOS scene. In the NLOS environment, the range value may contain a very high measurement error that cannot be directly used for position. Giving corresponding weight to different anchors' range values can improve the position accuracy. The method of determining the weights for each measurement will be explained in detail in Section 3.3.4.

The weight matrix for the measured ranges from anchors can be represented by Equation 3.19.

$$W = diag[W_1, W_2, W_3 \ldots W_n] \tag{3.19}$$

Based on the OLS, the partial derivative equation of WLS is

$$\frac{\partial e^2}{\partial X} \mathrm{W} = 2A^T WAX - 2A^T WB = 0 \tag{3.20}$$

The following equation calculates the tag's coordinates:

$$X = (A^T WA)^{-1} A^T WB \tag{3.21}$$

The premise of applying the WLS algorithm is to identify the NLOS accurately because the weights for range values in LOS and NLOS are significantly different.

Method to Identify NLOS

The proposed method to identify NLOS is based on the variance of the difference in measured distance between two adjacent sample times. The measured distance between anchor and tag at the time n can be modelled as $\hat{d}_n$ which is equal to the actual distance (d_n) plus measurement noise (ε) in the LOS environment. The measured distance in NLOS ($\hat{d}_n$) is equal to the actual distance (d_n) plus measurement noise (ε) superadd delay caused by NLOS (ε_{NLOS}). So, the difference in measured distance between two adjacent time slots can be computed as

$$\Delta\hat{d}_n = \left|\hat{d}_n - \hat{d}_{n-1}\right| = \begin{cases} d_n - d_{n-1} & LOS\ (n-1) \rightarrow LOS\ (n) \\ d_n - d_{n-1} + \varepsilon_{NLOS} & LOS(n-1) \rightarrow NLOS\ (n) \end{cases} \tag{3.22}$$

The UWB module used in this chapter is DecaWave DW1000, which is compliant with IEEE 802.15.4-2011 UWB standard [123]. The sampling frequency is 3Hz, and the highest indoor robot speed is less than 1m/s, so $d_n - d_{n-1}$ should be a tiny number, around a few centimetres, but ε_{NLOS} is around decimetres to a few meters, which is much greater than $d_n - d_{n-1}$. The method of the sliding window of variance of $\Delta\hat{d}_n$ was proposed in this chapter to identify NLOS, which is illustrated in Figure 3.10. The threshold used to estimate the NLOS is the variance of $\Delta\hat{d}_n$ measured in a LOS environment (Var($\Delta\hat{d}_n$ (LOS)))

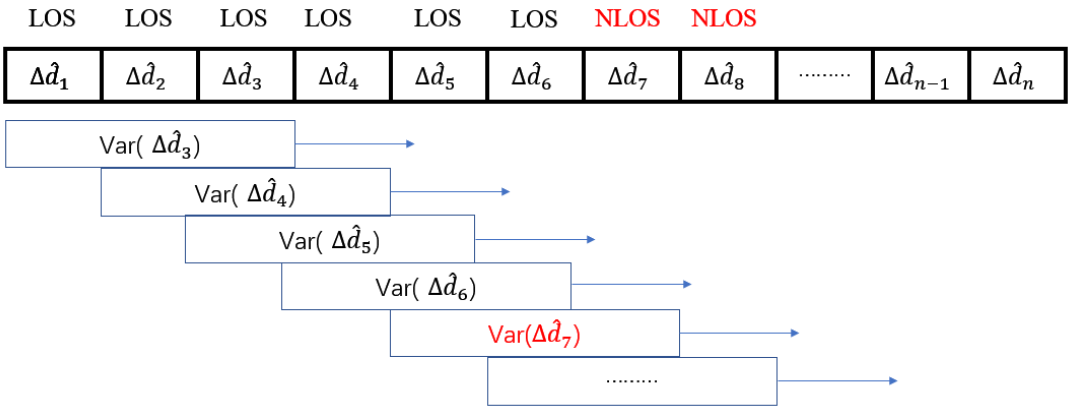

Figure 3.10 Sliding window method for NLOS identification

For further annotation of this method, shown in Figure 3.10, when a tag was not in NLOS until time slot n, the Var($\Delta\hat{d}_n$)) will suddenly increase due to the measured distance d_n, adding a huge NLOS error. Indeed, the value of Var($\Delta\hat{d}_n$) will be significantly greater than the threshold. Detecting that the Var($\Delta\hat{d}_n$) is bigger than the threshold, which means this measured data would most probably be affected by NLOS. Due to the high measurement noise in NLOS, the measurement range will keep jittering over an extensive range, leading to the value of Var($\Delta\hat{d}$) being still greater than the threshold in this situation. If the tag is back to LOS from NLOS at time slot k, the value of Var($\Delta\hat{d}_{k+3}$) will have a significant drop and be smaller than the threshold. The experiment will verify this strategy to identify the NLOS.

Delay Model for NLOS Mitigation

This part mainly focuses on the NLOS caused by walls. The strategy to compensate for the NLOS delay is to derive a delay model from the measured distance in the NLOS condition. The following Figure 3.11 illustrates the geometric model.

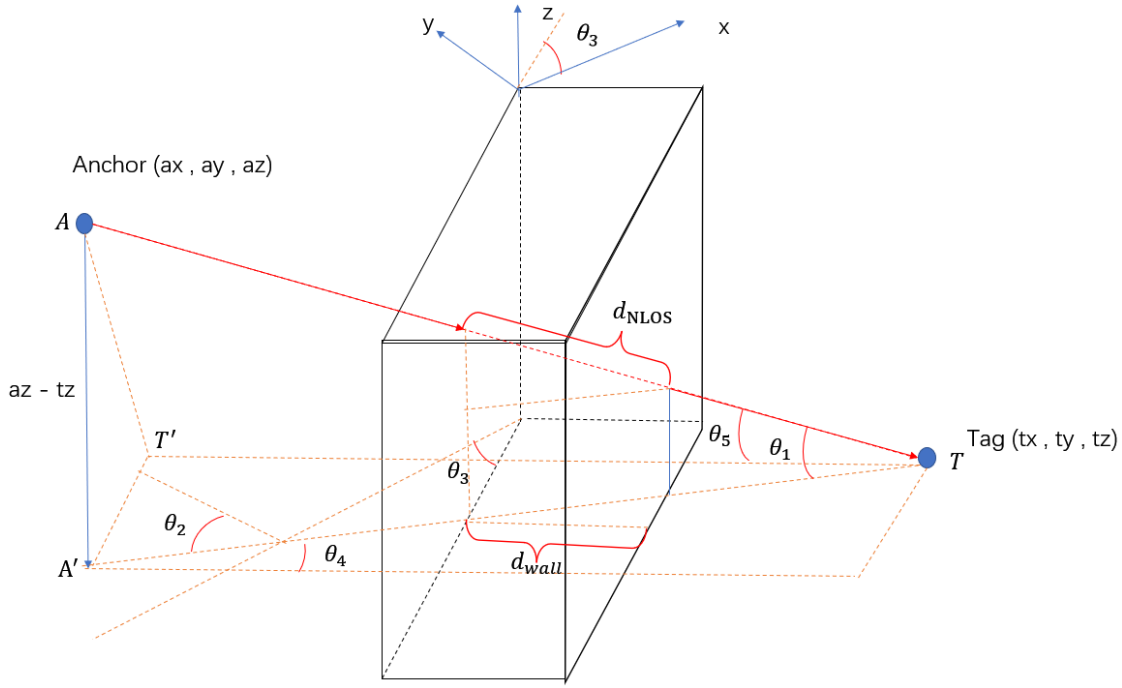

Figure 3.11 Delay model for a wall

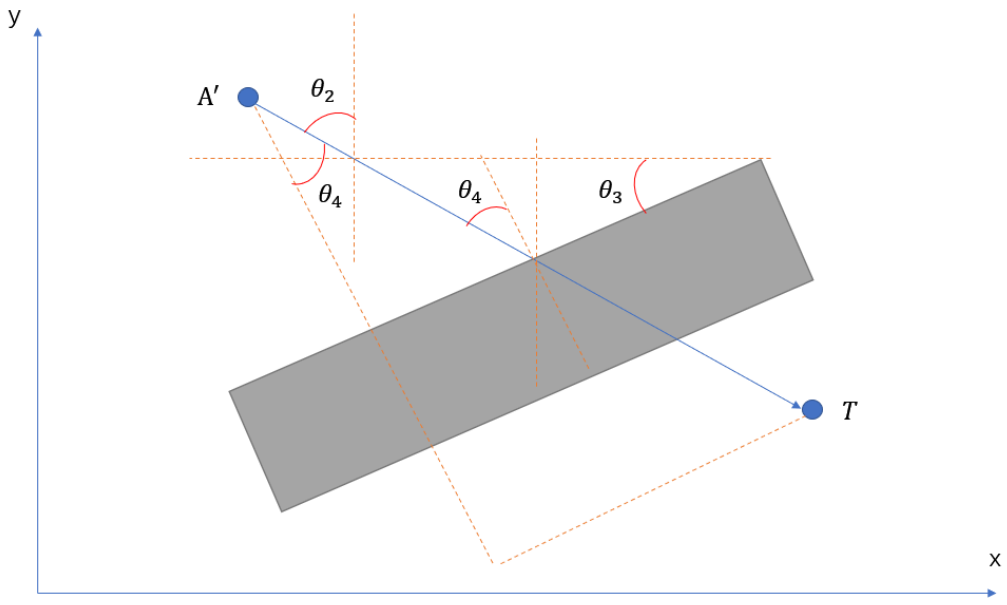

Figure 3.12 Projective image

Figures 3.11 and 3.12 show a universal model for all kinds of NLOS caused by a wall. In this model, the wall has an angle θ_3 between the positive x-axis, anchors and tags are at different heights, where A and T represent the anchor and tag points, respectively. Line TT' is perpendicular to the wall and AT' is perpendicular to TT', A' is the projection point of A on plan $y = tz$, θ_1 is the

angle between line AT and AT', θ_2 is the angle between line AT' and positive y-axis, θ_4 is the angle between the normal of the wall and $A'T$, θ_5 is the angle between the normal of the wall and AT, d_{wall} is the thickness of the wall, and d_{NLOS} is the actual distance of UWB signal propagation in the wall.

The primary factors leading to NLOS errors are the electrical permittivities and the thickness of a material when the UWB signal propagates through this obstacle. The electrical permittivity for a wall is a constant number in this experiment, and the relative thickness of the wall is increased with the incident angle increasing when the UWB signal penetrates the wall. The NLOS delay model is defined in Equation 3.23.

$$\Delta d_{NLOS} = A * d_{NLOS} * \left(\sqrt{\epsilon_{wall}} - 1\right) + B \tag{3.23}$$

where Δd_{NLOS} is the NLOS delay caused by a wall, and ϵ_{wall} is the permittivity of the wall.

$$d_{NLOS} = \frac{d_{wall}}{cos\theta_4 * cos\theta_1} = \frac{d_{wall}}{cos\theta_5} \tag{3.24}$$

$$\theta_1 = \arcsin\left(\frac{|az - tz|}{\sqrt{(ax - tx)^2 + (ay - ty)^2 + (az - tz)^2}}\right) \tag{3.25}$$

$$\theta_2 = \arctan\left(\frac{|ax - tx|}{|ay - ty|}\right) \tag{3.26}$$

The relationship between θ_4, θ_2 and θ_3 showing in Equation 3.27

$$\theta_4 = \begin{cases} \theta_2 - \theta_3 & if\ \theta_2 > \theta_4 \\ \theta_2 + \theta_3 & if\ \theta_2 \leq \theta_4 \end{cases} \tag{3.27}$$

The delay model is defined as follows:

$$\Delta d_{NLOS} = A * \frac{d_{wall} * \left(\sqrt{\epsilon_{wall}} - 1\right)}{cos\theta_5} + B \tag{3.28}$$

The measured data were used to ascertain the coefficients A and B in Equation 3.28. A tag was placed in 45 different positions with various incident angles covering the range from 0° to 80°, and the LOS path was blocked by different wall thicknesses (0.16m and 0.26m) with permittivity setting to 5.5. At least 60

samples were taken at each position. By computing the fitting equation from those more than 2,700 data, the coefficients of A equals 0.3459 and B equals 0.2722 were determined. Consequently, the corrected distance can be calculated by subtracting the NLOS delay from the measurement ranges. Algorithm 4 below describes how to model the NLOS error for a wall.

Algorithm 4 NLOS Delay Model (3D)

Input:

Anchor coordinates (a_x, a_y, a_z)
Tag coordinates (t_x, t_y, t_z)
Wall thickness d_{wall}
Permittivity of the wall ε_{wall}
Model parameters A, B

Output:

NLOS delay Δd_{NLOS}

Step 1: Calculate Angles

$$\theta_1 \leftarrow \arcsin\left(\frac{|a_z - t_z|}{\sqrt{(a_x - t_x)^2 + (a_y - t_y)^2 + (a_z - t_z)^2}}\right)$$

$$\theta_2 \leftarrow \arctan\left(\frac{|a_x - t_x|}{|a_y - t_y|}\right)$$

$$\theta_4 \leftarrow \begin{cases} \theta_2 - \theta_3, & \text{if } \theta_2 > \theta_4 \\ \theta_2 + \theta_3, & \text{if } \theta_2 \leq \theta_4 \end{cases}$$

$$\theta_5 \leftarrow \theta_4$$

Step 2: Calculate Delay

$$d_{NLOS} \leftarrow \frac{d_{wall}}{\cos(\theta_4) \cdot \cos(\theta_5)}$$

$$\Delta d_{NLOS} \leftarrow A \cdot d_{NLOS} \cdot \left(\sqrt{\varepsilon_{wall} - 1}\right) + B$$

return Δd_{NLOS}

Since the anchors and tags are likely to be at different heights in practical applications, this part of the algorithm is based on the previous 2D algorithm and proposes a more general 3D NLOS error model. This model can calculate the NLOS error from the constants and variables A and B, wall thickness, dielectric constant, and angle of incidence. The present error model has great potential to be applied to other types of obstructions when sufficient experimental data are available for modelling obstructions to determine the corresponding coefficients. In the following experiments, the Tag communicates with different anchor points during its movement along the reference path, and the NLOS error occurs due to wall obscuration. The A, B, dielectric constant and wall thickness are changed

according to different walls, and the signal's angle of incidence changes with the Tag's movement. The following experiments can fully verify whether the proposed error model can accurately calculate the NLOS error.

3.2.3 Experiment and Results

Experimental Environments and Equipment

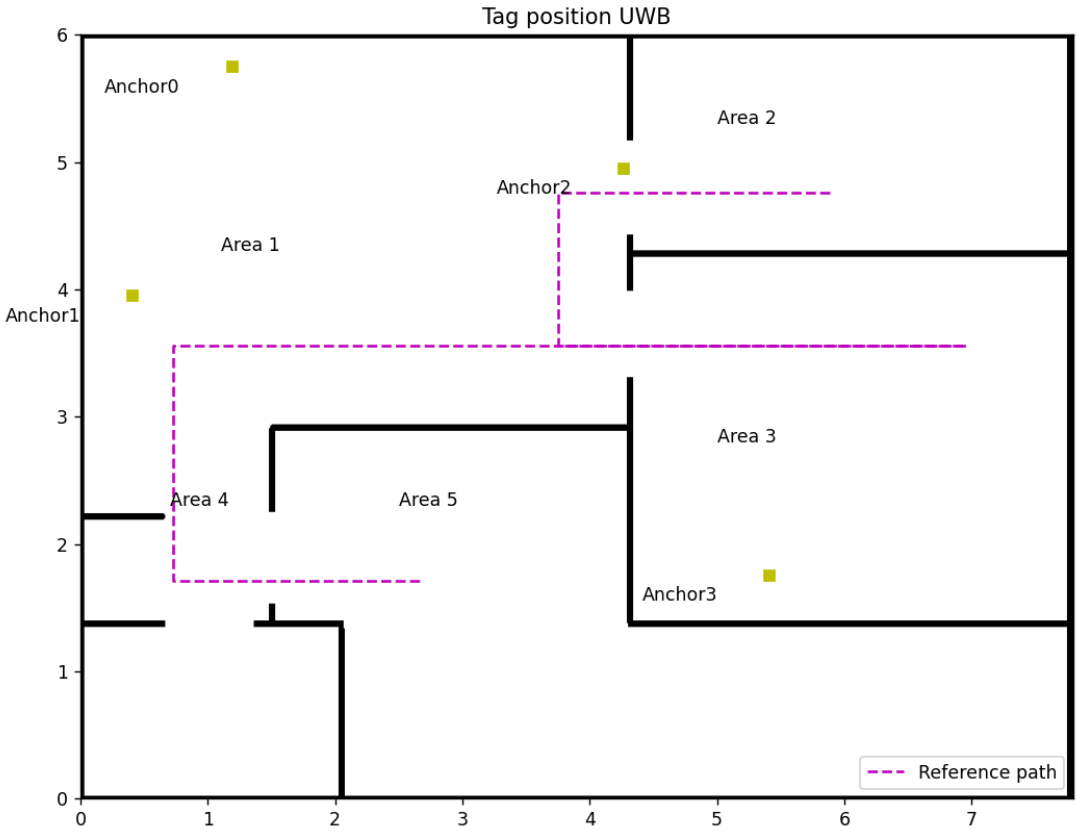

a) Map of Experiment 1

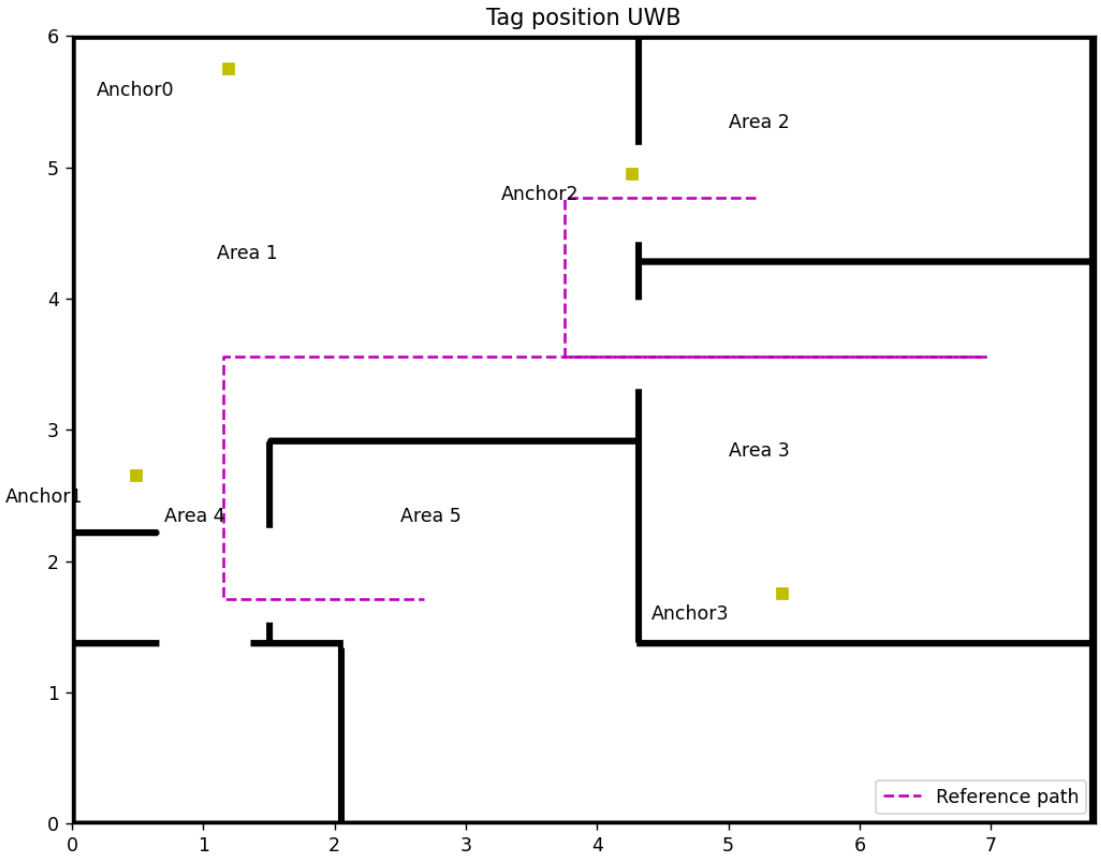

b) Map of Experiment 2

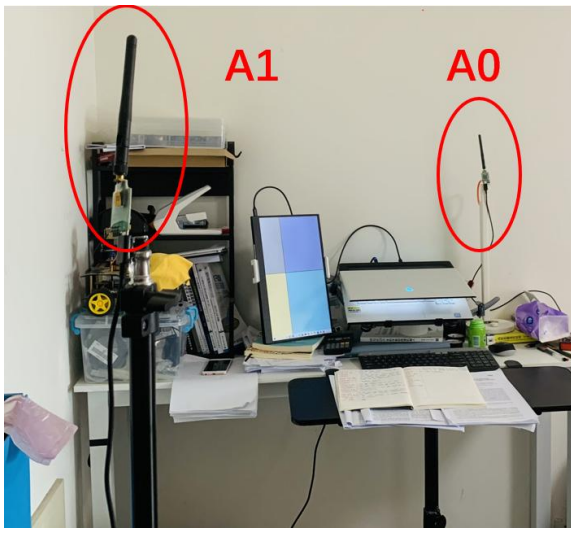

c) Anchor 0 & 1

d) Anchor 2

e) Anchor 3

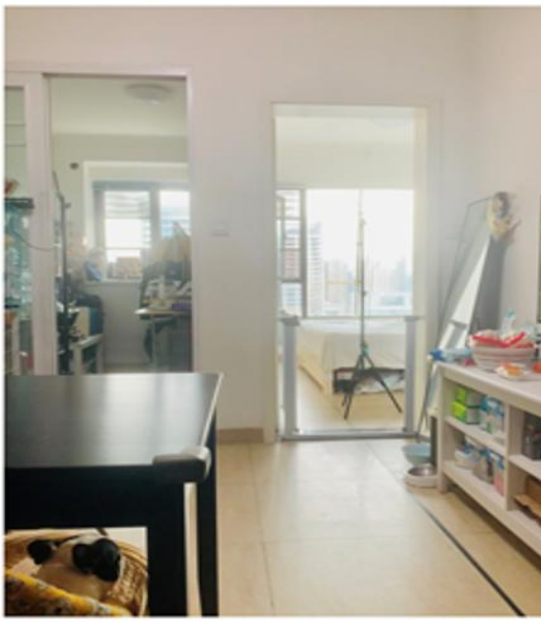

f) Experiment site

Figure 3.13 Experiment design: a) Map of Experiment 1, b) Map of Experiment 2, c) Anchor 0 & 1, d) Anchor 2, e) Anchor 3, f) Overall experiment environment

This experiment is conducted in an apartment (Fig. 3.23 (e)) with the following dimensions: 7.8m wide and 5.848m long, as shown in Figures 3.13 a) and b). Four fixed anchors (Fig. 3.23 c,d and e) are mounted in different positions, represented by the yellow square in Figure 3.13 a) and b). The coordinates of Anchors 0, 1, 2, and 3 for experiment 1 are (1.19, 5.75, 1.5), (0.41, 3.95, 1.5), (4.27, 4.95, 1.5), (5.41, 1.75, 1.5), respectively. In Experiment 2, the coordinate of Anchor 1 changes to (0.49, 2.65, 1.5), leading to only one LOS anchor in Area 3. These two experiments cover all conditions of NLOS anchor numbers in UWB IPS, shown in Table 3.7. The purple lines in Fig. 3.23 a) and b) are the reference paths, which start from Area 2 to Area 3 through Area 1 and then go back to the endpoint at Area 5 through Area 1 and 4 when reaching the stop point in Area 3. The height of the tag is 1.1m, which is a 0.4m height difference from fixed anchors.

Table 3.7 Anchors in NLOS in different areas

	Area 1	Area 2	Area 3	Area 4	Area 5
Anchor (NLOS-Experiment 1)	3	3	0 & 2	2 & 3	0, 1, 2 & 3
Anchor (NLOS-Experiment 2)	3	3	0, 1 & 2	2 & 3	0, 1, 2 & 3

Experimental Results for Identifying NLOS

The abovementioned method was used in two experiments to identify the NLOS for all anchors when a tag moves along the reference path. The results are presented in the following two sections.

Experiment 1

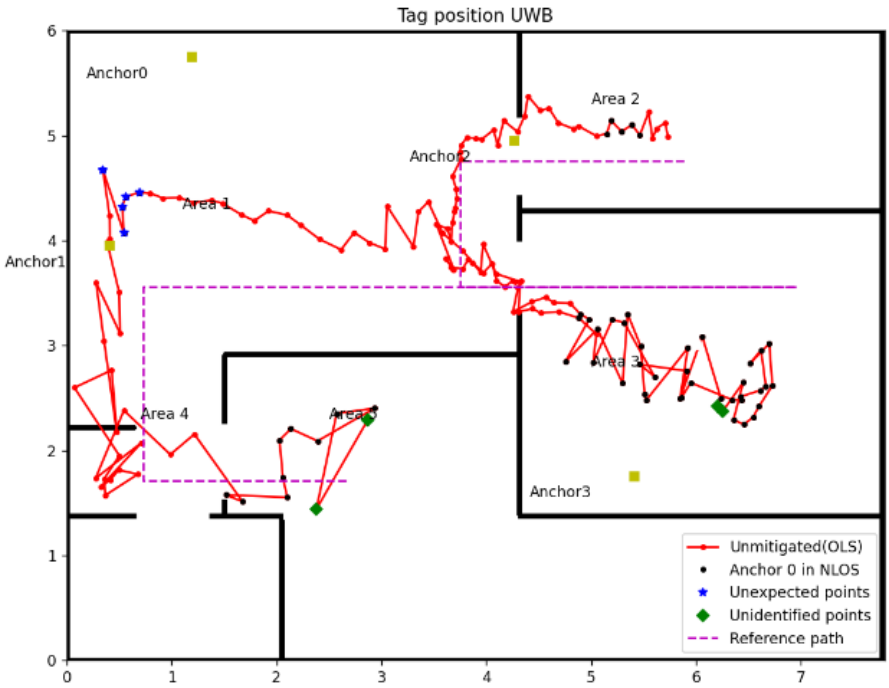

a) Identification result for Anchor 0

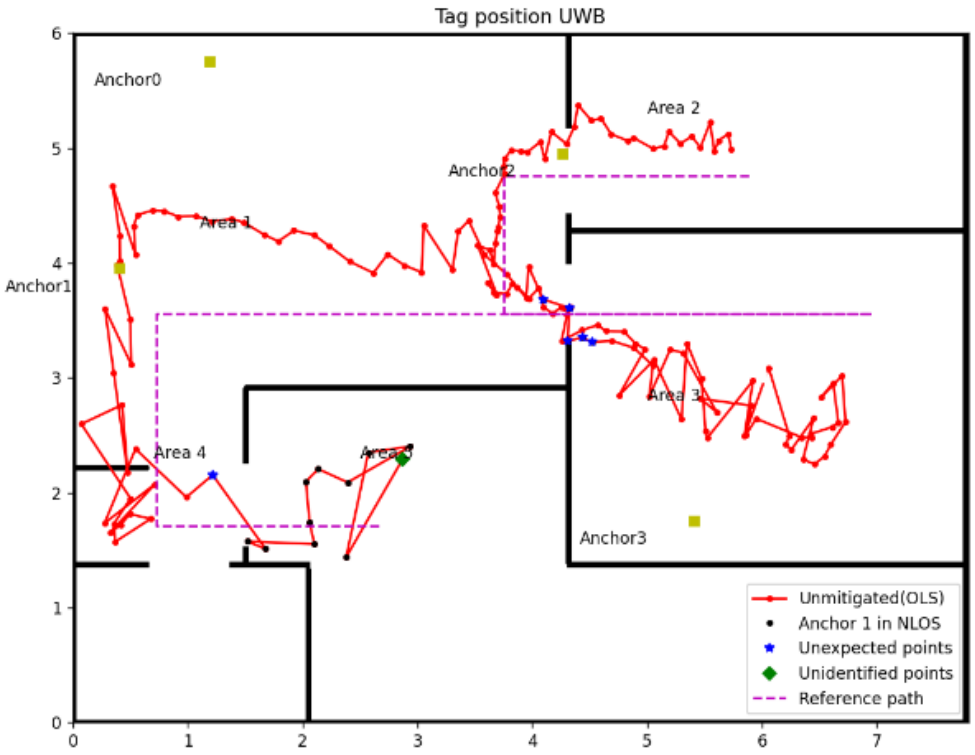

b) Identification result for Anchor 1

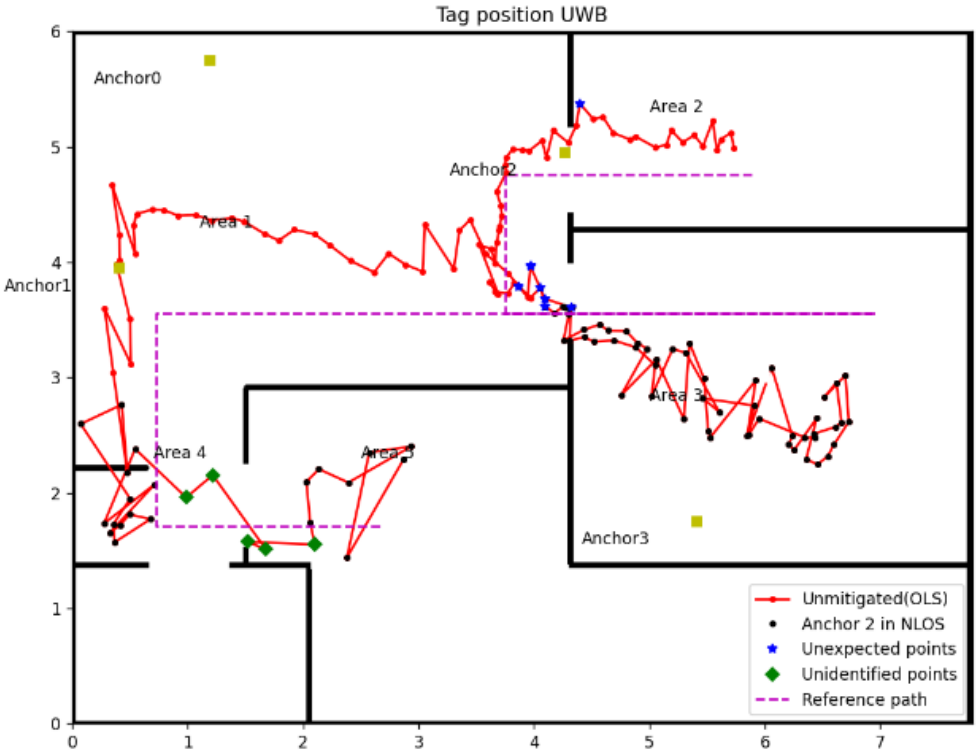

c) Identification result for Anchor 2

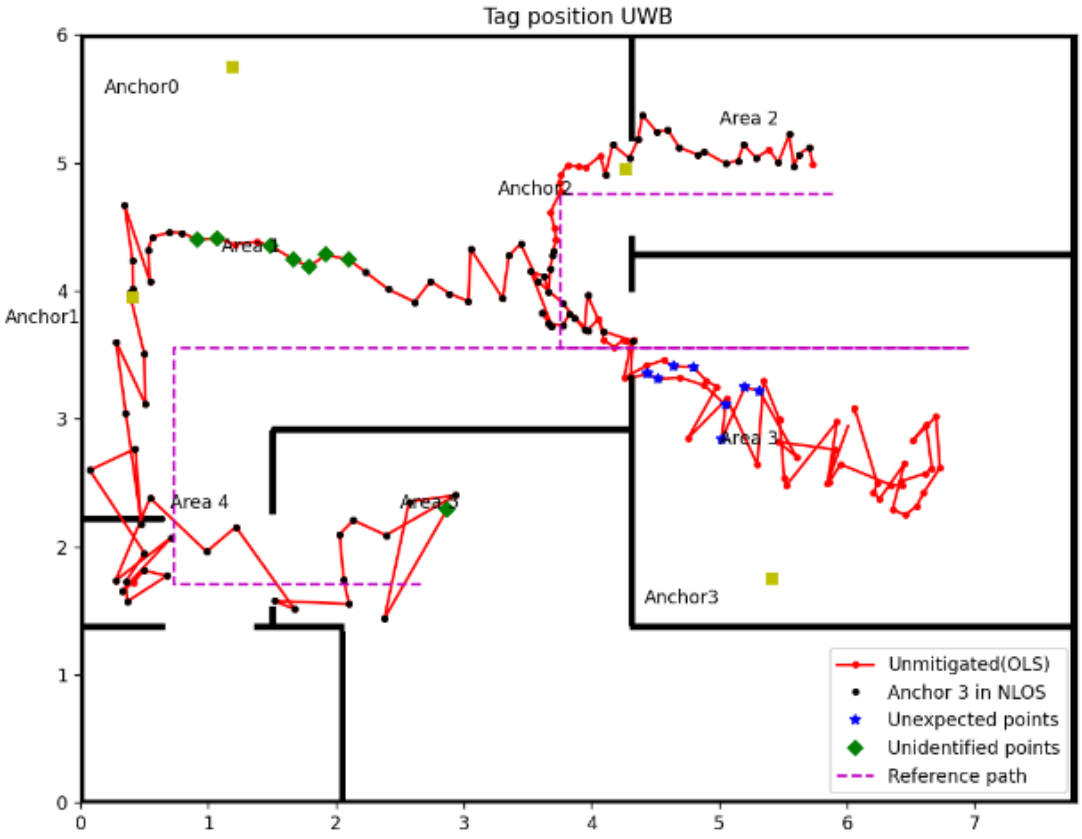

d) Identification result for Anchor 3

Figure 3.14 NLOS identification result (Experiment 1): a) Anchor 0, b) Anchor 1, c) Anchor 2, d) Anchor 3

Figure 3.14 shows the result of NLOS identification for four anchors, and the accuracy of identification is shown in the following table, Table 3.8:

Table 3.8 The accuracy rate of NLOS identification (Experiment 1)

Anchor	**Anchor 0**	**Anchor 1**	**Anchor 2**	**Anchor 3**
Identification rate	94.47%	95.71%	92.64%	90.18%

Experimental 2

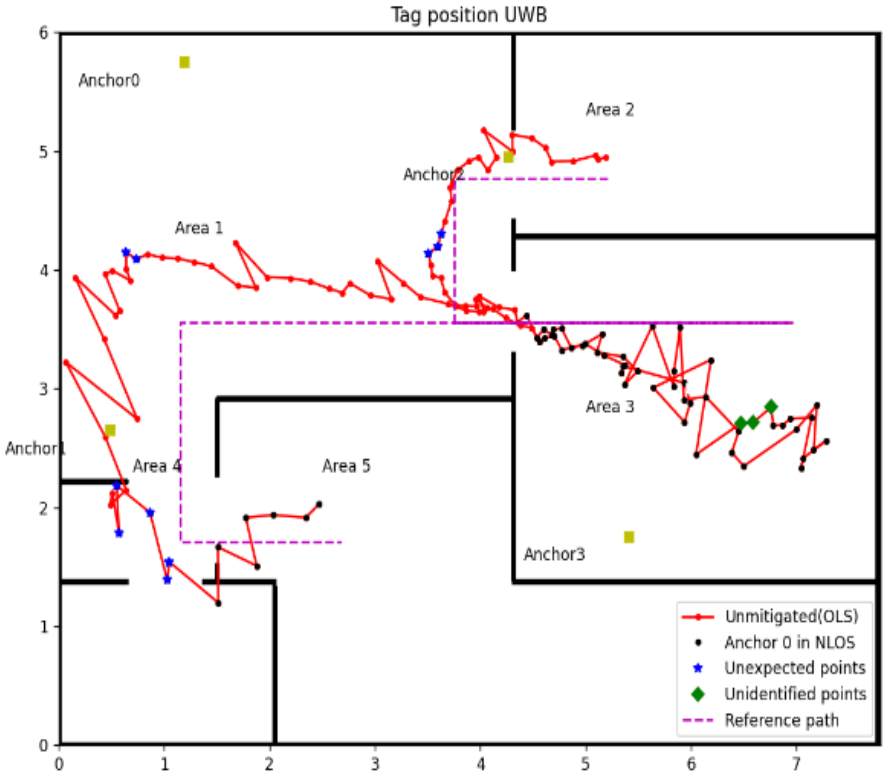

a) Identification result for Anchor 0

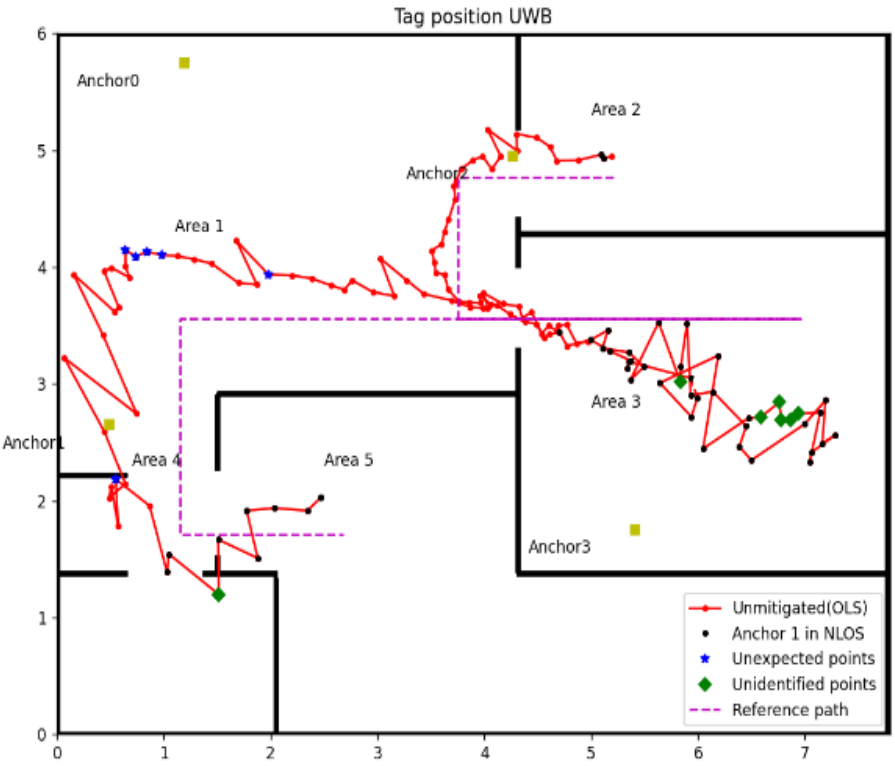

b) Identification result for Anchor 1

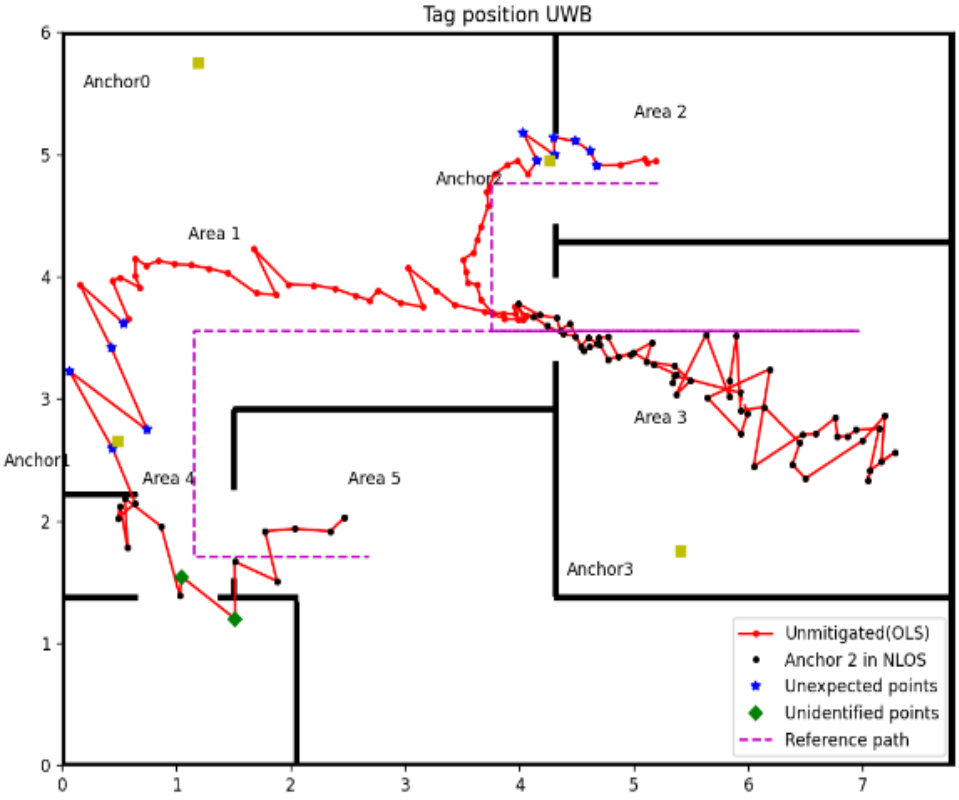

c) Identification result for Anchor 2

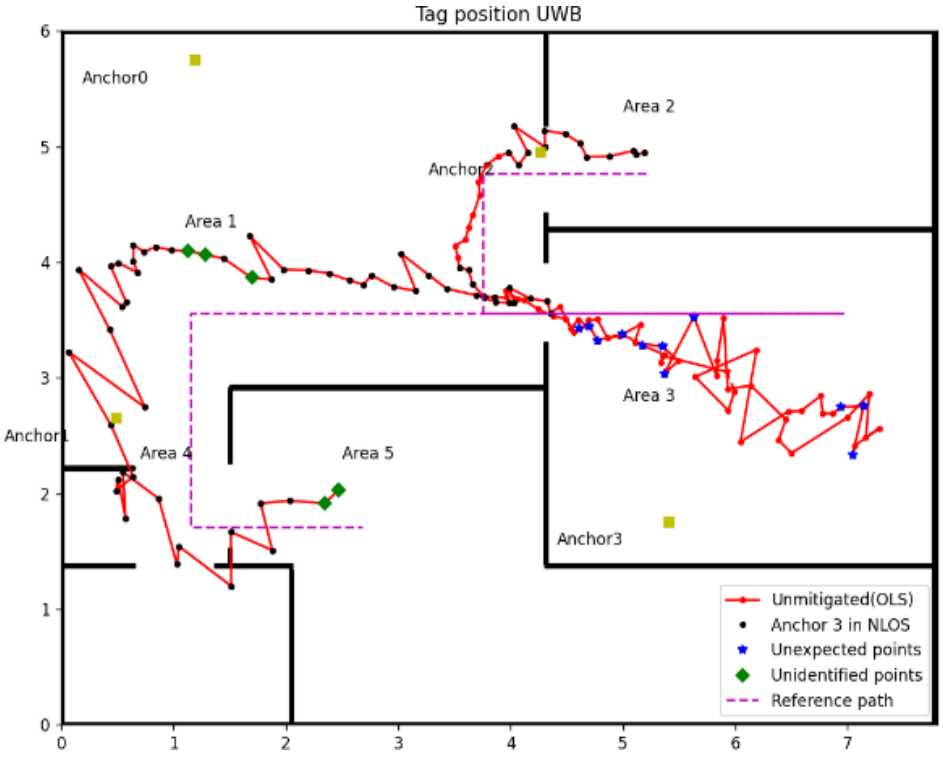

d) Identification result for Anchor 3

Figure 3.15 NLOS identification result (Experiment 2): a) Anchor 0, b) Anchor 1, c) Anchor 2, d) Anchor 3

Table 3.9 The accuracy rate of NLOS identification (Experiment 1)

Anchor	**Anchor 0**	**Anchor 1**	**Anchor 2**	**Anchor 3**
Identification rate	90.71%	90.71%	90%	88.65%

Figures 3.14 and 3.15, Tables 3.8 and 3.9 show that the method proposed in this chapter is relatively accurate. The worst accuracy of the NLOS identification case is the Anchor 3 in both experiments, which is 90.18% and 88.65%, respectively. The accuracy of other anchors is all over 90% in both experiments.

The misidentified case includes cases in NLOS that were not recognised and in LOS but misjudged into NLOS, which named unidentified points and unexpected points in Figures 3.14 and 3.15, respectively. The complex experiment environment, containing computers, desks, chairs and other factors, will increase the impact of multipath, which may lead to some unexpected points. The velocity of the tag is small during the turning, which is the possible reason for the unidentified point. Considering the impact of the factors above, this accuracy rate of NLOS identification is quite acceptable.

Mitigation Results for Delay Model (Experiment 1)

The experiment applies different position algorithms based on the number of NLOS in the corresponding areas. According to the reference path and anchors' position in Experiment 1, Area 1 has three anchors in LOS (Anchors 0, 1 and 2), which are enough to locate the tag accurately. For Area 2, the delay model was used to correct the range measured by Anchor 3. When the tag moves in Area 3, a 0.26m concrete wall will block the UWB signal from Anchors 0 and 2, and the delay model is also applied to those measured data containing NLOS errors. In Area 4, using the range data from Anchors 0 and 1, which are in LOS, two coordinates for the tag can be computed, and then the range data of Anchor 2 or

Anchor 3 can be used to select the tag's actual coordinate. The worst scenario is in Area 5; the delay model must correct all four anchors in NLOS since a 0.16m concrete wall blocked all the UWB signals. Figure 3.16 and Table 3.10 show the experiment's results.

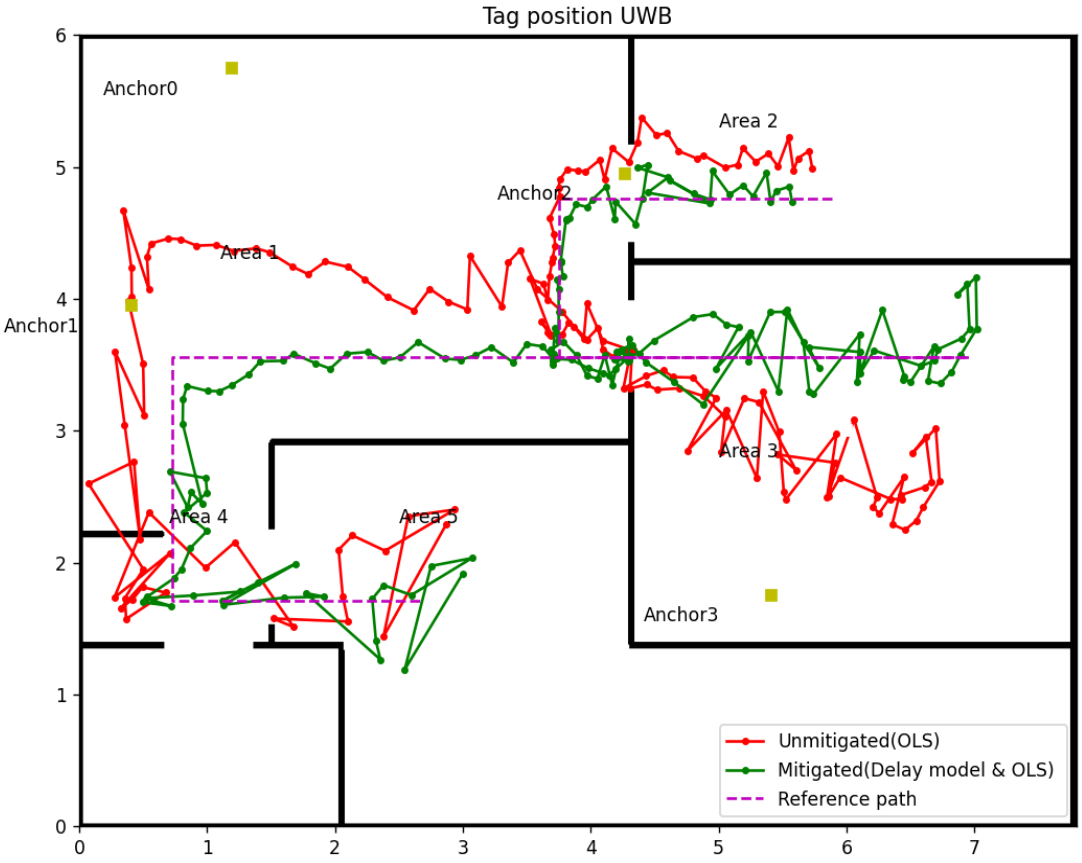

Figure 3.16 Tag position after mitigating by delay model with OLS

Table 3.10 Position accuracy analysis for delay model

Position error	**Area 1 (3 LOS Anchors)**		**Area 2 (3 LOS Anchors)**		**Area 3 (2 LOS Anchors)**		**Area 5 (0 LOS Anchors)**	
	OLS	**OLS (LOS only)**	**OLS**	**Delay model & OLS**	**OLS**	**Delay model & OLS**	**OLS**	**Delay model & OLS**
Max (m)	0.849	0.361	0.616	0.257	1.313	0.603	0.692	0.521

Min (m)	0.048	0.004	0.212	0.003	0.153	0.016	0.033	0.013
Average (m)	0.499	0.075	0.349	0.094	0.786	0.201	0.339	0.213
RMSE (m)	0.555	0.106	0.364	0.126	0.853	0.244	0.398	0.276

Figure 3.16 visually illustrates the effectiveness of the delay model proposed in this section. The green line with the dot in Figure 3.16 shows the tag position and trajectory computed by the measured distance after the delay model correction. It explicitly shows that the position accuracy of the tag was improved in Areas 2, 3, and 5, which applies the delay model to correct data with NLOS delay. Table 3.10 is a detailed analysis of the experiment's results. The first column of Area 1 is the position error using raw data from three LOS anchors (Anchors 0, 1 and 2) and one NLOS anchor (Anchor 3). The second column in Area 1 is the position error only using the range data from those three LOS anchors, and this group data can be used as the control group. It can be found that the NLOS error has a massive impact on position accuracy. With Anchor 3's NLOS error in Area 1, the maximum position error is over 0.8m, and RMSE is 0.555m. The UWB IPS performed better position accuracy after abandoning the range data from Anchor 3, and the maximum error and RMSE were reduced to 0.361m and 0.106m, respectively. The delay model minimises the affection of NLOS for areas that do not have enough LOS data to locate the tag. From Table 3.10, RMSE was reduced from 0.364m to 0.126m in Area 2, from 0.853m to 0.244m in Area 3, and from 0.398m to 0.276m in Area 5. A similar phenomenon of decreasing error occurs in average and maximum errors, too. The position accuracy of UWB IPSs in NLOS after correction by the delay model is approaching the accuracy in LOS. Another phenomenon that can be found in Figure 3.16 is the location point of the tag in Area 3, which disperses more widely with the growth of the incident angle. So, the WLS was used in the next step to eliminate the effection of heteroscedasticity.

Mitigation Results for Delay Model with WLS (Experiment 1)

The crucial part of WLS is to determine the exact weight for measured distance at different incident angles. The tag position kept jittering due to the measurement range affected by the noise, even though the tag was motionless. The jitter margin of range measurement positively correlates with the incident angle in NLOS caused by a wall. Thus, the variance of the range measurements in a position can be the weight's reference.

In this experiment, the weight for measured distance from the fixed Anchors 0, 1, 2 and 3 can be represented as

$$W = diag[W_0, W_1, W_2, W_3] \tag{3.29}$$

Setting the variance of measured distance in LOS as the criterion, the weight can be computed by the following equation when the tag in NLOS with the incident angle θ:

$$W_\theta = \frac{Var(d_{LOS})}{Var(d_\theta)} \tag{3.30}$$

where $Var(d_{LOS})$ is the variance of measured distance in LOS, $Var(d_\theta)$ is the variance of measured distance in NLOS with the incident angle θ, and W_θ is the weight for this NLOS measurement range.

Algorithm 5 below describes the WLS algorithm that assigns corresponding weights to different ranging values based on the incidence angle.

Algorithm 5 Weighted Least Squares (WLS) with Angular Weights

Input:

Anchor coordinates (a_x, a_y, a_z)
Tag coordinates (t_x, t_y, t_z)
Measured distances $d_1, d_2, \ldots, d_n$
LOS variance $\mathrm{Var}(d_{LOS})$
NLOS variance $\mathrm{Var}(d_\theta)$ for each θ

Output:

Tag coordinates (x, y)

Step 1: Calculate Angular Weights

for each measurement d_θ at angle θ **do**
$W_\theta \leftarrow \frac{\mathrm{Var}(d_{LOS})}{\mathrm{Var}(d_\theta)}$
end for
Construct diagonal weight matrix:
$W \leftarrow \mathrm{diag}(W_\theta)$

Step 2: Construct Matrices for WLS

$$A \leftarrow \begin{bmatrix} -2a_x & -2a_y & 1 \\ -2a_x & -2a_y & 1 \\ \vdots & \vdots & \vdots \\ -2a_x & -2a_y & 1 \end{bmatrix}$$

$$B \leftarrow \begin{bmatrix} d_1^2 - r_1 \\ d_2^2 - r_2 \\ \vdots \\ d_n^2 - r_n \end{bmatrix} \text{ where } r = x^2 + y^2$$

Step 3: Apply WLS Formula

$X \leftarrow (A^T W A)^{-1} A^T W B$

Step 4: Extract Tag Coordinates

$(x, y, r) \leftarrow X$
return (x, y)

In order to find the relationship between weight and incident angle, 30 groups of data were gathered, which covered incident angles from 0° to 70°. Each group of data contains at least 60 samples, so $Var(d_\theta)$ can be computed for each angle group, and the weight for different incident angles can be drawn from Equation 3.30. The following figure, Figure 3.17, illustrates the relationship between the incident angle and the weight.

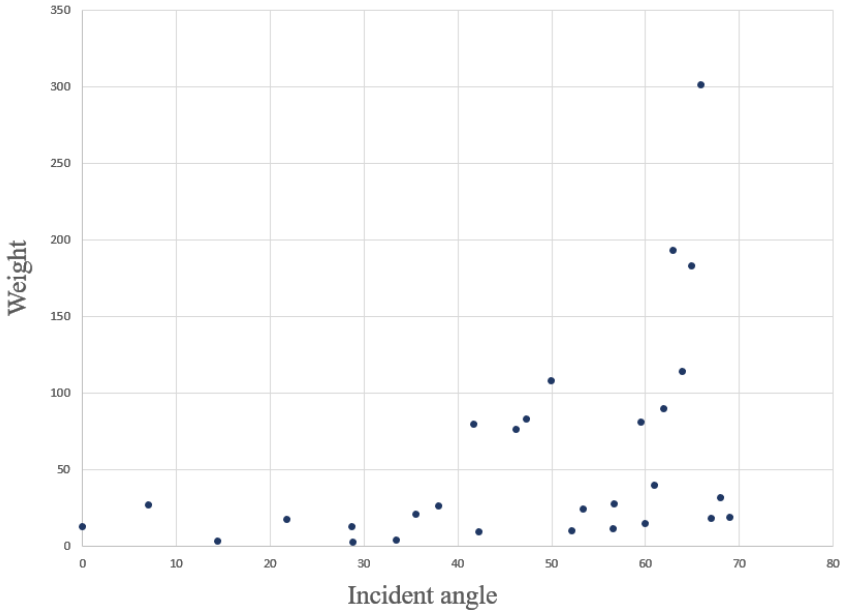

Figure 3.17 Relationship between θ and the W_θ

The experiment in this part uses the same measured range data from the previous section. According to the relationships between θ and the W_θ, corresponding weight to the measured range was assigned. The measured range with weight can calculate the tag's position by Equation 3.21. Figure 3.18 and Table 3.11 show the position results of the delay model with the WLS algorithm.

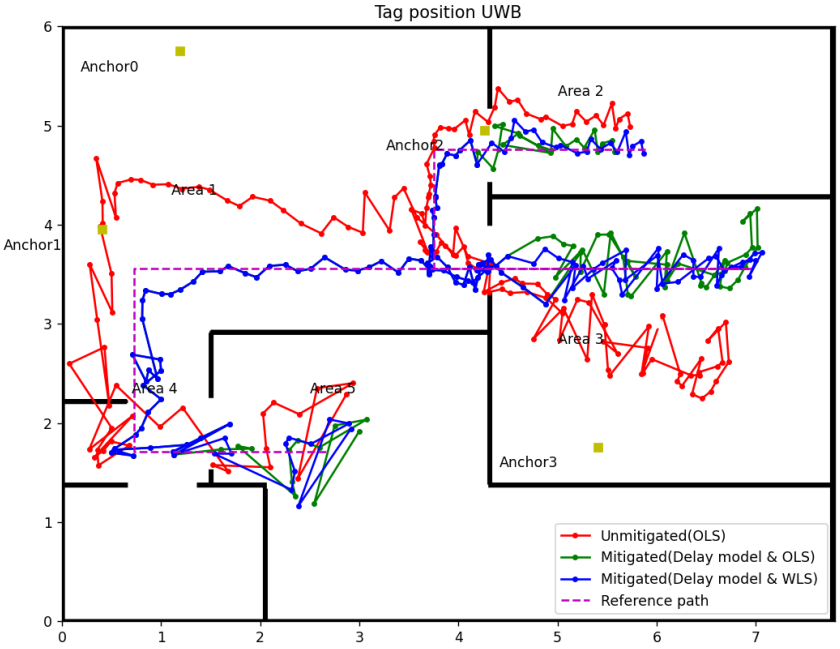

Figure 3.18 Experiment 1 results for the delay model with WLS

Table 3.11 Position accuracy analysis for delay model with WLS (Experiment 1)

Position error	Area 2 (3 LOS Anchors)		Area 3 (2 LOS Anchors)		Area 5 (0 LOS Anchors)	
	Delay model& OLS	Delay model& WLS	Delay model& OLS	Delay model& WLS	Delay model& OLS	Delay model& WLS
Max (m)	0.257	0.259	0.603	0.319	0.521	0.547
Min (m)	0.003	0.003	0.016	0.002	0.013	0.019
Average (m)	0.094	0.083	0.201	0.112	0.213	0.207
RMSE (m)	0.126	0.111	0.244	0.132	0.276	0.265

The blue line with the dot in Figure 3.18 is the tag position calculated by the WLS algorithm. Compared with the green line (OLS algorithm), the position accuracy of WLS shows significant improvements in Areas 2 and 3; also, the detailed data analysis in Table 3.11 attests to this. In Area 3, the WLS significantly enhances the position precision, the maximum position error has a nearly 0.3 m reduction (0.603m to 0.319m), and the RMSE reduces from 0.244m (OLS) to 0.132m (WLS). The maximum position errors were almost equal in Areas 2 and 5, and the average errors and RMSEs slightly decreased using the WLS algorithm. Even the WLS algorithm did not contribute generously to the maximum error, but from average error and RMSE, the position accuracy was improved overall. Hence, applying WLS further enhances the accuracy and precision of the UWB IPSs in NLOS environments.

Mitigation Results for Delay Model with WLS (Experiment 2)

To further verify the affection of the delay model and WLS algorithm, an improved experiment was designed in which the coordinates of Anchor 1 were changed to (0.49, 2.65, 1.5), resulting in only one LOS anchor in Area 3. That means the condition for UWB IPSs in Area 3 will be harsher than in Experiment

1. Figure 3.19 illustrates the coordinates of anchors (yellow square), reference path (purple dot line), and experiment results (red, green, and blue line).

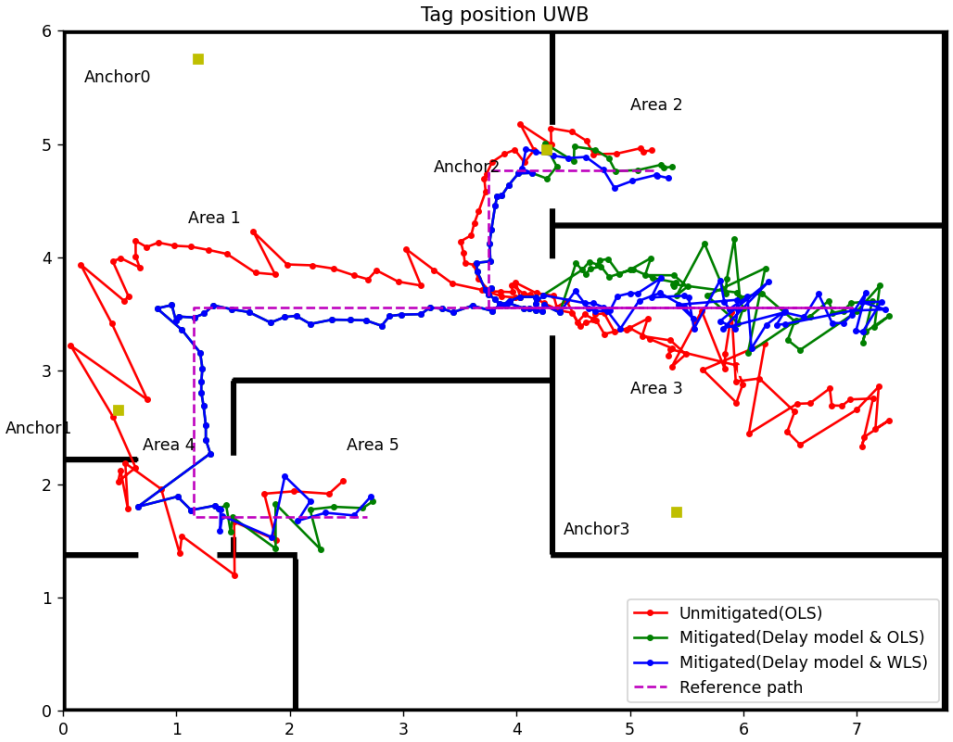

Figure 3.19 Experiment 2 results for the delay model with WLS

Table 3.12 Position accuracy analysis for delay model with WLS (Experiment 2)

Position error	**Area 2 (3 LOS Anchors)**		**Area 3 (2 LOS Anchors)**		**Area 5 (0 LOS Anchors)**	
	Delay model& OLS	**Delay model& WLS**	**Delay model& OLS**	**Delay model& WLS**	**Delay model& OLS**	**Delay model& WLS**
Max (m)	0.257	0.259	0.603	0.319	0.521	0.547
Min (m)	0.003	0.003	0.016	0.002	0.013	0.019
Average (m)	0.094	0.083	0.201	0.112	0.213	0.207
RMSE (m)	0.126	0.111	0.244	0.132	0.276	0.265

In Figure 3.19, the red line represents the tag's position and trajectory computed by OLS using raw range data, which uses the same strategies as in experiment 1.

The green and blue lines represent the position and trajectory of the tag, for which the delay model corrected the range data but used OLS and WLS to compute the position, respectively. The main difference between this experiment and Experiment 1 is in Area 3. By changing the coordinate of Anchor 1, the tag in Area 3 can only receive one LOS UWB signal. Even so, the delay model and the WLS can mitigate the NLOS error well, which can be observed from the contrast of the three trajectories. Detailed data can be found in Table 3.12. The second column data in Area 1 is data analysis for the tag's position using only three LOS anchors' range information, which can be the evaluation criteria for other groups. In Area 2, there is only Anchor 3 in NLOS, but this NLOS delay still leads to a maximum 0.416 m position error, the average error and RMSE all being over 0.2 m. After using the delay model to correct the range data of Anchor 3, the maximum error is reduced to 0.247m; the average error and RMSE are around 0.1m, following the OLS algorithm. Changing the position algorithm to WLS can further improve the accuracy of the tag; the maximum error is only 0.195m, and the average error and RMSE can reach the control group's performance in Area 1 in LOS.

In Area 3, despite moving Anchor 1 to the NLOS environment, the position accuracy remains largely untouched by this change compared to Experiment 1. The reason may be that two walls entirely block the direct path between the tag and Anchor 1, but by multipath, the tag and Anchor 1 still have regular communication. Accordingly, the measurement error of Anchor 1 should be stable, not leading to a vast negative impact on position accuracy.

For other areas, the order of the performance of those position algorithms is that the delay model with WLS is the best, and then the delay model with OLS is better than OLS only. However, in Area 5, there is one exception: the maximum error of the delay model with WLS is 0.359m, which is bigger than the 0.284m of the delay model with OLS. The inappropriate weight of some points may cause this

exception due to the complex indoor environments. In summary, the delay model with WLS algorithms can enhance the overall accuracy and precision of the UWB IPS in the NLOS environment.

3.2.4 Discussion

Even though the performance of the delay model with the WLS algorithm is close to the LOS level, the RMSEs in Tables 3.11 and 3.12 are all over 0.1m in Areas 2, 3 and 5. Moreover, the jitter margin of the tag's position in those NLOS areas is still more significant than in the LOS environment. So, some inherent defects have restricted the application of IPS to only using UWB technology. For instance, in the experiment environment, if the tag in Area 5 moves forward to the far right of the map, the communication between the tag and some anchors will be severed by more than one wall or some metals (e.g., refrigerator, metal cabinet, rebar in the load-bearing wall). Therefore, the UWB IPS can not provide the tag position because of the lack of measured range data in the hash indoor environment.

The same situation happened in Area 4; two walls blocked the signal from Anchors 2 and 3. The delay model and WLS algorithms cannot handle the data like this. Therefore, in Area 4, we use a different strategy to calculate the tag position. In Area 4, the tag can receive two LOS signals from Anchors 0 and 1. These two measurement ranges in the LOS environments can obtain two coordinates. Range data from Anchor 2 or 3 can select the accurate coordinate for the tag from Anchor 2 or 3. The positioning result using this method in Area 4 can be observed in Figures 3.18 and 3.29, and the accuracy was indeed improved compared to using raw data with OLS. Especially as shown in Figure 3.19, the accuracy and precision of the tag's position in Area 4 are all the better. This result was predictable because the correct range information calculated the tag's position, so the position result should be as good as in Area 1. Only using range

information from LOS anchors can improve the position accuracy if the system has more than one LOS anchor.

The geometric position of the anchors is another factor affecting the position accuracy of UWB IPS [128]. In Experiments 1 and 2, the tag, Anchors 0 and 2, were almost in a line when the tag was moving along the reference path in Area 2. According to the literature [129], these bad anchor placement positions will significantly reduce the position accuracy of the tag. Therefore, the tag in Area 2 can communicate with three LOS anchors, but the position accuracy is still not satisfying.

In summary, even though the methodology used in this chapter can improve the position accuracy and precision of UWB IPSs, it is impossible to settle all issues for indoor position systems that only rely on one method or sensor. Future research will consider multisensor fusion to enhance position accuracy and system robustness. In the differential drive kinematics model, a two-wheel odometer can offer the distance and yaw of the system. A further plan is to combine UWB and an odometer so that this system can operate well in harsh indoor environments.

3.2.5 Conclusion

This section proposed a novel, simple method to identify and mitigate NLOS for UWB IPSs. The strategy to correct the NLOS error is first to identify the NLOS delay by the sliding window, then update the measured range containing the NLOS error by the delay model, using the WLS algorithm to calculate the tag's position. The experiment results for the accuracy of NLOS identification is approximately 90% in a harsh environment and mostly over 90% in a standard indoor environment. The performance of the NLOS delay model was impressive. According to the data in Tables 3.10, 3.11, and 3.12, the accuracy of tag location in NLOS, which was corrected by the 3D delay model, has been improved to a

certain extent. Although the delay model revised the measured range and improved position accuracy, the location precision is still low. As the green lines in Figures 3.18 and 3.19 indicate, the large jitter margin of the position result remains problematic. The solution is to use WLS algorithms to give different weights according to the UWB signal propagation incidence angle through the wall. The test results showed that the delay model with the WLS algorithm could improve the accuracy and precision of UWB IPSs close to the LOS level.

3.3 Mobile-UWB-Anchor-Configuration Approach

3.3.1 Introduction

With the development of IoT technology, supply chain changes, and intelligent cities, people's activities are increasingly concentrated indoors. Traditional positioning technology in the outdoor environment, such as GPS, can no longer meet the positioning requirements in a complex indoor environment. In addition, the actual requirements of the intelligent warehouse, logistics monitoring, and human capital monitoring also make the research of indoor positioning technology an important and current area.

There are many research directions and methods of indoor positioning technology, such as Bluetooth positioning technology, Wi-Fi positioning technology, and UWB positioning technology, all of which have advantages and disadvantages. Kong et al. summarised that a navigation system needs to consider quality attributes, which include accuracy, availability, reliability, robustness, safety, security, and response time. On the other hand, development constraints also need to be considered, which include maintainability, usability, development complexity, cost constraints, time constraints, and client and supplier collaboration capacity [130]. One of the difficulties in developing indoor positioning technology is measuring the positioning accuracy and system costs.

The deployment cost is low for some positioning technologies, such as Bluetooth and Wi-Fi. Positioning accuracy is also relatively low and can only reach 2 meters. Although high-accuracy technology, such as UWB, can meet the centimetre-level positioning accuracy, the hardware cost is remarkably high, making it unsuitable for large-scale applications.

This chapter focuses on the following research question: How can a more reasonable hardware configuration reduce the system cost without affecting the accuracy of UWB indoor positioning? This research presents a new indoor positioning approach to change the fixed anchor point in a conventional UWB positioning system into a mobile anchor-point configuration to reduce the number of anchor points required in a large-area indoor environment, thereby reducing system cost. This approach is verified using the design and experiments at the positioning accuracy level of the mobile anchor point system.

3.3.2 Mobile-UWB-Anchor-Network Configuration Approach

In the conventional UWB positioning approach, many fixed position anchors are deployed. Figure 3.20 illustrates this positioning approach.

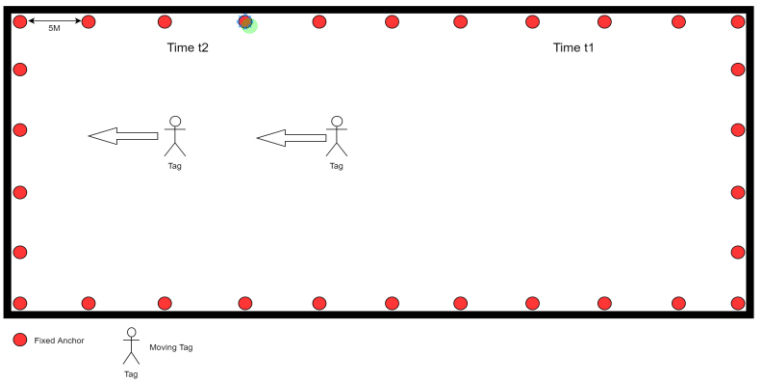

Figure 3.20 Conventional UWB anchor network using fixed anchors

If tags are moving from Time t1 to Time t2 and leave the space where these tags were in Time t1 without tags, the anchors in the Time t1 area are not used for

positioning. We propose a new approach to reduce the deployment of such a large number of fixed anchors, as shown in Figure 3.21.

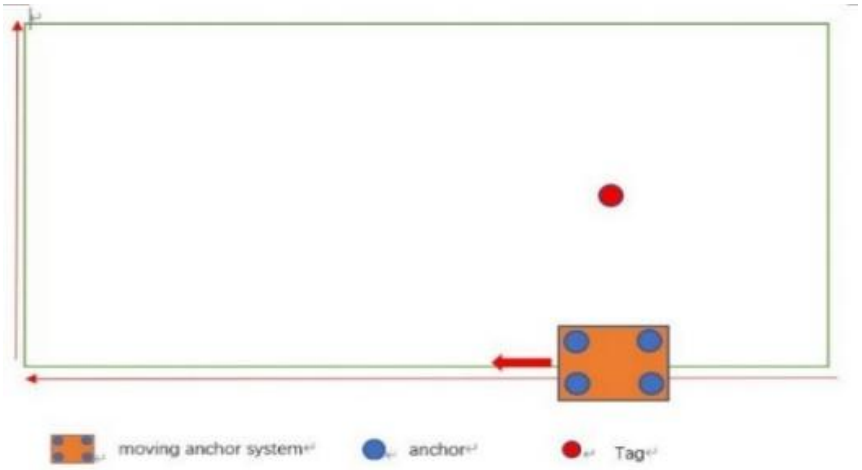

Figure 3.21 Mobile-anchor-network approach

This section discusses a novel approach to transform the previously stationary anchor into a mobile platform, establishing a mobile anchor point system. This system continuously moves along a predetermined track within a specific area. Upon detecting tags in the vicinity, the mobile platform uses displacement time, velocity, and direction to determine its position accurately. By ensuring communication with at least three anchor points, we can employ the TOA method to calculate the tag's precise location, thus effectively positioning our mobile anchor system. The experimental flowchart is presented in Figure 3.22.

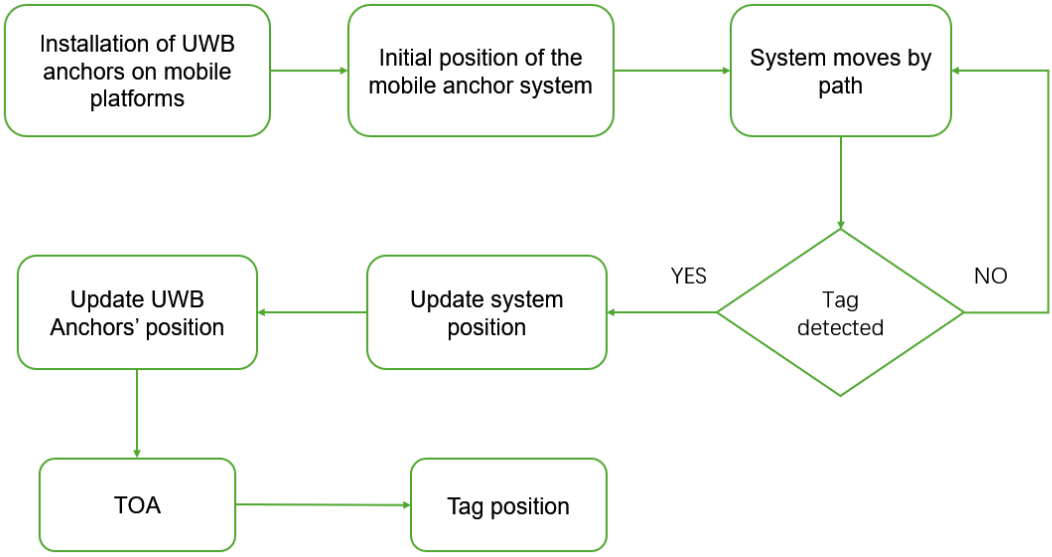

Figure 3.22 Mobile anchor system experimental flowchart

For the positioning algorithm TOA, the actual experimental state signal will be interfered with by noise, which will cause the measurement distance error. So, the ranging error ε_i is added to the experimental simulation. The true distance is shown in Equation 3.31 below:

$$d_i = r_i - \varepsilon_i \tag{3.31}$$

where i is the number of anchors (i = 1，2，3，4), d_i is an actual range between anchor i and tag, r_i is measuring range between anchor i and tag, and ε_i is ranging error.

Assuming:

$$K_i = x_i^2 + y_i^2 + z_i^2 \tag{3.32}$$

where ($x_i\ y_i\ z_i$) is the coordinate of anchor i (i = 1, 2, 3, 4).

In the TOA algorithm, the relationship between the position of the tag, fixed anchor points, and range can be expressed by Equation 3.33:

$$\begin{aligned} d_1^2 &= (x - x_1)^2 + (y - y_1)^2 + (z - z_1)^2 \\ d_2^2 &= (x - x_2)^2 + (y - y_2)^2 + (z - z_2)^2 \\ d_3^2 &= (x - x_3)^2 + (y - y_3)^2 + (z - z_3)^2 \\ d_4^2 &= (x - x_4)^2 + (y - y_4)^2 + (z - z_4)^2 \end{aligned} \tag{3.33}$$

where the coordinates of the tag is $T = (x, y, z)$, anchors coordinates are $A_i = (x_i, y_i, z_i)$ i=1,2,3...N, and d_i is the distance between Anchor i and tag.

Assuming:

$$D = \begin{bmatrix} (x_1 - x_2) & (y_1 - y_2) & (z_1 - z_2) \\ (x_1 - x_3) & (y_1 - y_3) & (z_1 - z_3) \\ (x_1 - x_4) & (y_1 - y_4) & (z_1 - z_4) \end{bmatrix} \tag{3.34}$$

$$X = \begin{bmatrix} x \\ y \\ z \end{bmatrix} \tag{3.35}$$

$$c = \begin{bmatrix} r_2^2 - r_1^2 + K_1 - K_2 \\ r_3^2 - r_1^2 + K_1 - K_3 \\ r_4^2 - r_1^2 + K_1 - K_4 \end{bmatrix} \tag{3.36}$$

$$\Delta = \begin{bmatrix} \varepsilon_2^2 + 2r_1\varepsilon_1 - 2r_2\varepsilon_2 - \varepsilon_1^2 \\ \varepsilon_3^2 + 2r_1\varepsilon_1 - 2r_3\varepsilon_3 - \varepsilon_1^2 \\ \varepsilon_4^2 + 2r_1\varepsilon_1 - 2r_4\varepsilon_4 - \varepsilon_1^2 \end{bmatrix} \tag{3.37}$$

The tag coordinate is shown in Equation 3.38 from the LS.

$$X = \frac{1}{2}(D^T D)^{-1} D^T (c + \Delta) \tag{3.38}$$

3.3.3 Experiment

The main purpose of this experiment is to verify whether the moving anchor points can accurately locate the tag after the fixed anchor points are turned into mobile anchor points.

Experiment Hardware

Experiments are set up using DWM1001 UWB, as shown in Figure 3.23.

Figure 3.23 DWM1001-DEV development boards

In the context of an IPS, positioning accuracy and system cost are the factors of utmost importance. To evaluate these aspects, we conducted tests utilising the DWM1001 board by deploying four fixed anchors and a mobile tag to compare collected data against actual positions. Our findings confirm that the UWB system achieves centimetre-level precision within its effective communication range. However, one major challenge associated with employing UWB for indoor positioning is its high-cost implications. Given that UWB's effective communication range is typically around 10m, large-scale indoor environments, such as airports or warehouses, would necessitate installing hundreds or even thousands of fixed anchors, significantly escalating overall system costs. Consequently, our experiments focus on strategies to mitigate expenses while achieving highly accurate positioning in UWB-based IPS.

Experimental Results

The primary objective of this experiment is to optimise the number of anchors by transforming the fixed anchor into a mobile anchor, thereby reducing system costs. Figure 3.24 depicts four UWB anchors affixed to the corners of a single enclosure with a tag securely attached to a robot. Data acquisition from the tag is

facilitated through its connection with a computer. Consequently, the box and robot establish an interconnected mobile UWB positioning system.

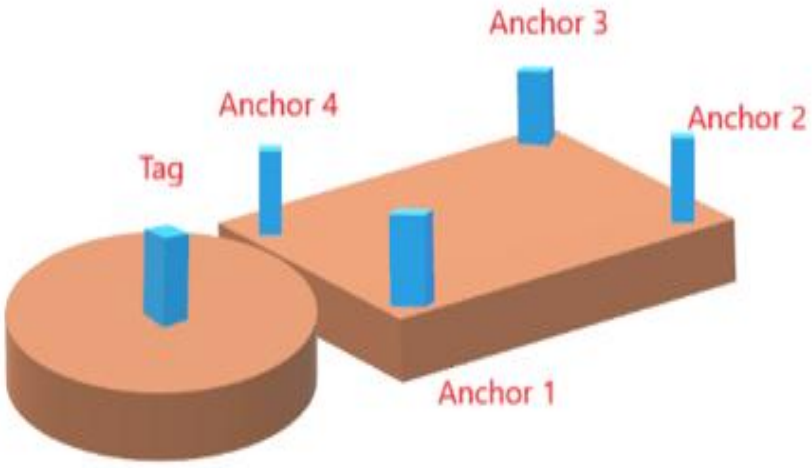

Figure 3.24 Mobile-anchor UWB system

The coordinate information of the anchor is shown in Figure 3.25.

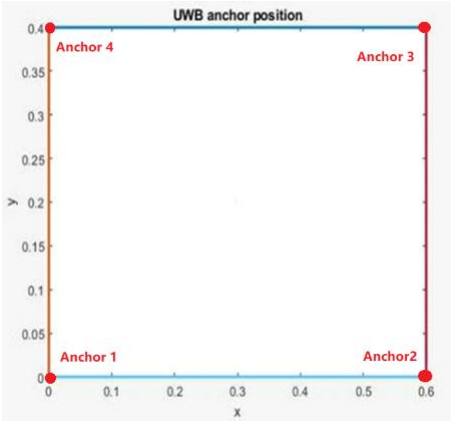

Figure 3.25 Coordinate of anchors

Figure 3.26 Trajectory design

Figure 3.26 illustrates the experimental site and the trajectory of the UWB system. The experiment was conducted in a common area on level 12 of Building 11 at UTS, and the figure depicts the movement path of the entire system from point A to point B and then to point C, where AB represents the X-axis and BC represents the Y-axis. The following figure, Figure 3.27, shows the trajectory of the system.

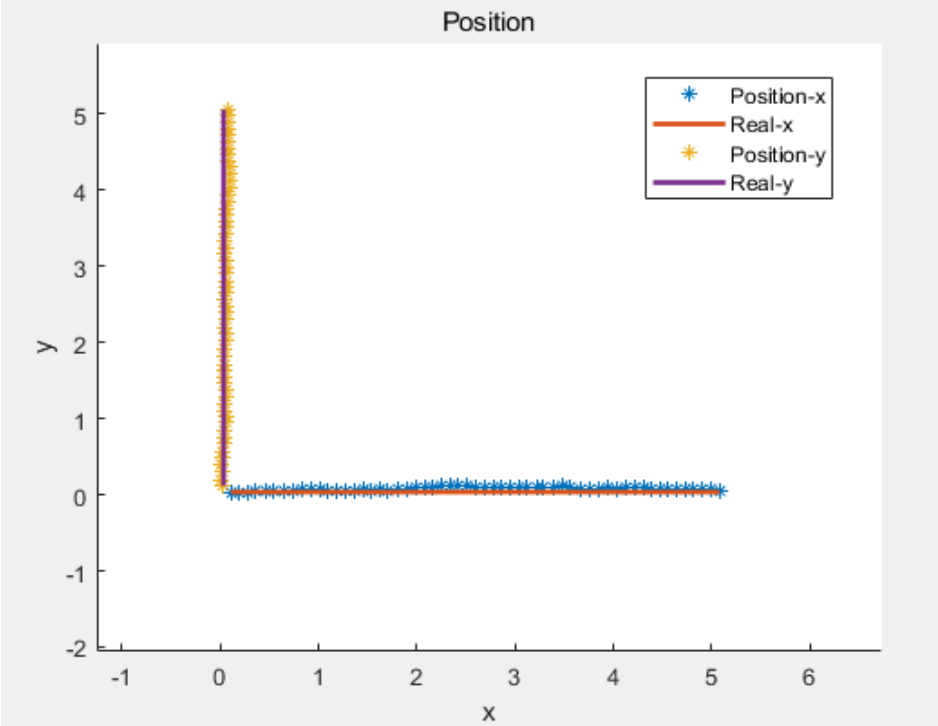

Figure 3.27 Trajectory of the system

The red line in Figure 3.27 depicts the reference path, and the blue and yellow points represent the trajectory of the tag. The mobile UWB anchor positioning system moves along the X-axis and Y-axis for a distance of 5 meters. From the figure above, it is evident that the system can accurately determine the position of the tag during movement. The specific positioning error is illustrated in Figures 3.28 and 3.29.

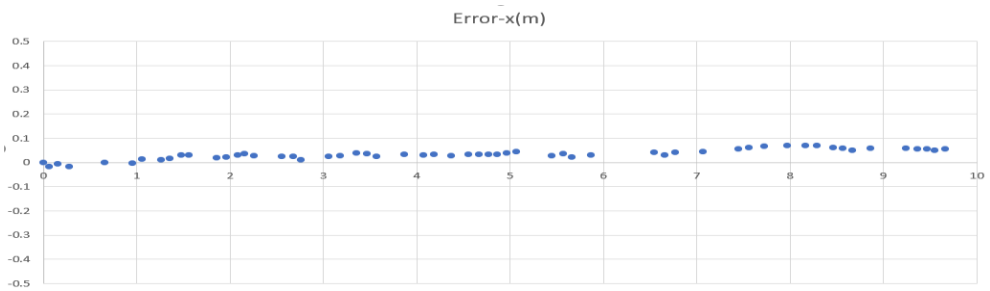

Figure 3.28 Position error during the system moves along the X-axis.

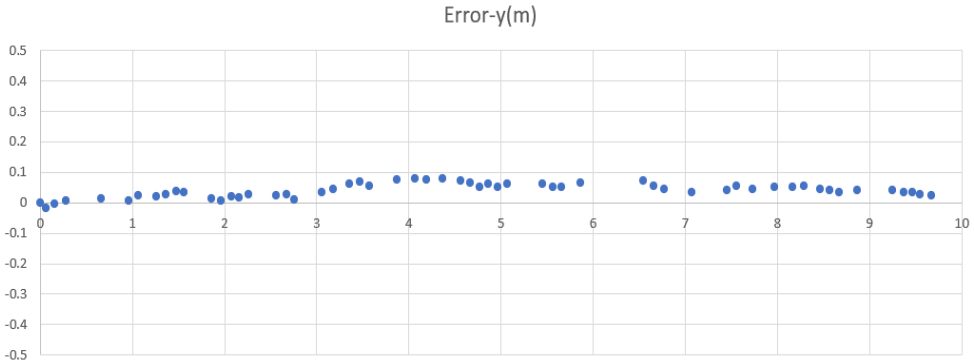

Figure 3.29 Position error during the system moves along the Y-axis.

Table 3.13 Position error

	AVG (m)	**MAX (m)**	**RMSE (m)**
X-Error	0.033193	0.07	0.039183
Y-Error	0.039596	0.08	0.045534

The results of tag positioning during the movement of the mobile UWB anchor positioning system along the X-axis and Y-axis are depicted in Figure 3.28 and Figure 3.29, respectively. Based on these figures and the accompanying Table 3.13, it can be observed that when the system moves along the X-axis, the maximum positioning error of the tag is 7cm with an RMSE of 3.39cm. Similarly, when moving along the Y-axis, the tag's maximum positioning error is measured at 8cm with an RMSE of 4.55cm. Consequently, these findings demonstrate that the mobile UWB anchor positioning system effectively locates tags while operating on a fixed track and further validates the feasibility of transforming fixed UWB anchor points into mobile ones as a cost-saving measure. However, this experiment is only an exploratory experiment to verify the feasibility in a simple experimental environment, and the specific application still needs further research.

4. Chapter 4 A Loosely Coupling Approach for UWB and Wheel Odometry

In the previous chapter, the UWB-only IPS was optimised to a large extent. This chapter introduces a loosely coupled method of UWB and odometry to further improve the positioning accuracy and stability of the system. This chapter is organised as follows. The first section is the study's introduction; the second section is methods, which include the positioning algorithm and the fusion algorithm; the third section is the experimental design and results; the fourth section is the discussion; and the fifth section is the conclusion.

4.1 Introduction

In the previous chapter, it is evident that while UWB positioning accuracy can achieve centimetre-level precision in LOS environments, complex indoor settings pose a significant challenge for UWB-based IPS relying solely on LOS conditions. NLOS errors caused by obstructions can degrade the accuracy of UWB positioning systems to the meter level. Numerous researchers have contributed to addressing this issue in UWB-based IPS.

Cui et al. [114] proposed a method known as Morlet wave transform and convolutional neural networks (MWT-CNN), demonstrating an accuracy exceeding 90% in identifying LOS/NLOS conditions within UWB systems. Accurate identification of LOS/NLOS is crucial for further enhancing positioning accuracy. Zhu et al.'s [131] research described an adapted error map-based particle filter (AEMBPF) method to improve the precision of

localisation in UWB systems. They claimed that this approach could reduce the number of observation points per square meter on the error map by 50% compared to traditional methods, resulting in faster convergence and higher accuracy. However, when applied to more complex or larger map environments, this method encounters computational challenges due to the requirement of constructing an error map. In the experimental investigations conducted by Hao et al. [132], NLOS discrepancies induced by a 0.7-m-thick concrete pillar could exceed 3 m. The study posits the viability of redressal for NLOS errors by developing an error model for diffracted waves, potentially increasing accuracy by up to 80%.

The discernment and amelioration of NLOS errors constitute a central thrust within UWB-based IPS research. In recent years, various scholars have embarked upon various methodologies to grapple with this challenge. Some have advocated residual-based approaches, as elucidated by Jingwang et al. [133], which entail the identification of NLOS instances predicated upon variations in the standard deviation of ranging values, followed by employing Kalman filtering for error rectification. Others have pursued avenues predicated upon scrutinising CIR attributes, as expounded by Chunxue et al. [134], who advocate for selecting higher-fidelity anchor point data through CIR analysis, leading to a discernible 40% abatement in the RMSE associated with positioning. Further inquiries have been directed towards modelling specific obstacles through statistical descriptors, as evidenced by [135-137], which principally concentrate on NLOS errors engendered by human presence. Concurrently, the advent of ML methodologies, including SVM [114, 138, 139] and LSTM [140], has demonstrably catalysed the in-depth scrutiny of CIR and RSS attributes, affording a vantage point for the formulation of error models. Different AI algorithms have their drawbacks; for instance, SVM's drawback is that it requires longer training time and cannot handle noisy data well [141],

and LSTM requires a lot of computation and memory, which is not friendly to the miniaturisation of the carrier.

These methods somewhat mitigate the impact of NLOS errors on positioning accuracy. However, providing consistent and accurate positioning data in complex and changing indoor environments using only one type of sensor is difficult. Consequently, the integration of multiple sensors represents an inexorable progression. Through multi-sensor fusion, the system not only aids UWB technology in identifying and mitigating NLOS errors to enhance positioning precision but also augments the system's resilience in demanding environmental conditions. Commonly integrated sensors with UWB encompass IMU [3, 63], visual [142], odometers [143], and LiDAR [144]. Among these, wheeled odometers have historically received less attention from researchers, primarily due to their constrained applicability, typically limited to 2D vehicular movement in scenarios involving wheeled AGVs. Nonetheless, wheeled odometers are uncomplicated, cost-effective sensors immune to extraneous electromagnetic interference. This makes them suitable for low-cost robotic platforms or those functioning in intricate electromagnetic environments. The advancement of optoelectronic technology has led to notable enhancements in the sampling frequency and precision of wheeled odometers, rendering them highly suitable for integration within a UWB-based fusion positioning system.

The KF is a fundamental algorithm in multi-sensor fusion. Originally developed as a recursive filter for linear systems, the KF's significance remains undiminished despite its long-standing introduction. For instance, in the study by Kim et al. [101], the KF was employed to integrate data from UWB and IMU. The resulting fused system achieved a positioning precision of approximately 0.4 m, even in challenging NLOS conditions.

The evolution of the KF led to the development of the EKF and the UKF, both tailored to address nonlinear system requirements. The EKF achieves this by linearising the nonlinear system through the Jacobian matrix and subsequently applying the KF. However, the EKF's primary limitation arises from its linearisation process, which can introduce inaccuracies. Moreover, the EKF may prove unstable in contexts of intense nonlinearity.

In contrast, the UKF mitigates linearisation issues by employing sigma points for unscented transformation, yielding more accurate state estimates. A comparative study by Krishnaveni et al. [145] examined the EKF and UKF localisation outcomes when fused with UWB and IMU under identical conditions. Their findings underscored the UKF's superior performance over the EKF.

Particle filtering, on the other hand, employs a particle cloud to represent the system's state, updating weights iteratively. While capable of addressing strongly nonlinear systems, its computational demands escalate with an increase in particle count. In a study by Jia et al. [146], particle filtering was used to merge UWB, LiDAR, and odometry data, achieving an RMSE of 5 cm in environments with weak NLOS interference from natural elements like foliage.

Given the demonstrated superiority of the UKF over the EKF and its more manageable computational demands compared to PF, this chapter selects the UKF for further comparative analysis.

Compared to other studies, the algorithm presented in this chapter possesses several advantages. Firstly, within the context of the loosely coupled framework,

our experimental setup has reached the application limits of UWB systems. Many current studies have simpler path designs and NLOS environments in their experimental setups. Some integrated positioning system studies do not consider the impact of NLOS on UWB [71, 147], and others only account for NLOS interference over very short motion paths [148]. In contrast, the UWB system designed in this study encounters NLOS interference over extended durations and distances, making the experimental setting more challenging. The loosely coupled algorithm is relatively straightforward and requires minimal computational resources. Lastly, the system's overall localisation accuracy remains high even under stringent conditions.

The primary contributions of this chapter can be summarised as follows:

- This chapter introduces a straightforward adaptive localisation algorithm that first identifies NLOS through a previous sliding window approach. The ranging values of the optimal localisation anchors are then actively selected for localisation in complex indoor environments to effectively mitigate the effects of NLOS.
- This chapter introduces a novel algorithm loosely integrating UWB and wheeled odometers. This integration facilitates 1D and 2D fusion, adapting to varying motion states. Through comparative analysis with the UKF algorithm, the proposed approach outperforms the UKF algorithm in terms of localisation precision.
- This chapter substantiates the accuracy and effectiveness of the proposed algorithm through comprehensive data collection in a real-world indoor environment.

The chapter is structured as follows: Section 2 describes the localisation principles of UWB and wheeled odometers and the fusion strategy of UWB and wheeled odometers. Section 3 is dedicated to the experimental environment,

equipment, and corresponding results. Section 4 is a discussion of the results. Finally, Section 5 encapsulates the findings and implications of the proposed algorithm.

4.2 Method

4.2.1 UWB

The positioning algorithm of UWB remains unchanged from the LS algorithm introduced in Chapter 3, which calculates the distance between the tag and fixed anchors by measuring the time of flight (TOF) of signals. In ideal conditions, the tag's position can be calculated using at least three distance measurements from fixed anchors. However, due to the complexity of this chapter's experimental environment, it is challenging to establish an accurate mathematical model for NLOS errors, as discussed in Chapter 3. Based on the experimental data presented in Chapter 3, it can be observed that UWB systems exhibit a ranging error below 10cm in LOS environments. Therefore, this chapter proposes a dynamic adjustment method for the positioning algorithm: employing the LS algorithm when at least three LOS ranging measurements are available and utilizing a combined judgment-based positioning algorithm when two LOS measurements are available, as illustrated in Figure 4.1.

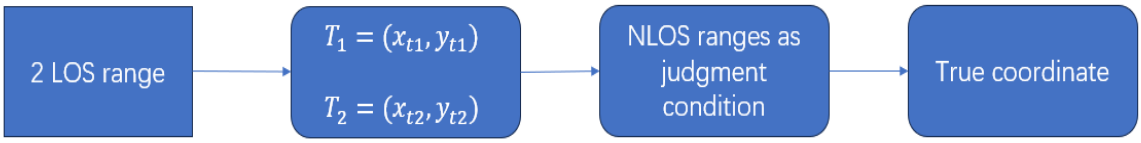

Figure 4.1 Flowchart of the algorithm for the 2 LOS ranging values

In the presence of highly accurate UWB ranging, the distances measured by these two LOS anchor points can be utilised to calculate the coordinates of two points. Although the distance measurements from other anchor points affected by NLOS errors cannot be directly employed for computing the tag coordinates,

they can still serve as a foundation for determining the actual tag coordinates among the two potential coordinate points. Since this chapter adopts a loosely coupled approach that necessitates independent calculation of tag coordinates using UWB and odometry, this UWB positioning strategy already represents an optimal choice and has significant potential to enhance UWB positioning accuracy in NLOS environments.

4.2.2 Odometer

This research employs the two-wheel differential model [149] to identify the robot's locomotion in the context of odometer-based positioning. Within this model, effective control over the robot's motion can be achieved by regulating the speeds of the robot's left and right driving wheels.

In Figure 4.2, vl and vr denote the linear velocities of the left and right driving wheels, respectively. l represents the distance between the two wheels, r represents the turning radius, and θ signifies the turning angle. Based on this model, the ensuing equation can be derived:

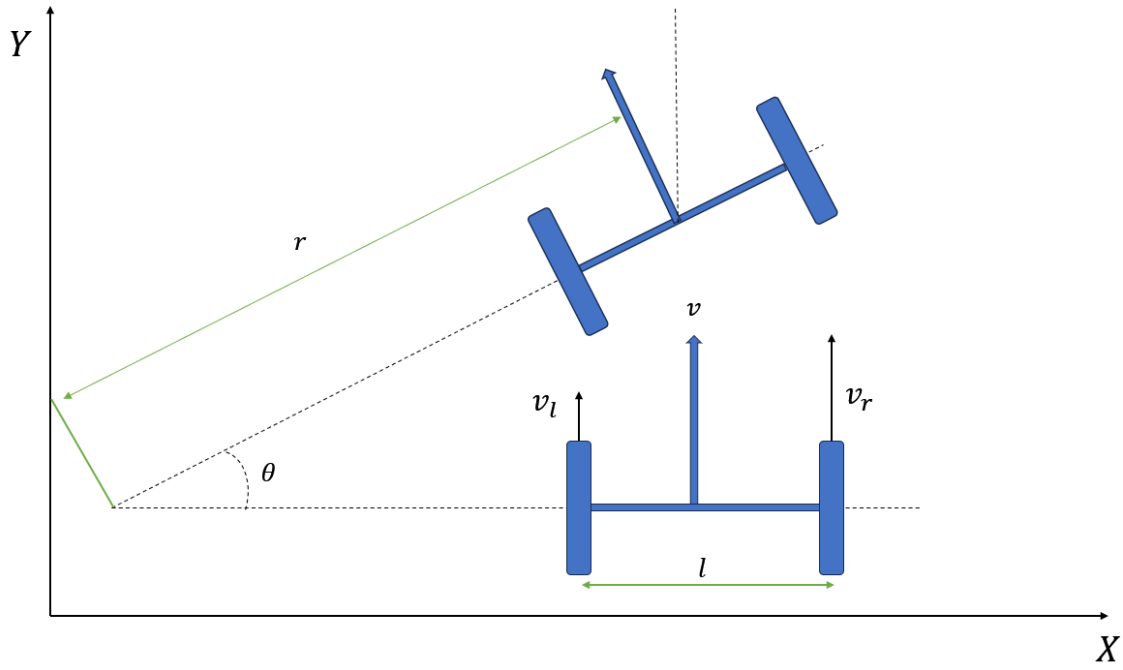

Figure 4.2 Two-wheel differential motion model

Linear velocity v and angular velocity w at the centre of the robot:

$$v = \frac{v_l + v_r}{2} \tag{4.1}$$

$$w = \frac{v_l - v_r}{l} \tag{4.2}$$

Turning radius:

$$r = \frac{v}{w} \tag{4.3}$$

When the sampling frequency is Δt, the odometer data can be converted to the robot coordinates by the differential method (Equations (4.4)–(4.6)):

$$x_n = x_{n-1} + \ v * \cos(\theta_{n-1}) * \Delta t \tag{4.4}$$

$$y_n = y_{n-1} + \ v * \sin(\theta_{n-1}) * \Delta t \tag{4.5}$$

$$\theta_n = \ \theta_{n-1} + w * \Delta t \tag{4.6}$$

Wang et al. [150] categorised wheeled odometer errors into two primary classes. The first category encompasses systematic errors from hardware characteristics such as wheel diameter, wheelbase, and drive motor. These errors accumulate over time and contribute to positioning drift. The second category encompasses random errors, such as wheel slip and uneven terrain. Experimental design measures were taken to minimise these random errors as much as possible.

4.2.3 Fusion Methodology

This section explains an indoor localisation method based on the fusion of odometry and UWB technology, as shown in Figure 4.3.

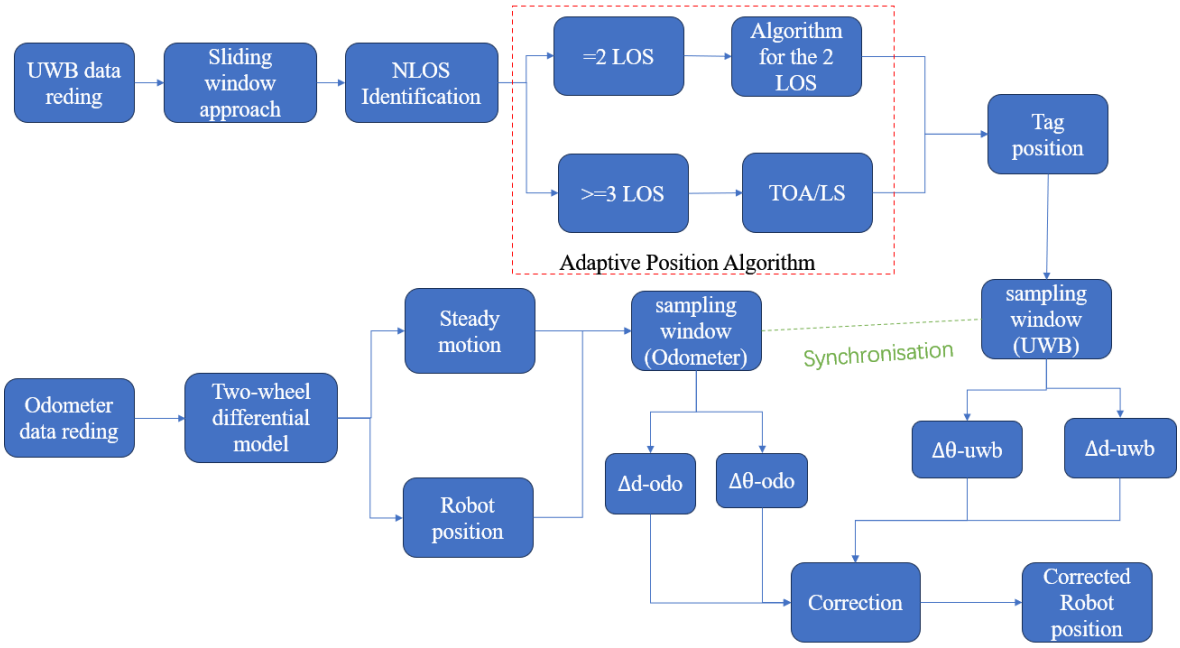

Figure 4.3 Flowchart of the fusion methodology

The UWB system includes four fixed anchors with known coordinates and a tag with no predetermined coordinates. The system employs the TWR technique, eliminating the need for synchronised clocks between the anchors and the tag. This approach effectively reduces the influence of clock-drift error on the range measurements obtained [151].

After measuring the distances between the four anchors and the tag, this section applies the sliding window method, previously introduced in our earlier research, to determine the potential effects of NLOS conditions on the ranging values. Once the range values affected by NLOS are identified, the positioning results of UWB can be optimized using the conditional dynamic positioning algorithm proposed in the previous section.

The fusion system uses a loosely coupled approach. Firstly, a sliding sampling window with a size of 120 is employed to sample the odometry data. Once all the sampled data within the window exhibit linear velocities exceeding the threshold (0.17m/s), it can be inferred that the robot maintains a stable motion state during

this interval. This state implies an absence of unknown obstacles impeding the robot's movement and consequently ensures relatively consistent UWB data readings. Subsequently, by synchronizing with time, we acquire optimized UWB positioning results corresponding to this period and perform linear fitting on the UWB positioning points within this timeframe to determine both the direction and distance of robot displacement. Finally, utilizing both direction and distance information obtained from UWB measurements within the window, we rectify those derived from odometry readings. It should be emphasized that only one set of sampled data is used each time to correct the last odometry data in the window. Such an approach is adopted due to the higher short-term accuracy offered by odometry while avoiding excessive frequency of corrections and ensuring better alignment between our trajectory estimation and actual motion. The proposed fusion technique facilitates the calibration of the robot in both motion direction and distance, thus earning it the designation of the dynamic dimension fusion (DDF) method.

Based on the above characterization of the algorithm, the experimental design needs to expose the inherent problems of UWB and odometer and verify whether the proposed algorithm can effectively fuse the two systems and improve the positioning accuracy. The biggest problem with the odometer is the cumulative error over a long distance, so this part of the experiment will be conducted at a large test site, and the odometer will be run continuously over a long distance to increase the cumulative error. The biggest problem of the UWB system is the NLOS error, so some anchors in the motion path will be designed to be blocked by the wall, causing the NLOS error. At the same time, the algorithm proposed in this part corrects the system localisation in two motion states: uniform steady motion and turning, so the path contains a long straight line and turning. This experimental design can be used to verify whether the algorithm proposed in this section can improve the accuracy of the system localisation.

Algorithm 6 below clearly represents the entire loosely coupled algorithm.

Algorithm 6 Loosely Coupling Approach

Input:

UWB data (range measurements)

Odometer data: left and right wheel velocities (v_L, v_R),wheelbase l

Time step Δt

Output:

Corrected robot position (x_n, y_n, θ_n)

Step 1: Process UWB Data with Sliding Window

Identify LOS and NLOS conditions using a sliding window approach:

$\text{LOS}, \text{NLOS} \leftarrow$ UWB Sliding Window Analysis

Step 2: Adaptive Positioning Based on LOS/NLOS Conditions

if Number of LOS ≥ 3 **then**

Use TOA/LS algorithm to calculate tag position:

Tag Position $\leftarrow$ TOA/LS Algorithm

else if Number of LOS $= 2$ **then**

Use 2 LOS range algorithm to calculate tag position:

Tag Position $\leftarrow$ 2 LOS Algorithm

end if

Step 3: Calculate Linear and Angular Velocities

$v \leftarrow \frac{v_L + v_R}{2}$ *(Linear velocity at robot center)*

$w \leftarrow \frac{v_R - v_L}{l}$ *(Angular velocity at robot center)*

Step 4: Update Position and Orientation

$x_n \leftarrow x_{n-1} + v \cdot \cos(\theta_{n-1}) \cdot \Delta t$

$y_n \leftarrow y_{n-1} + v \cdot \sin(\theta_{n-1}) \cdot \Delta t$

$\theta_n \leftarrow \theta_{n-1} + w \cdot \Delta t$

Step 5: Synchronize and Create Sampling Window

Synchronize UWB and odometer data based on timestamps:

Match timestamps of UWB and odometer data within the time interval T

Create sampling windows based on synchronized data:

$W_{\text{uwb}} \leftarrow \{\text{Synchronized UWB data within } T\}$

$W_{\text{odo}} \leftarrow \{\text{Synchronized odometer data within } T\}$

Compute displacement and orientation change within T:

$\Delta d_{\text{uwb}} \leftarrow \frac{1}{|W_{\text{uwb}}|} \sum_{i \in W_{\text{uwb}}} d_{\text{uwb}}^{(i)}$

$\Delta \theta_{\text{uwb}} \leftarrow \frac{1}{|W_{\text{uwb}}|} \sum_{i \in W_{\text{uwb}}} \theta_{\text{uwb}}^{(i)}$

$\Delta d_{\text{odo}} \leftarrow \frac{1}{|W_{\text{odo}}|} \sum_{j \in W_{\text{odo}}} d_{\text{odo}}^{(j)}$

$\Delta \theta_{\text{odo}} \leftarrow \frac{1}{|W_{\text{odo}}|} \sum_{j \in W_{\text{odo}}} \theta_{\text{odo}}^{(j)}$

Step 6: Correct Robot Position

Perform position correction using sampled data:

Corrected Position $\leftarrow$ Correction Algorithm$(\Delta d, \Delta \theta)$

return Corrected Position 1

4.3 Experiment and Results

4.3.1 Experimental Environments and Equipment

The experiment occurred on the 6th floor of Building 11 at the University of Technology Sydney. The layout of the test area is depicted in Figure 4.4 (a), with the map scaled in meters. The four UWB anchors are marked as yellow squares on the map. The specific coordinates for Anchors 0, 1, 2, and 3 are (8.7, 5.1, 1.87), (8.91, 7.4, 1.87), (24.8, 6.13, 1.87), and (24.8, 8.99, 1.87), respectively. The experimental zone is located on the right side of the map, within a 15-meter-long corridor. The reference path for the robot is indicated by a solid orange line in Figure 4.4(a). The start and end points of the robot's journey are marked with red dots, and the turning point is shown with green dots. In the experiment, the turtlebot2 starts at the initial point, follows the set path to the turning point, and then returns to the endpoint. The UWB tag is attached to the turtlebot2, moving in tandem with it. It is important to note that environmental obstacles, such as walls and cabinets, significantly impact the UWB system, often causing pronounced NLOS errors during its operation.

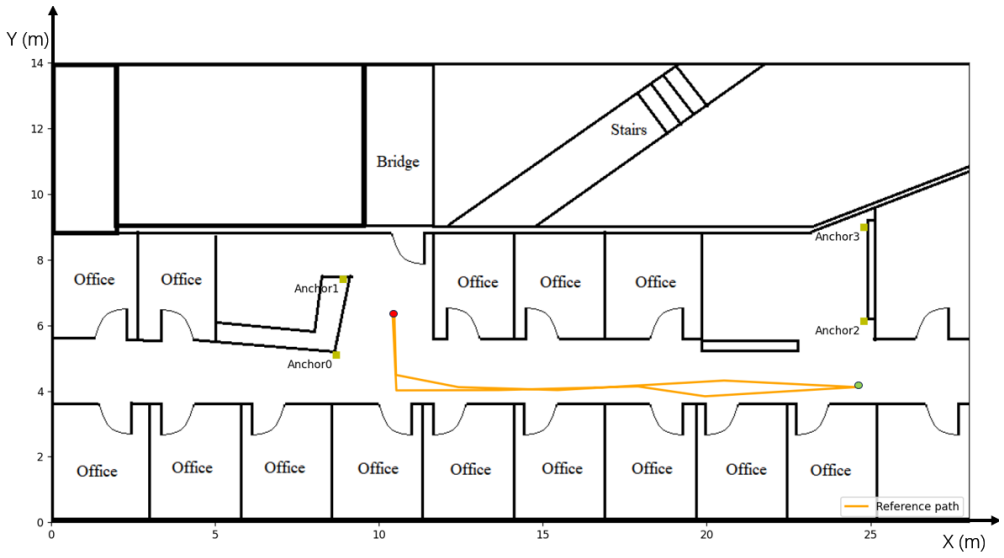

(a)

(b) (c)

Figure 4.4 Experiment design: (a) maps and reference path; (b) UWB; and (c) turtlebot2

In the experiments illustrated in Figure 4.4 (b), the UWB anchors and tags utilise the DW1000 chips manufactured by DECAWAVE. This chip stands out due to its small size, accurate distance measurement capabilities, and cost efficiency [3]. It has become popular in both industrial and research settings, as referenced in sources [152-154]. Under LOS conditions, the UWB system demonstrates a range error of less than 10 cm, operating at a sampling frequency of 3 Hz.

The odometer used in the experiment is a wheel-type odometer from the turtlebot2 platform, shown in Figure 4.4 (c), and it functions at a sampling frequency of 20 Hz. The experimental area features a flat, carpeted surface with a high friction coefficient, effectively reducing the impact of wheel slippage and uneven terrain on the odometer's performance. While occasional slippage may affect the odometer's accuracy, the UWB system remains unaffected. The absolute position data provided by the UWB can still be utilised to correct the odometer, thereby ensuring the accuracy of the overall system.

4.3.2 Experimental Results

This section analyses the experiment's outcomes, covering three main aspects. The first aspect involves comparing and evaluating the positioning results

obtained from the UWB system before and after its optimization. The second aspect examines the use of two distinct algorithms, DDF and UKF, to fuse the optimized UWB results with the positioning data from the odometer. Lastly, the section validates the positioning results derived from the improved algorithms. The positioning accuracy attained through these fusion methods will be thoroughly compared and detailed in presenting the findings.

Figure 4.5 illustrates trajectories, represented in red, which were calculated using uncorrected UWB ranging values that include all NLOS errors and related noise. These trajectories clearly highlight the substantial negative impact of NLOS errors on the UWB system's positioning accuracy. Particularly noticeable on the left and right sides of the trajectory, the UWB signals are obstructed and cannot penetrate through multi-layer walls, resulting in significant NLOS errors due to multipath effects. The maximum positioning error observed exceeds 6.64 meters, with a RMSE of 0.845 meters. Such high levels of inaccuracy demonstrate that these results are unsuitable for IPS.

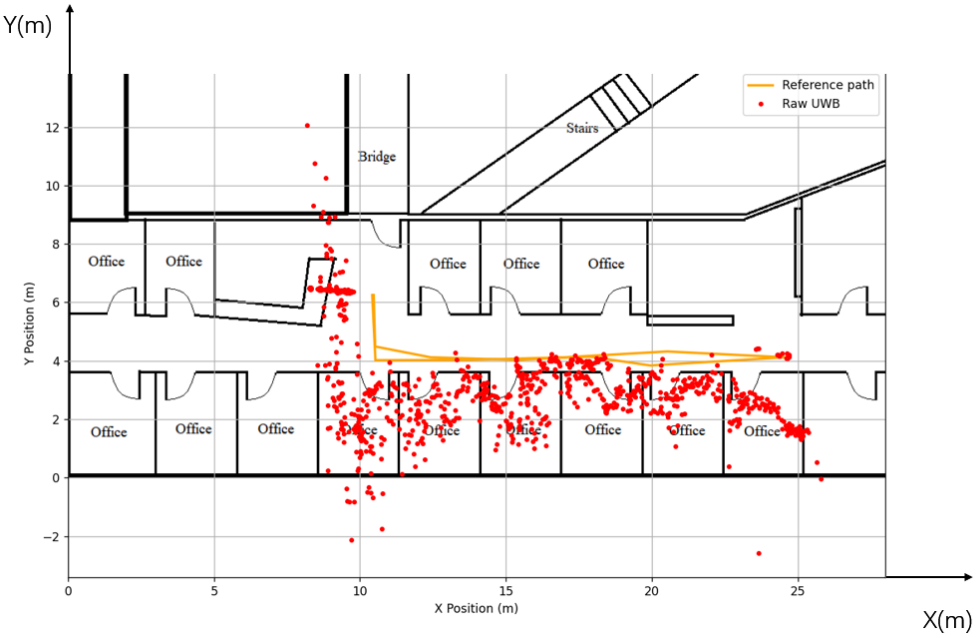

Figure 4.5 UWB positioning results under the influence of NLOS

The implementation of the adaptive positioning algorithm, as shown by the green trajectories in Figure 4.6, leads to significant improvements in accuracy despite some positioning points still showing notable deviations. This inconsistency is likely due to the inherent challenges in achieving absolute accuracy in identifying NLOS conditions. In the trajectory, it is observed that the tag maintains communication with three LOS anchors near the left and right turning points, ensuring positioning accuracy that aligns with the reference path. However, when the tag moves through the central corridor, it can only connect with two LOS anchors. The extended length of the corridor contributes to a certain level of multipath effect, which results in fluctuations in the calculated positioning points. The optimized UWB positioning system achieves a maximum positioning error of 2.968 meters, with mean and RMSE values of 0.127 meters and 0.16 meters, respectively.

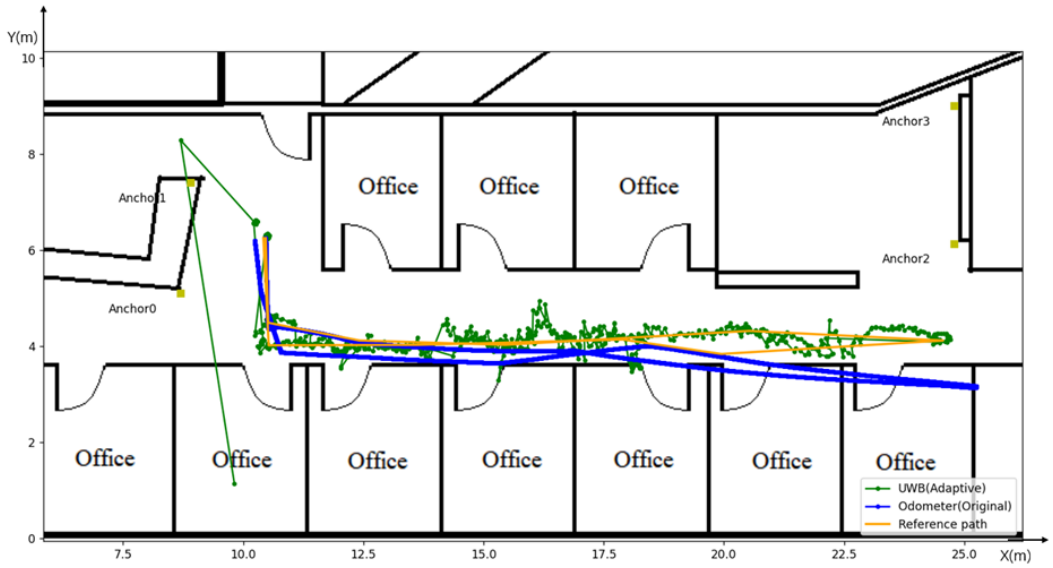

Figure 4.6 UWB positioning results after the adaptive position algorithm

The blue trajectory in Figure 4.6 is derived from the raw data collected from the odometer. Comparing and analysing this trajectory with the reference path shows that the accuracy of the odometer in the initial phase is highly satisfactory. However, as the duration of operation extends, there is a noticeable gradual accumulation of errors, which leads to a progressive divergence in the direction

of motion. This deviation is most pronounced at the rightmost inflexion point of the trajectory. Furthermore, the distance measured by the odometer at this point exceeds the actual distance travelled. This discrepancy is attributed to the accumulation of systematic errors in the odometer's measurements.

The position data from these two sensors are fused using the proposed DDF method and the traditional UKF, with the following results. Figure 4.7 compares the localisation results of the UKF approach (a), represented by a magenta line and the DDF method (b), shown as a black line.

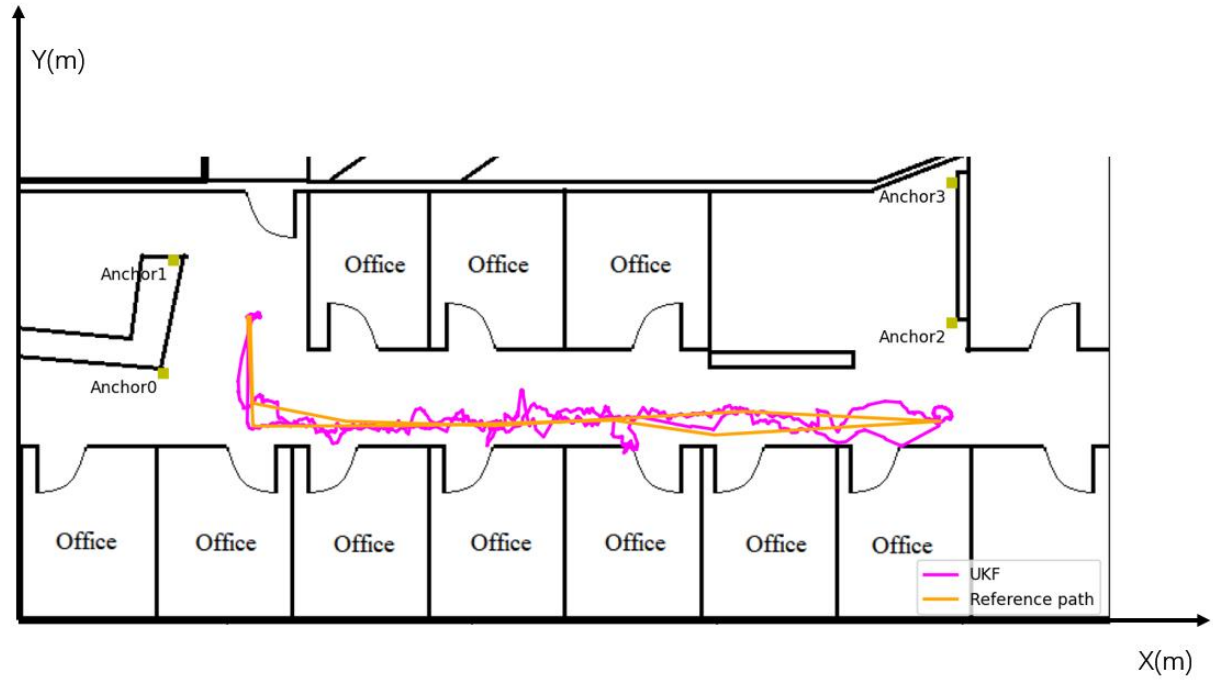

(a)

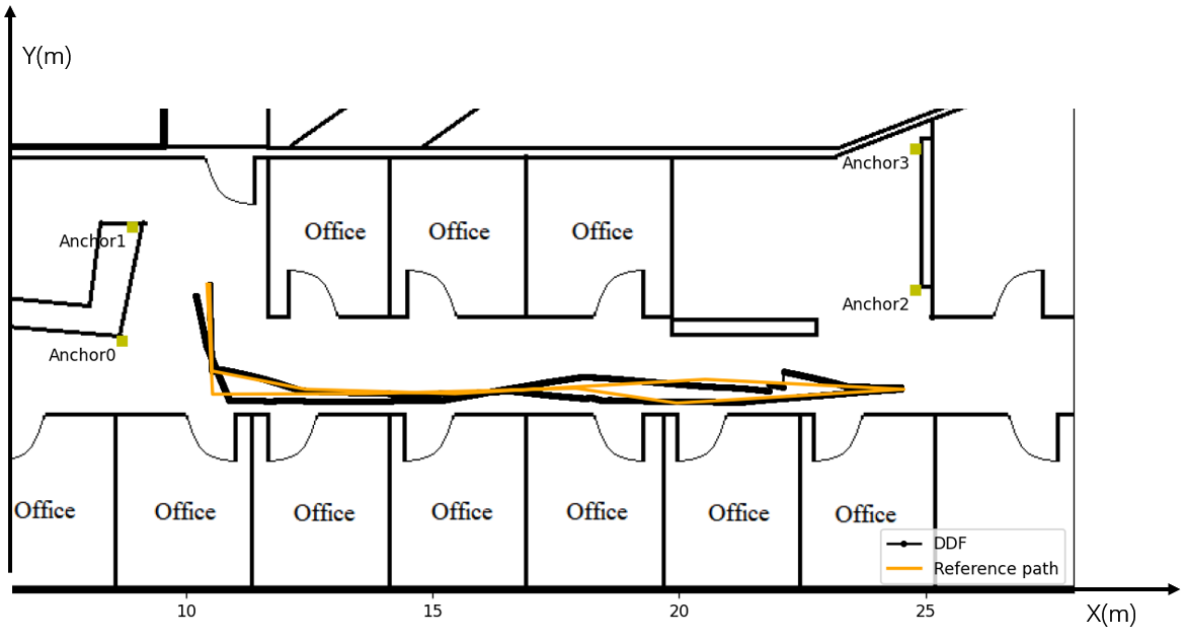

(b)

Figure 4.7 Position results of UKF (a) and DDF (b)

Table 4.1 Position errors

Position Error	**UWB (Original)**	**UWB (Adaptive)**	**Odometer (Original)**	**UKF**	**DDF**
Max (m)	6.639	2.968	1.191	0.677	0.238
Mean (m)	1.448	0.127	0.259	0.119	0.073
RMSE (m)	0.845	0.160	0.304	0.117	0.068

The trajectories are illustrated in Figure 4.7, and the data is tabulated in Table 4.1. The UKF method significantly improves positioning accuracy, reducing the maximum positioning error to just 0.677 meters. Moreover, the mean error and the RMSE are substantially reduced to approximately 12 centimetres. This improvement signifies a notable enhancement in accuracy compared to the initial input from the odometer and the results from the optimized UWB system. The DDF yields a trajectory that closely aligns with the reference path. The data in Table 1 corroborate the efficacy of this approach, showcasing that the maximal error post-DDF fusion is reduced to 0.238 m. Both the mean error and RMSE

have been reduced to around 7 cm. Consequently, the proposed DDF method surpasses UKF in terms of positioning accuracy.

4.4 Discussion

Table 4.2 summarises the comparison of the positioning accuracy of different sensors and UWB fusion, from which it can be seen that the best positioning accuracy is obtained from the literature [155]. However, the experimental environment is in the ideal LOS environment. The literature [155] shows that in the LOS environment, only using UWB can achieve high positioning accuracy with an RMSE equal to 4.66 cm. However, once the UWB has NLOS errors, even in a weak NLOS environment, the overall positioning accuracy of the fused system will be seriously affected, such as in the literature [142], where the RMSE exceeds 20 cm. The result of [146] achieves an RMSE of 5 cm in a weak NLOS environment but uses three more sensors, including the expensive LiDAR.

Therefore, in comparison with these papers, our proposed method uses only two sensors, UWB and odometer, and achieves an accuracy of NLOS equal to 0.068 m in a harsh NLOS environment, which is an excellent performance.

Table 4.2 Comparison with other methods

Reference	Fusion Algorithm	Sensors	LOS/NLOS	Accuracy(cm)
[101]	KF	UWB and IMU	Hard NLOS	RMSE = 30–40
[72]	EKF	UWB, IMU, odometer	LOS	Fusion-RMSE = 3.29 UWB-only RMSE = 4.66
[145]	EKF UKF	UWB and IMU	LOS	MSE-EKF = 143 MSE-UKF= 94
[146]	PF	UWB, LiDAR, odometer	Weak NLOS	RMSE = 5

[142]	Federated KF	UWB, Visual	Weak NLOS	Mean error of fusion: <30
[155]	EKF	UWB, IMU, mmWave radar	LOS	RMSE-UWB-IMU: 18.4 RMSE-UWB-mmWave: 32.3
This chapter	DDF	UWB , odometer	Hard NLOS	RMSE = 6.8

In the initial experimental findings, as depicted in Figure 4.5, it becomes evident that the precision of the UWB system's positioning capability experiences a substantial decline when subjected to NLOS errors. This renders the system incapable of furnishing accurate positional information. While many approaches have been postulated to alleviate these NLOS errors, our experiments indicate that the most favourable positioning accuracy is achieved when ranges containing NLOS errors are straightforwardly omitted. This optimization arises from imperfections in the algorithms designed to detect and mitigate NLOS errors exclusively within the UWB system.

Recognizing the limitations of the approach presented in this chapter is crucial. First and foremost, the effectiveness of this method relies on having at least two LOS ranges. When only a single LOS anchor point is available, the UWB system struggles to calculate tag coordinates independently, making it unsuitable for the strategy described in this document. Additionally, this chapter's methodology primarily focuses on accurately determining the 2D coordinates of the tag. Comprehensive measurements for the tag's 3D coordinates will be a subject of future research. Lastly, due to the constraints of our testing environment, the placement of UWB anchor points was not optimal, affecting the precision of the UWB system's positioning data. Furthermore, this research employs a loosely coupled fusion method that requires both the UWB and odometer systems to provide the location information of the tag. If the UWB system encounters errors

that are difficult to recognise and ameliorate, especially in harsh environmental conditions, or if the odometer experiences slippage and large cumulative errors, the inability of the two subsystems to provide a system position can result in a significant loss of positional accuracy for the fused system. Consequently, Chapter 5 investigates the use of a tightly coupled integration method. The system can function normally with only one LOS range through this tightly coupled method, thereby enhancing its robustness and applicability.

4.5 Conclusion

This chapter introduces a fusion scheme for loosely coupling the UWB positioning system and the odometer, particularly in environments strongly influenced by NLOS conditions. The UWB system's performance is notably compromised in such challenging conditions, and the odometer's accuracy gradually diminishes over prolonged operation due to cumulative errors. This chapter applies an optimised UWB localisation approach to address these challenges, leveraging previously studied NLOS identification techniques based on sliding windows. Furthermore, a novel DDF method was proposed for integrating the optimised UWB localisation data with odometry, employing a loose-coupling fusion strategy. Notably, this method obviates the need for the robot to be actively or passively stationary for odometer calibration, and the calibration process exerts no influence on the robot's motion. This enhancement significantly bolsters system efficiency and renders it more conducive for practical applications. The feasibility and accuracy of this fusion scheme are confirmed by experiments conducted in a real environment. The experimental results manifest an impressive RMSE and average error of around 7 cm for robot positioning. This performance surpasses the positioning accuracy of the odometer and the optimised UWB system and outperforms the fusion accuracy achieved through the UKF.

5. Chapter 5 A Tightly Coupled UWB and Wheel Odometry Based on a Dynamic UKF

The previous chapter introduced a loosely coupled fusion scheme for UWB and odometry, demonstrating good accuracy through experiments. However, due to the limitations of the loosely coupled approach, we observed that when only one anchor point is in LOS with the UWB system, the positioning information provided by UWB becomes highly inaccurate, further compromising the accuracy of the fused positioning. To address this issue comprehensively, this chapter will adopt a tightly coupled approach and construct a fusion IPS using a dynamic UKF algorithm.

5.1 Introduction

As previously discussed, various industries increasingly demand higher accuracy indoor positioning with the advancement of technologies such as smart devices or the IoT. The GNSS, represented by the GPS, faces significant challenges due to signal blockage caused by buildings, rendering it unsuitable for indoor positioning. In recent years, research on IPS has primarily been categorised into two domains: RF-based technologies, such as UWB [156], Wi-Fi [157], and Bluetooth [158-160], and non-RF technologies, such as IMU[161], Camera[162], and LiDAR [163].

RF-based IPS strikes a balance when considering cost and positioning accuracy. While Wi-Fi and Bluetooth offer low costs, these methods often rely on RSS fingerprinting algorithms or path loss models for positioning purposes, resulting in accuracy typically at the meter level [164, 165]. Even with convolutional CNN-

assisted Wi-Fi fingerprinting algorithms, as described in [166], the final localisation error reaches 7.6 m. Some researchers have also adopted other algorithms for accuracy improvement. For example, the literature [167] claims to have achieved decimetre-level positioning accuracy through the RSSI-assisted TDOA method. On the other hand, UWB provides higher accuracy at decimetres or even centimetres at a comparable cost.

RF-based IPS generally offers a wider coverage range since signals can penetrate obstacles or utilise multipath propagation under NLOS conditions indoors, enabling the fulfilment of large-scale localisation requirements as demonstrated by wall-penetrating human tracking using Wi-Fi [168]. However, RF-based IPS may experience significant positioning errors in complex indoor environments due to NLOS effects. The NLOS errors caused by walls are discussed in the literature [169], with experimental data showing that factors that the UWB signal passes through, such as the number of walls and the material of the walls, can lead to several decimetre errors in the UWB range. Even after the mitigation algorithm in this chapter, the NLOS error is still more than ten centimetres.

Due to its wide bandwidth, UWB technology exhibits a high data transmission rate. It commonly employs nanosecond-level pulse signals for communication, ensuring low energy consumption and providing centimetre-level accuracy with high multipath resolution [170]. Consequently, UWB has emerged as a prominent research focus for future endeavours in achieving precise indoor positioning. The prevailing positioning algorithms employed in UWB encompass TOA, TDOA, and AOA. These algorithms primarily measure the signal's TOF to determine the distance between the tag and fixed anchor points [171]. However, it is crucial to acknowledge that even a minute error as small as one nanosecond can result in an amplified ranging error of up to 30 cm due to multiplying TOF by the speed of light [38]. Moreover, obstacles like walls, furniture, or moving individuals in

indoor environments may impede LOS communication within UWB systems, leading to NLOS errors. The NLOS ranging error due to human shading is around 30 cm, and the NLOS error due to concrete walls can be more than 1 m. Ranging values with NLOS errors lead to larger positioning errors when calculating the coordinate points. Therefore, identifying and mitigating NLOS errors represents a significant area of interest within UWB IPS research.

Previous literature has generally categorised the handling of this issue into three categories. The first category involves identifying and mitigating NLOS effects by analysing variations in distance measurements. In reference [113], equality-constrained Taylor series robust LS suppress NLOS residuals, achieving positioning accuracy of around 30 centimetres in complex environments. The second category focuses on CIR, where the main principle is that under LOS conditions, the energy of the first path arrival signal is significantly higher than that of other paths, and this difference decreases under NLOS conditions. AI algorithms have significantly assisted feature extraction and classification for LOS/NLOS scenarios. Reference [172] utilises an SVM to achieve a recognition accuracy rate of 92% for NLOS identification based on hundreds of real training data sets. Similarly, reference [173] demonstrates that CNN algorithms can achieve over 90% accuracy in directly processing CIR data for NLOS identification. Deep learning techniques [51] are also suitable for classifying UWB channel conditions, as they automatically extract features from raw data without requiring manual feature extraction [174, 175]. The final category involves utilising other sensors to identify and mitigate NLOS effects. Previous researchers have conducted extensive studies on integrating IMU [65, 176], camera [142], and LiDAR [64, 144] with UWB technology for IPSs. Those studies have some drawbacks. Either the algorithms are complicated and computationally expensive, or the hardware costs are high. Therefore, this chapter aims to achieve

centimetre-level positioning through a simple, low-cost algorithm for fusing UWB and wheeled odometers.

Wheeled odometers are widely used in indoor AGVs, enabling independent calculation of the robot's coordinates and motion status. It has a low cost and a simple structure, making it easy to maintain. With the development of optoelectronic technology, the accuracy of wheeled odometers has been greatly improved. Based on the advantages of high accuracy in a short time, low cost, and wide application of odometers, this chapter identifies and mitigates UWB NLOS errors by fusion with wheel odometry. The most prevalent fusion algorithms in multi-sensor systems encompass the KF [177], the EKF [108, 178], the UKF [145, 179], and the PF [127]. KF is a fundamental fusion technique typically suitable for linear systems but exhibits subpar performance in nonlinear systems. Extended algorithms such as EKF and UKF have been proposed to address nonlinear systems. EKF approximates nonlinear systems using Taylor series expansion, which introduces errors due to linearisation. UKF approximates nonlinear systems through UT by sigma points. When dealing with highly nonlinear problems, UKF outperforms EKF. PF has a broader range of applications as it simulates the probability distribution of a system utilising a set of random particles and can handle both linear and nonlinear systems. However, given that the system's complexity increases along with the number of particles involved, PF necessitates significant computational resources and may be limited in its application on small, low-cost devices. Considering all factors, we adopt UKF for fusing UWB and wheel odometry in this chapter.

The traditional NLOS identification methods, especially the algorithms for CIR analysis, are usually complicated and computationally intensive. However, the algorithm proposed in this chapter only needs to analyse the outliers of the ranging values to achieve the identification of NLOS, which is a simple and

reliable algorithm. In the research on mitigating NLOS errors, many previous studies, such as experiments in literature [180, 181], were conducted in a milder NLOS environment. At the same time, the method proposed in this chapter is validated in a more demanding NLOS environment, and better centimetre-level positioning can be obtained. The main contributions of this chapter are as follows:

- Proposes a simple method to identify and mitigate the NLOS effects on UWB ranging values, assisted by odometry data.
- Proposes a DUKF fusion method that dynamically adjusts the UKF based on NLOS, HDOP, and robot motion states to achieve more accurate localisation.
- Compared with previous studies, the experimental environment designed in this chapter is harsher for the fusion system of UWB and the odometer, which is better for verifying the accuracy and robustness of the system.

The organisation of this chapter is as follows. The second section introduces algorithms, encompassing fusion algorithms and tightly coupled frameworks. The third section presents the experimental design and result analysis. The fourth section entails a discussion. Finally, a conclusion of this chapter, along with future research plans.

5.2 Methods

Some studies have used simpler, loosely coupled algorithms for the fusion of UWB and other sensors, but such algorithms require each subsystem to compute the robot's position independently [177]. In a strong NLOS environment, accurate positioning information becomes challenging due to limited LOS distance measurements from the UWB system. The accuracy of IPS based on loose coupling will also be significantly affected by inaccurate UWB positioning. Conversely, tightly coupled integration utilises raw measurement data from both subsystems as inputs and employs fusion algorithms to calculate the system's coordinates and pose. Tightly coupled integration processes data early,

improving complexity and accuracy compared to loose coupling. In complex environments, tight coupling accuracy is better than loose coupling [180]. The tight coupling algorithm adopted in this chapter is shown in Figure 5.1.

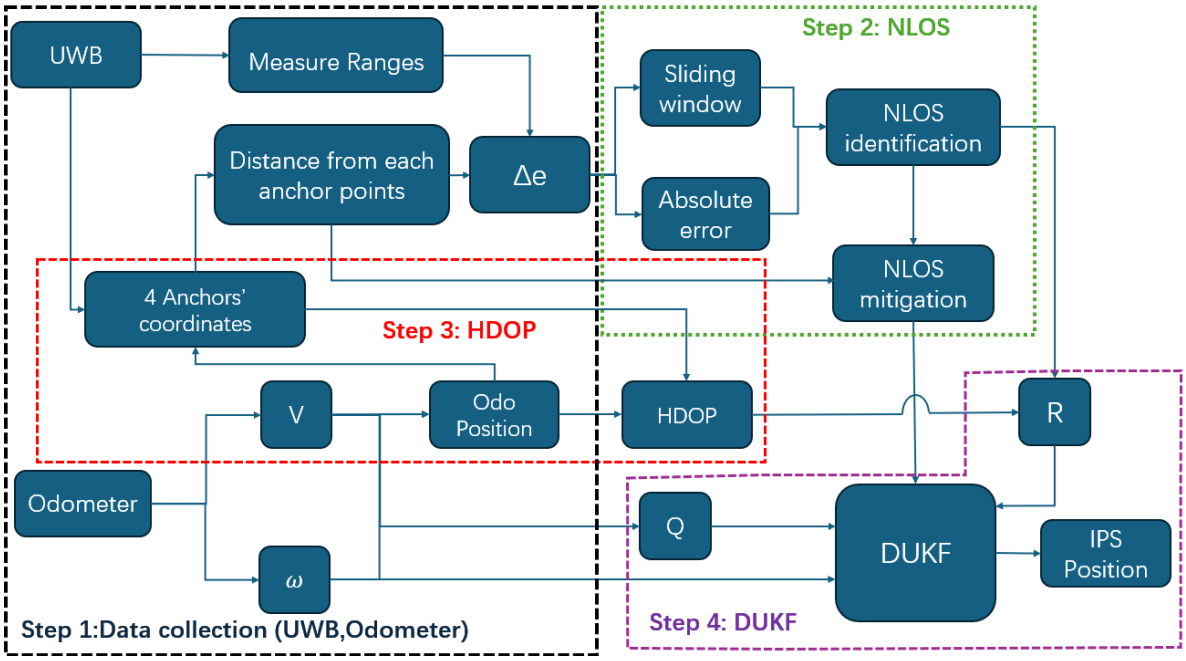

Figure 5.1 Flowchart of the DUKF

The UWB system provides distance measurements from the robot to the four anchor points, and the wheeled odometer calculates information about the robot's motion and position. The odometer position can be used to assist in calculating the HDOP value of the UWB system and the distance to the four UWB anchor points. Specifically, HDOP is a ratio factor that reflects the effect of the geometrical relationship between the position of the anchor point and the tag in the UWB system and its accuracy. The final positioning error is obtained by multiplying the base positioning error with the HDOP value. Ideally, the HDOP value is small, but if the HDOP value is large, the UWB system is not well placed, increasing the error and reducing the accuracy. The distances calculated from the UWB ranging values and the odometer positions can be used to identify and mitigate the NLOS errors of the UWB. Finally, the DUKF algorithm proposed in this chapter can obtain optimised positioning information. The algorithm

illustrated in Figure 5.1 consists of three main parts: NLOS identification and mitigation, computation of HDOP values, and DUKF fusion of all data to output robot coordinates. These three parts are explained separately below.

5.2.1 NLOS Identification and Mitigation

When UWB is affected by NLOS, a positive error in the corresponding distance measurement is introduced. Wheel odometry can provide high-frequency outputs of the robot's speed and direction, which can be used to determine the robot's position. Identification and mitigation of NLOS can be achieved by comparing the distance of the odometer coordinates to the UWB anchor point and the corresponding measured distance of the UWB.

$$abs(\Delta e) = abs(d_{Odometer} - d_{UWB}) \begin{cases} < Threshold1 \rightarrow LOS \\ \geq Threshold1 \rightarrow NLOS \end{cases} \quad (5.1)$$

In Equation 5.1, the difference (Δe) between the distance between the odometry provided position information and the fixed anchor points of UWB ($d_{Odometer}$) and the UWB measured range(d_{UWB}) can be used to identify NLOS. Ideally, Δe should be equal to zero, but cumulative errors in odometry cause Δe changes over time. Nevertheless, ranging errors caused by NLOS can be several tens of centimetres or even meters, Δe can still serve as an effective basis for identifying NLOS.

Relying solely on this method for NLOS identification is not accurate enough; therefore, we apply the sliding window algorithm proposed in previous research [182] to Δe. If sudden changes or outliers occur within Δe, it indicates that the current UWB distance measurement is affected by NLOS. When the window size is k, NLOS can be determined by Equation 5.2.

$$Var(\Delta e_{n-k}, \Delta e_{n-k+1} \dots \Delta e_n) \begin{cases} < Threshold2 \rightarrow LOS \\ \geq Threshold2 \rightarrow NLOS \end{cases} \quad (5.2)$$

If the UWB range value at a particular time is identified as containing NLOS by two judgment conditions, then the range value is judged to have suffered from

the effect of NLOS error. By combining these two criteria for judgment, NLOS can be identified more accurately. The impact of the NLOS error is much larger than the cumulative error of the odometer. Thereby, identified range values from an anchor point containing NLOS errors are replaced directly with distances between odometer positions and this anchor point. This method improves accuracy in updating measurement values using UKF.

5.2.2 HDOP

Similar to GPS, the accuracy of UWB systems is influenced by the distribution of anchor points and their geometric relationship with the tag. In this chapter, which focuses on 2D plane positioning using a wheeled robot, HDOP can be utilised to quantify measurement accuracy at specific locations.

If there are n fixed anchors in the UWB system, the anchor point coordinates are $(x_i,\ y_i)i \in (1,2,3 \cdots n-1)$, and the tag coordinates are (x, y), with a distance of di between them. The unit LOS vector (ai, bi) for anchor point i can be obtained from Equation 5.3 below.

$$a_i = \frac{x_i - x}{d_i}, b_i = \frac{y_i - y}{d_i} \tag{5.3}$$

$$H = \begin{bmatrix} a_0 & b_0 \\ a_1 & b_1 \\ \cdots & \cdots \\ a_{n-1} & b_{n-1} \end{bmatrix} \tag{5.4}$$

The unit LOS vectors of all anchors can form the observation matrix H (Equation 5.4), and the covariance matrix Q is represented by Equation 5.5. As HDOP is the horizontal component of the Q matrix, it can be expressed by Equation 5.6.

$$Q = (H^T H)^{-1} \tag{5.5}$$

$$HDOP = \sqrt{Q_{11} + Q_{22}} \tag{5.6}$$

In order to prevent UWB NLOS errors from affecting the accuracy of HDOP, the robot's position calculated by the odometer is used instead of the tag position when calculating HDOP.

5.2.3 UKF

UKF is an extension of KF, mainly used to deal with nonlinear systems. Unlike EKF's method of linearising nonlinear systems, UKF is an approximate nonlinear system based on the UT of sigma points, avoiding complex Jacobian matrix calculations [1] and the errors introduced by linearisation. According to the literature [145], the accuracy of EKF can reach the first order of the Taylor series, while the accuracy of UKF can reach the third order of the Taylor series. Equations 2.13-2.30 in Chapter 2 describe the standard UKF calculation process.

Following the iterative process, UKF can effectively handle systems with strong nonlinear characteristics. The parameters α, κ, β, Q, and R in the given equations play a crucial role in determining the performance of UKF. Among these parameters, α controls the diffusion level of sigma points and is typically assigned a small value such as 1×10^(-3). κ is used to adjust the weight distribution of sigma points and is usually set to 0 in practical experiments. Additionally, a parameter β influences the characteristics of state distribution when calculating the mean weight; for Gaussian distributed states, β is commonly set to 2.

In the fusion IPS of the UWB and odometer, Q and R affect the degree of dependence of the fusion system on the two subsystems. Especially in practical applications, the two subsystems will change due to environmental factors or changes in the robot's state. Setting Q and R to a fixed value will seriously affect the performance of UKF. In this chapter, the Q and R of UKF were dynamically adjusted by considering the NLOS and HDOP values of UWB and the motion state of the robot.

Algorithm 7 below demonstrates the tightly coupled algorithmic process proposed in this chapter.

Algorithm 7 Tightly coupled system based on DUKF

Input:

UWB data: measured ranges $\{d_{\text{UWB}}\}$, anchor coordinates $\{(x_i, y_i)\}$
Odometer data: displacement d_{odo}, linear velocity v, angular velocity ω
NLOS status
UKF parameters: α, κ, β

Output:

Corrected robot position (x, y, θ)

Step 1: Initialize UKF Parameters

Set UKF parameters:

$\alpha, \kappa, \beta \leftarrow$ Predefined values (e.g., $\alpha = 10^{-3}, \kappa = 0, \beta = 2$)

Initialize process noise covariance matrix:

$\mathbf{Q}_{\text{base}} \leftarrow$ Default process noise matrix

Initialize measurement noise covariance matrix:

$\mathbf{R}_{\text{base}} \leftarrow$ Default measurement noise matrix

Step 2: Compute HDOP Based on UWB Anchor Geometry

Compute unit LOS vectors for all anchors:

$a_i \leftarrow \frac{x_i - x}{d_i}$, $b_i \leftarrow \frac{y_i - y}{d_i}$

Form observation matrix:

$$H \leftarrow \begin{bmatrix} a_0 & b_0 \\ a_1 & b_1 \\ \vdots & \vdots \\ a_{n-1} & b_{n-1} \end{bmatrix}$$

Compute covariance matrix:

$Q_{\text{HDOP}} \leftarrow (H^T H)^{-1}$

Compute HDOP value:

$\text{HDOP} \leftarrow \sqrt{Q_{\text{HDOP},11} + Q_{\text{HDOP},22}}$

Step 3: Adjust Q Based on Robot Motion State

Dynamically adjust $\mathbf{Q}$ based on linear velocity v and angular velocity ω:

Higher values of v and ω lead to increased uncertainty in $\mathbf{Q}$

Step 4: Adjust R Based on NLOS and HDOP

if NLOS is detected **then**
  Increase $\mathbf{R}$ to reflect higher measurement uncertainty
end if
if HDOP is high **then**
  Further increase $\mathbf{R}$ to account for reduced UWB accuracy
end if

Step 5: Update UKF State and Covariance

Predict state using UKF:

$\mathbf{x}_{k|k-1} \leftarrow f(\mathbf{x}_{k-1}, \mathbf{u}_k)$
$\mathbf{P}_{k|k-1} \leftarrow \mathbf{F}_k \mathbf{P}_{k-1} \mathbf{F}_k^T + \mathbf{Q}$

Update state using measurement and dynamically adjusted $\mathbf{R}$:

$\mathbf{K}_k \leftarrow \mathbf{P}_{k|k-1} \mathbf{H}_k^T (\mathbf{H}_k \mathbf{P}_{k|k-1} \mathbf{H}_k^T + \mathbf{R})^{-1}$
$\mathbf{x}_k \leftarrow \mathbf{x}_{k|k-1} + \mathbf{K}_k (\mathbf{z}_k - h(\mathbf{x}_{k|k-1}))$
$\mathbf{P}_k \leftarrow (\mathbf{I} - \mathbf{K}_k \mathbf{H}_k) \mathbf{P}_{k|k-1}$

Step 6: Output Corrected Robot Position

Extract position from state vector:

$(x, y, \theta) \leftarrow \mathbf{x}_k$

return (x, y, θ)

5.3 Experimental Design and Results

5.3.1 Experimental Equipment and Environment

Based on the algorithm proposed above, this part will design a harsh experiment to verify the stability and accuracy of the algorithm. The cumulative error of the odometer will gradually increase with time and distance, so the experiment will be conducted in a large site so that the odometer will increase the error level by moving for a long time and over a long distance. The NLOS error is the most important factor affecting the UWB system, and since the algorithm proposed in this chapter adopts a tightly coupled approach, the experiments are designed to include the stringent situation of having only one LOS anchor point. Meanwhile, this part of the experimental path design takes into account the influence of the geometric layout of the UWB anchor points on the positioning accuracy and introduces the parameter HDOP to assist in adjusting the UKF. The following is the specific experimental procedure designed according to the above ideas.

The UWB experiment employs the DW1000 chips (Figure 5.2a) module from Decawave, which utilises the two-way ranging (TWR) method to measure the distance between the tag and anchor. Based on real measurements, it has been determined that this module operates at a sampling frequency of 3 Hz, providing a ranging accuracy within 10 cm under LOS conditions. The wheel odometry relies on turtlebot2's built-in odometer (Figure 5.2b), operating at a sampling frequency of 20 Hz. Systematic and random errors are two primary sources of error in wheel odometry. Systematic errors arising from slight differences in wheel diameter and friction coefficient variations led to accumulated drift during positioning experiments. The random error resulted from wheel slippage and uneven surfaces during movement. The experimental trials were conducted on the sixth floor of UTS Building 11, as shown in Figure 5.2c. The test site featured rough and even carpeting on the ground surface, effectively mitigating random

errors associated with motion for the wheel odometry system. The UWB system is running on a Windows computer, and the odometer is running on Ubuntu on another computer. The two sets of data are time synchronised by the system time to validate the fusion algorithm proposed in this chapter.

(a)

(b)

(c)

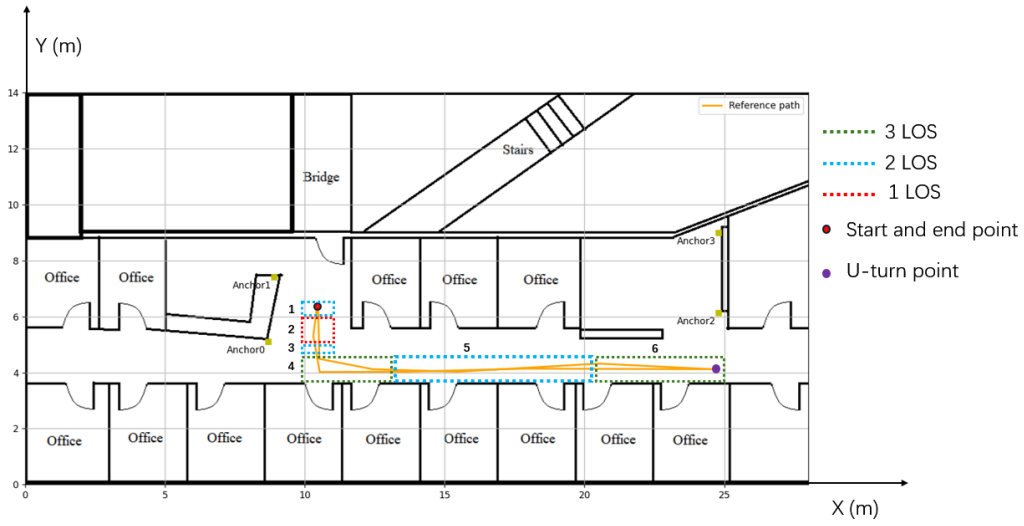

(d)

Figure 5.2 Experiment design: (a) UWB, (b) turtlebot2, (c) experimental site, and d) map and reference path

The experimental map and robot trajectory are depicted in Figure 5.2d. The four yellow boxes in this figure correspond to the positions of UWB anchors (Anchor 0, 1, 2, 3) with coordinates (8.7, 5.1), (8.91, 7.4), (24.8, 6.13), and (24.8, 8.99), respectively, and the height of the anchors are all 1.87m. The orange solid line represents the reference path of the robot's movement, and the red dots indicate its initial and final position. The robot starts from its initial position and moves to a U-turn point represented by a purple dot before returning to its starting point again. A UWB tag is installed on the robot; however, due to obstructions caused by walls during robot motion, some anchor measurements may experience NLOS errors. Within the region outlined by red dashed lines in the figure, the signal from Anchor 1 is obstructed by a cabinet, whereas walls block signals from Anchors 2 and 3. As such, only Anchor 0 remains within the LOS state in this area. Three LOS anchors exist at both corridor ends, indicated by green dashed lines. In the middle corridor enclosed within the blue dashed lines region, Anchors 0 and 2 remain within the LOS state, while walls block signals from Anchors 1 and 3. The UWB system necessitates adaptive switching between environments with one, two, and three LOS anchors in this experimental setup. This environment significantly challenges the accuracy and stability of the proposed DUKF. The different LOS regions are numbered from left to right, as shown in Figure 5.2d. Table 5.1 below clearly shows which anchors are in LOS in different areas.

Table 5.1 LOS anchors in different areas

Area	**1**	**2**	**3**	**4**	**5**	**6**
LOS Anchors	0 and 1	0	0 and 1	0, 1, and 2	0 and 2	0, 2, and 3

5.3.2 Experiment Results

Figure 5.3 below shows the trajectory plot using raw data from UWB and odometry. The red dots represent the coordinates of the tags calculated using the LS method from the raw UWB data containing the NLOS errors. It shows the significant impact of NLOS errors on the UWB system. Due to NLOS errors, the overall trajectory deviates from the reference path. The NLOS also increases measurement noise, resulting in more dispersed localisation points. In this scenario, the accuracy and precision of the UWB system are poor. The maximum error exceeds 6 m, and the RMSE surpasses 80 cm, making it difficult to meet indoor positioning requirements.

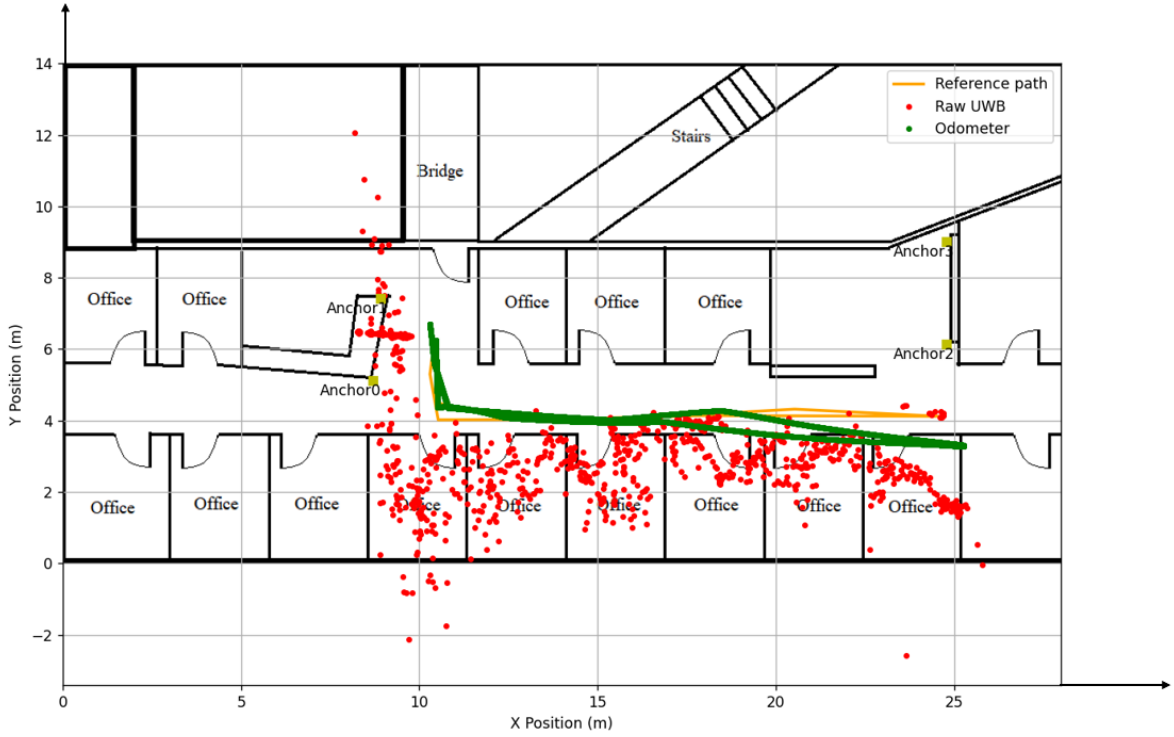

Figure 5.3 UWB and odometer raw trajectories

On the other hand, the green trajectory represents the original path plotted using odometry data. It can be observed that initially, at the early stages of motion, the green trajectory closely aligns with the reference path. However, as the distance travelled and the number of turns increases for odometry measurements, there is a gradual deviation from the reference path. This deviation reaches a maximum

value of 1.093m when it reaches the U-turn point. The average error and RMSE for odometry are slightly over 20 cm. Although odometry also suffers from cumulative errors, it can still serve as an auxiliary means to identify which anchor point's ranging value in the UWB system has encountered NLOS errors, as shown in Figure 5.4.

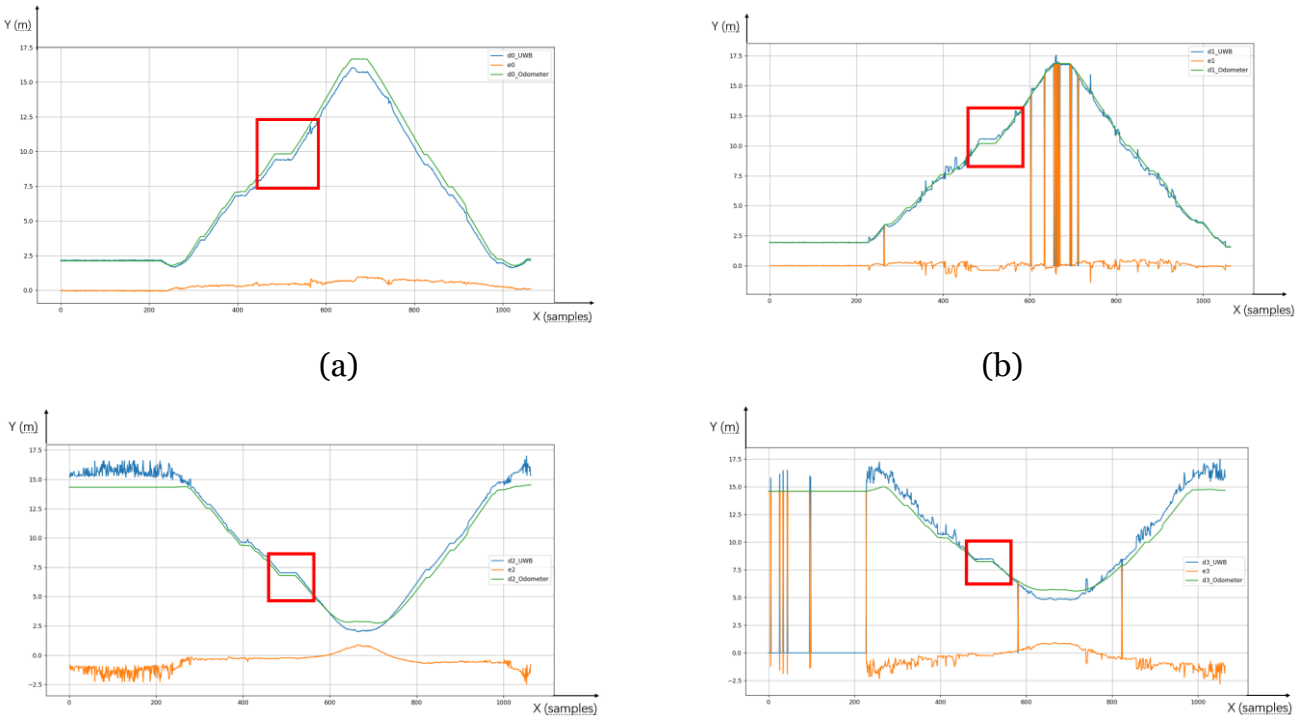

Figure 5.4 UWB ranging values (blue), the distance between the anchor point and odometer (green), the difference between the range and the distance (orange) and the robot is stopped by human interference (red box), (a) Anchor 0, (b) Anchor 1, (c) Anchor 2, (d) Anchor 3

The original ranging values (*dn_UWB*, n=0, 1, 2, 3) of the four UWB anchors are depicted in Figure 5.4 with four blue lines. It can be observed that the ranging value of Anchor 0 remains smooth and mostly unaffected by NLOS conditions. However, the remaining three anchors experience varying degrees of influence from NLOS during robot movement, leading to significant fluctuations in measured distances. Both Anchor 1 and Anchor 3 even lose data when multiple

walls block the signal. The data enclosed within the red box corresponds to situations where sudden pedestrian presence pauses robot movement temporarily. Furthermore, when the robot resumes its motion, NLOS occurs as pedestrians pass through Anchors 0 and 1; this can also be observed from the fluctuating data in Figure 5.4.

The green line in the diagram represents the distance between the anchor point and the robot coordinates provided by the odometer ($dn\_Odometer$, n = 0, 1, 2, 3). The orange line in the figure represents the difference (e_n) between $dn\_Odometer$ and dn_UWB. It can be observed from the graph that when UWB is affected by NLOS, e_n exhibits a significant increase with pronounced fluctuations. By considering the absolute value of e_n and employing the previously studied sliding window method, NLOS can be accurately identified. Under NLOS conditions, e_n is much smaller than NLOS errors. Therefore, this study mitigates NLOS effects by substituting dn_UWB contains NLOS errors with corresponding $dn\_Odometer$ values.

According to the robot's position provided by the odometry, the HDOP value of the UWB system can be calculated. The UWB data after NLOS mitigation is used as observation input for UKF, with a noise covariance matrix R = diag[$r0$, $r1$, $r2$, $r3$]. According to the values of e_n and HDOP dynamically adjusts R in UKF, the corresponding r_n for range measurements with NLOS errors can be calculated by Equation 5.25.

$$r_n = \frac{abs(e_n)}{var} * HDOP \tag{5.25}$$

where var is the threshold in the sliding window identification NLOS algorithm, which changes according to different environments.

The state vector of the UKF system is X = [x,y,θ], where (x,y) represents the coordinates of the robot and θ is the heading angle. For this experiment, different

Q values are set based on the robot's motion state. The robot's coordinates and heading angle remain constant when stationary, so the Q = diag [0, 0, 0]. During straight-line movement, the odometer coordinates are affected by more noise, and the heading angle is not affected as significantly. It is better to increase the values of x and y in Q and keep the values of θ at a small number, so set Q = diag [0.01, 0.01, 0.0001]. On the contrary, if the robot is turning, Q is set to diag [0.0001, 0.0001, 0.01]. Employing this fusion algorithm called DUKF, the fused trajectory of the system is shown in Figure 5.5.

Figure 5.5 Trajectory of DUKF

The magenta line in Figure 5.5 represents the robot trajectory output through the DUKF algorithm, demonstrating its proximity to the reference path. Fusion with DUKF has significantly enhanced positioning accuracy compared to UWB and odometry, as evidenced by specific data in Table 5.2.

Table 5.2 Position error

	UWB-only	**Odometer**	**DUKF**
Max(m)	6.708	1.093	0.342
Mean(m)	1.484	0.221	0.085

RMSE(m)	0.835	0.296	0.075

Figure 5.5 demonstrates the effective mitigation of harsh NLOS interference on the UWB system by the DUKF algorithm, resulting in optimised positioning accuracy and precision. A comparison with the odometer raw trajectory in Figure 5.3 shows a notable reduction in cumulative errors related to total mileage and direction of motion. The data presented in Table 5.2 indicates that under strong NLOS conditions, UWB positioning accuracy has degraded to unacceptable levels. The overall accuracy of the odometers exceeds expectations and can achieve an RMSE of around 0.3 m over long run times.

The DUKF algorithm significantly improved positioning accuracy, with an RMSE of 0.075 m and a mean error of 0.085 m, achieving the UWB system's claim for a 10 cm positioning error under LOS conditions. The result demonstrated that the DUKF algorithm can achieve robust and highly accurate positioning in complex indoor environments.

5.4 Discussion

The data in Table 5.2 also reveals that DUKF still exhibits a maximum positioning error of 30 cm on the left side of the trajectory when the robot makes a right-angle turn to return to the ending point. In this area, there is only one valid LOS anchor point for UWB, and the odometry system also experiences a significant decrease in motion accuracy over long distances. Consequently, both subsystems' observations and predictions contain substantial errors, indicating reduced accuracy in the final segment of the trajectory as the robot moves along the Y-axis during its return journey. The red boxes marked trajectory in Figure 5.5 represent a scenario explained in Figure 5.4 where the sudden appearance of pedestrians caused robot stoppage, and NLOS occurred for Anchors 0 and 1. Only Anchor2 remained in the LOS state for the UWB system during this time. It can be

observed that the position result of DUKF was a brief deviation from the reference path at this moment, but as soon as the pedestrian obstruction disappeared, it gradually approached closer to the reference path again. Based on these two scenarios above, it can be concluded that even when applying the DUKF algorithm, at least one LOS UWB anchor point is necessary to ensure the system's positioning accuracy.

Table 5.3 below summarises recent research on combining UWB with other sensors to form an IPS. The comparison reveals the advantages of the fusion system in this research.

Table 5.3 Comparison with other methods

Reference	Sensors	Hardware Cost	LOS/NLOS	Accuracy(cm)
[183]	Visual, Inertial and UWB	High	Moderate NLOS	RMSE: Over 20
[102]	UWB, IMU	Low	Mild NLOS	RMSE: 7.58
[184]	UWB, IMU	Low	LOS	RMSE: 4
[181]	UWB, IMU, Odometer, LIDAR	High	Mild NLOS	RMSE: 7-9
[185]	LiDAR, UWB	High	LOS	RMSE: 14
[54]	UWB, IMU	Low	Mild NLOS	Mean error: 12
[186]	Visual, UWB	High	LOS	RMSE: 20
This research	UWB, Odometer	Low	Harsh NLOS	RMSE: 7.5

In Table 5.3, it is evident that certain studies have achieved high positioning accuracy in UWB fusion systems, as demonstrated by references [102, 181, 184], all of which have accomplished positioning accuracy within 10 cm. However, these experiments were conducted primarily in LOS or mildly NLOS environments. For example, in literature [181], the NLOS of the UWB system is generated by the occlusion of the sparse plants in the greenhouse, and from the experimental results, it can also be seen that the system can achieve a positioning accuracy of about 15 cm when only using UWB, which also proves that UWB has a relatively mild effect on NLOS. Conversely, alternative sensors such as vision and LiDAR escalate hardware costs and fail to provide higher positioning accuracy comparable to UWB-only IPS. Consequently, some studies indicate decreased positioning accuracy when these sensors are integrated. For instance, references [183, 186] reveal that a UWB system fused with visual sensors achieves an approximate positioning accuracy of 20 cm. The strength of the current study lies in utilising cost-effective sensors to achieve centimetre-level positioning accuracy even under harsh NLOS conditions.

5.5 Conclusion and Future Planning

The present research proposes a tightly coupled architecture-based DUKF algorithm fusion of UWB and wheel odometry to form an IPS. This method offers the advantages of cost-effectiveness, high accuracy, and robustness without analysing UWB's CIR characteristics or establishing error models, making it suitable for diverse indoor environments. The design of this validation experiment is highly rigorous, considering not only the NLOS state of some UWB anchors caused by wall obstructions but also interferences from a sudden human presence on both the odometry and UWB systems. The experimental scenarios meticulously consider real-life environmental factors, including a scenario with only one LOS anchor point. In this intricate and dynamic experimental setting,

the proposed DUKF system achieved an impressive RMSE of only 0.075 m and an average error of 0.085 m, achieving stable robot localisation at centimetre-level accuracy. Future research plans will integrate sensors such as cameras or LiDAR into the system to enable mapping, obstacle recognition, collision avoidance, and path planning while concurrently maintaining precise positioning accuracy at the centimetre level.

6. Chapter 6 Conclusions and Future Work

The advancement of intelligent devices and IoT technology has stimulated the demand for IPSs. Conventional methods like Wi-Fi and Bluetooth exhibit positioning errors ranging from several centimetres to over a meter, limiting their utility to only presence detection and rough positioning purposes. Emerging applications such as AR, VR, and smart warehouses necessitate more precise determination of coordinates and postures for individuals or robots. Researchers are actively working towards enhancing indoor positioning accuracy to the centimetre level, with UWB technology being a promising choice. UWB's ability to transmit extremely short pulses enables more accurate measurement of signal flight time, thereby achieving centimetre-level ranging precision. However, this characteristic also renders UWB highly susceptible to NLOS errors caused by environmental obstructions in complex indoor settings that constantly change. In UWB IPS deployments, obstacles can easily obstruct LOS signals, leading to NLOS errors. Our empirical measurements demonstrate that NLOS ranging errors induced by human bodies fall within several tens of centimetres; materials possessing strong signal shielding capabilities, like concrete walls or iron doors, can cause ranging errors on the scale of meters. Consequently, NLOS errors significantly impact the accuracy and stability of UWB IPS solutions. The primary objective of this thesis is to achieve cost-effective centimetre-level positioning accuracy while accounting for NLOS effects in UWB systems.

6.1 UWB-Only IPS

The primary objective of Chapter 3 is to investigate UWB-only IPS. Section 3.1 proposes a method for identifying and mitigating NLOS. The basic principle of

NLOS identification is the sudden increase in range measurements caused by NLOS errors. This study focuses on AGVs, which typically have a movement speed of less than 1m/s. If there is a significant difference in range measurements between two adjacent time points for a certain UWB anchor, it is considered to be affected by NLOS. Additionally, under NLOS conditions, measurement noise increases. If the variance of range measurement differences noticeably increases in a period, it can also be considered as being influenced by NLOS. The NLOS can accurately be identified using this section's proposed sliding window method. Furthermore, this section introduces a 2D error model specifically for wall-induced NLOS effects. Combining these two algorithms can effectively identify and mitigate the impacts caused by NLOS.

In Section 3.2, a WLS algorithm based on NLOS errors is proposed. This algorithm assigns different weights to distance measurements according to the anchor's state, including LOS/NLOS and the degree of NLOS influence. It effectively utilises distance measurements affected by NLOS errors. Additionally, the error model of walls is improved from 2D to 3D, further enhancing the accuracy of NLOS error correction. Experimental results demonstrate that this method can achieve positioning accuracy similar to LOS under severe NLOS effects caused by walls.

However, utilising the UWB module in our experiments incurs a substantial hardware cost. In scenarios like airports or shopping malls, which encompass large areas, more UWB anchors are required, further escalating the hardware expenses associated with UWB technology. To address this concern, Section 3.3 proposes a transformation of fixed anchors utilised in UWB IPS into mobile anchors. By relocating idle anchors to areas with positioning requirements, we can effectively reduce the number of UWB IPS anchors and associated hardware costs without compromising system accuracy. Experimental results validate that

precise tag positioning can still be achieved even when anchor systems are in motion.

6.2 Multi-Sensor Fusion Method for UWB and Wheeled odometers

Although UWB-only IPS research has partially mitigated the impact of NLOS errors, it falls short in addressing the complexities of real-world scenarios compared to controlled experimental environments. A low-cost and highly accurate multi-sensor fusion approach is proposed to overcome this limitation by integrating UWB and odometry systems. By leveraging their respective strengths, these sensors synergistically enhance the accuracy and robustness of the system.

The fourth chapter presents a loosely coupled framework introducing a fusion algorithm for UWB and odometry. Firstly, the sliding window method proposed earlier is utilised to detect NLOS, followed by dynamic adjustments of the UWB positioning algorithm based on the number of LOS anchor points to optimize the UWB system. While wheel odometry is subject to long-term positioning inaccuracies due to systematic and random errors, the optimized UWB system provides absolute coordinates regardless of operating time. Utilizing stable motion coordinates from UWB makes it possible to rectify deviations in total mileage and direction caused by odometry, smoothing out UWB coordinates fluctuations resulting from measurement noise. Experimental results demonstrate that this algorithm can maintain accurate system positioning even under strong interference affecting UWB.

The fifth chapter presents a tightly coupled approach for integrating UWB and wheel odometry. In contrast to the loosely coupled method discussed in Chapter 4, which relies on both subsystems providing coordinate information, this approach addresses the challenges faced in more complex environments where UWB has only one LOS anchor, making it difficult to ensure accurate positioning

with loose coupling. To solve this problem, a dynamic UKF algorithm that tightly couples UWB with wheel odometry is proposed in this chapter. This algorithm leverages odometry measurements to assist UWB in identifying and correcting NLOS conditions and calculates the HDOP of the UWB system using coordinates obtained from the odometry system. Precise fusion-based localisation can be achieved by dynamically adjusting UKF parameters and measurements based on the NLOS status of UWB, HDOP values, and robot motion states measured by the odometry system. Rigorous experimental scenarios are designed to evaluate the performance of the proposed method under various UWB operation scenarios (1, 2 or 3 LOS anchors) while also considering potential disruptions caused by human presence that impact normal operations of both UWB and wheel odometry systems. Under such demanding and realistic conditions, the proposed system autonomously identifies NLOS conditions and dynamically adjusts UKF parameters to achieve centimetre-level positioning accuracy consistently.

6.3 Future Work and Applications

A fusion positioning system combining UWB and odometry has been gradually developed through the research above, demonstrating universal applicability even in harsh NLOS environments while maintaining accuracy. However, the system lacks mapping, obstacle recognition, and path planning abilities. Future research will primarily incorporate visual sensors to enhance UWB IPS's perception of the surrounding environment. It should be noted that visual sensors still exhibit significant localisation errors compared to UWB systems' centimetre-level precision. Based on the findings of other researchers at this stage, it is challenging for these two sensor types to achieve centimetre-level positioning when fused. Therefore, future research directions will combine vision and UWB technologies to achieve centimetre-level accuracy.

The development of precise indoor positioning technology has a great impact on many industries. In this research, UWB-only indoor positioning systems can be applied to the management of people and goods, such as the management of patients and medical devices in hospitals, the location of people and real-time navigation in shopping malls, the real-time tracking of baggage in airports and the location of goods in smart warehouses, and the localisation of people in emergency rescue. Some major cell phone manufacturers have already added UWB to their phones, and in the future, it is expected that these smart terminals will be able to provide more accurate real-time positioning for people through indoor UWB positioning systems. The fusion of UWB and odometry is aimed at the developing robotics industry. Many robots have already been applied in real life, including daily use of sweeping robots, intelligent forklifts and sorting robots in smart warehouses, and robots in shopping malls and hospitals to deliver goods in buildings.

The centimetre-level positioning accuracy achieved in this research could facilitate innovation and development in these industries. For example, it can help audiences find their seats quickly for theatres and concerts. For smart warehousing and logistics it can improve the efficiency and accuracy of goods in and out of the warehouse and reduce costs, and for robots, accurate positioning can assist in more precise path planning and obstacle avoidance. With future research, the application of accurate indoor localisation will be even more extensive, bringing more value to the industry and consumers.

References

[1] J. Fu, Y. Fu, and D. Xu, "Application of an adaptive UKF in UWB indoor positioning," in *2019 Chinese Automation Congress (CAC)*, 2019: IEEE, pp. 544-549.

[2] C. A. Patterson, R. R. Muntz, and C. M. Pancake, "Challenges in location-aware computing," *IEEE Pervasive Computing,* vol. 2, no. 2, pp. 80-89, 2003.

[3] R. Ali, R. Liu, A. Nayyar, B. Qureshi, and Z. Cao, "Tightly coupling fusion of UWB ranging and IMU pedestrian dead reckoning for indoor localization," *IEEE Access,* vol. 9, pp. 164206-164222, 2021.

[4] L. Yu, Y. Liu, T. Chi, and L. Peng, "An iBeacon-based indoor and outdoor positioning system for the fire emergency command," in *2017 Forum on Cooperative Positioning and Service (CPGPS)*, 2017: IEEE, pp. 326-329.

[5] M. Zare, R. Battulwar, J. Seamons, and J. Sattarvand, "Applications of Wireless Indoor Positioning Systems and Technologies in Underground Mining: A Review," *Mining, Metallurgy & Exploration,* pp. 1-16, 2021.

[6] F. Abulude, A. Akinnusotu, and A. Adeyemi, "Global Positioning System And It's Wide Applications," *Continental J. Information Technology,* vol. 9, no. 1, 2015.

[7] N. H. A. Wahab, N. Sunar, S. H. Ariffin, K. Y. Wong, and Y. Aun, "Indoor Positioning System: A Review," *International Journal of Advanced Computer Science and Applications,* vol. 13, no. 6, 2022.

[8] J. Huang, S. Junginger, H. Liu, and K. Thurow, "Indoor Positioning Systems of Mobile Robots: A Review," *Robotics,* vol. 12, no. 2, p. 47, 2023.

[9] F. Mazhar, M. G. Khan, and B. Sällberg, "Precise indoor positioning using UWB: A review of methods, algorithms and implementations," *Wireless Personal Communications,* vol. 97, no. 3, pp. 4467-4491, 2017.

[10] X. Wang, S. Mao, S. Pandey, and P. Agrawal, "CA2T: Cooperative antenna arrays technique for pinpoint indoor localization," *Procedia computer science,* vol. 34, pp. 392-399, 2014.

[11] D. Ni, O. A. Postolache, C. Mi, M. Zhong, and Y. Wang, "UWB indoor positioning application based on Kalman filter and 3-D TOA localization algorithm," in *2019 11th International Symposium on Advanced Topics in Electrical Engineering (ATEE)*, 2019: IEEE, pp. 1-6.

[12] X. Guo, N. Ansari, F. Hu, Y. Shao, N. R. Elikplim, and L. Li, "A survey on fusion-based indoor positioning," *IEEE Communications Surveys & Tutorials,* vol. 22, no. 1, pp. 566-594, 2019.

[13] Z. Zhao, J. Fang, G. Q. Huang, and M. Zhang, "iBeacon enabled indoor positioning for warehouse management," in *2016 4th international symposium on computational and business intelligence (ISCBI)*, 2016: IEEE, pp. 21-26.

[14] Ó. Belmonte-Fernández, A. Puertas-Cabedo, J. Torres-Sospedra, R. Montoliu-Colás, and S. Trilles-Oliver, "An indoor positioning system based on wearables for ambient-assisted living," *Sensors,* vol. 17, no. 1, p. 36, 2016.

[15] T. Kim Geok *et al.*, "Review of indoor positioning: Radio wave technology," *Applied Sciences,* vol. 11, no. 1, p. 279, 2020.

[16] F. Zafari, A. Gkelias, and K. K. Leung, "A survey of indoor localization systems and technologies," *IEEE Communications Surveys & Tutorials,* vol. 21, no. 3, pp. 2568-2599, 2019.

[17] V. Malyavej, W. Kumkeaw, and M. Aorpimai, "Indoor robot localization by RSSI/IMU sensor fusion," in *2013 10th International Conference on Electrical Engineering/Electronics, Computer, Telecommunications and Information Technology*, 2013: IEEE, pp. 1-6.

[18] C. Ascher, C. Kessler, M. Wankerl, and G. F. Trommer, "Dual IMU indoor navigation with particle filter based map-matching on a smartphone," in *2010 International Conference on Indoor Positioning and Indoor Navigation*, 2010: IEEE, pp. 1-5.

[19] Y. Li and J. Ibanez-Guzman, "Lidar for autonomous driving: The principles, challenges, and trends for automotive lidar and perception systems," *IEEE Signal Processing Magazine,* vol. 37, no. 4, pp. 50-61, 2020.

[20] A. Filgueira, H. González-Jorge, S. Lagüela, L. Díaz-Vilariño, and P. Arias, "Quantifying the influence of rain in LiDAR performance," *Measurement,* vol. 95, pp. 143-148, 2017.

[21] C. Goodin, D. Carruth, M. Doude, and C. Hudson, "Predicting the Influence of Rain on LIDAR in ADAS," *Electronics,* vol. 8, no. 1, p. 89, 2019.

[22] A. M. Wallace, A. Halimi, and G. S. Buller, "Full waveform LiDAR for adverse weather conditions," *IEEE transactions on vehicular technology,* vol. 69, no. 7, pp. 7064-7077, 2020.

[23] N. Charron, S. Phillips, and S. L. Waslander, "De-noising of lidar point clouds corrupted by snowfall," in *2018 15th Conference on Computer and Robot Vision (CRV)*, 2018: IEEE, pp. 254-261.

[24] B. Jia, B. Huang, H. Gao, W. Li, and L. Hao, "Selecting critical WiFi APs for indoor localization based on a theoretical error analysis," *IEEE access,* vol. 7, pp. 36312-36321, 2019.

[25] L. Kanaris, A. Kokkinis, A. Liotta, and S. Stavrou, "Fusing bluetooth beacon data with Wi-Fi radiomaps for improved indoor localization," *Sensors,* vol. 17, no. 4, p. 812, 2017.

[26] J. Lovon-Melgarejo, M. Castillo-Cara, O. Huarcaya-Canal, L. Orozco-Barbosa, and I. Garcia-Varea, "Comparative study of supervised learning and metaheuristic algorithms for the development of bluetooth-based indoor localization mechanisms," *IEEE Access,* vol. 7, pp. 26123-26135, 2019.

[27] M. Pušnik, M. Galun, and B. Šumak, "Improved Bluetooth low energy sensor detection for indoor localization services," *Sensors,* vol. 20, no. 8, p. 2336, 2020.

[28] Y. Ma, B. Wang, S. Pei, Y. Zhang, S. Zhang, and J. Yu, "An indoor localization method based on AOA and PDOA using virtual stations in multipath and NLOS environments for passive UHF RFID," *IEEE Access,* vol. 6, pp. 31772-31782, 2018.

[29] T. Taniguchi and T. Kobayashi, "An omnidirectional and low-VSWR antenna for the FCC-approved UWB frequency band," in *IEEE Antennas and Propagation*

Society International Symposium. Digest. Held in conjunction with: USNC/CNC/URSI North American Radio Sci. Meeting (Cat. No. 03CH37450), 2003, vol. 3: IEEE, pp. 460-463.

[30] K. Kim, "Samsung expects UWB to be one of the next big wireless technologies," ed: Samsung Newsroom. URL: https://news. samsung. com/global/samsung-expects-uwb ..., 2020.

[31] D. Coppens, A. Shahid, S. Lemey, B. Van Herbruggen, C. Marshall, and E. De Poorter, "An overview of UWB standards and organizations (IEEE 802.15. 4, FiRa, Apple): Interoperability aspects and future research directions," *IEEE Access,* vol. 10, pp. 70219-70241, 2022.

[32] L. Taponecco, A. A. D'Amico, and U. Mengali, "Joint TOA and AOA estimation for UWB localization applications," *IEEE Transactions on Wireless Communications,* vol. 10, no. 7, pp. 2207-2217, 2011.

[33] R. S. Kshetrimayum, "An introduction to UWB communication systems," *Ieee Potentials,* vol. 28, no. 2, pp. 9-13, 2009.

[34] E. Novakov, "A low complexity, medium data rate, ultra-wideband communication method and system," in *2013 19th Asia-Pacific Conference on Communications (APCC)*, 2013: IEEE, pp. 26-31.

[35] M.-J. Zhao, B. Li, Z.-H. Wu, and K. Wang, "A 3–5 GHz low-power high-speed radiated power tuning UWB transmitter," *Microelectronics Journal,* vol. 44, no. 12, pp. 1358-1363, 2013.

[36] G. Caso, M. T. Le, L. De Nardis, and M.-G. Di Benedetto, "Performance comparison of WiFi and UWB fingerprinting indoor positioning systems," *Technologies,* vol. 6, no. 1, p. 14, 2018.

[37] D. Ltd., "DW1000 User Manual," ed: Decawave Ltd. Dublin, Ireland, 2015.

[38] O. Gremigni and D. Porcino, "UWB ranging performance tests in different radio environments," in *London Communications Symposium*, 2006.

[39] M. H. Kabir and R. Kohno, "A hybrid TOA-fingerprinting based localization of mobile nodes using UWB signaling for non line-of-sight conditions," *Sensors,* vol. 12, no. 8, pp. 11187-11204, 2012.

[40] T. Jia, H. Wang, X. Shen, Z. Jiang, and K. He, "Target localization based on structured total least squares with hybrid TDOA-AOA measurements," *Signal Processing,* vol. 143, pp. 211-221, 2018.

[41] H. Wu, L. Liang, X. Mei, and Y. Zhang, "A convex optimization approach for NLOS error mitigation in TOA-based localization," *IEEE Signal Processing Letters,* vol. 29, pp. 677-681, 2022.

[42] B. V. Krishnaveni, K. S. Reddy, and P. R. Reddy, "Performance comparison of TOA-based indoor positioning algorithms using ultra-wideband technology in 3D," *International Journal of Wireless and Mobile Computing,* vol. 25, no. 3, pp. 201-208, 2023.

[43] R. Zekavat and R. M. Buehrer, *Handbook of position location: Theory, practice and advances*. John Wiley & Sons, 2011.

[44] D. Dardari, A. Conti, U. Ferner, A. Giorgetti, and M. Z. Win, "Ranging with ultrawide bandwidth signals in multipath environments," *Proceedings of the IEEE,* vol. 97, no. 2, pp. 404-426, 2009.

[45] T. Wang, X. Chen, N. Ge, and Y. Pei, "Error analysis and experimental study on indoor UWB TDoA localization with reference tag," in *2013 19th Asia-Pacific Conference on Communications (APCC)*, 2013: IEEE, pp. 505-508.

[46] I. Guvenc and C.-C. Chong, "A survey on TOA based wireless localization and NLOS mitigation techniques," *IEEE Communications Surveys & Tutorials,* vol. 11, no. 3, pp. 107-124, 2009.

[47] B. Jachimczyk, D. Dziak, and W. J. Kulesza, "Using the fingerprinting method to customize RTLS based on the AoA ranging technique," *Sensors,* vol. 16, no. 6, p. 876, 2016.

[48] A. Dempster, "Dilution of precision in angle-of-arrival positioning systems," *Electronics Letters,* vol. 42, no. 5, pp. 291-292, 2006.

[49] W. Wei, X. Jin-Yu, and Z. Zhong-Liang, "A new NLOS error mitigation algorithm in location estimation," *IEEE Transactions on Vehicular Technology,* vol. 54, no. 6, pp. 2048-2053, 2005.

[50] X. Wei, N. Palleit, and T. Weber, "AOD/AOA/TOA-based 3D positioning in NLOS multipath environments," in *2011 IEEE 22nd International Symposium on Personal, Indoor and Mobile Radio Communications*, 2011: IEEE, pp. 1289-1293.

[51] C. Jiang, J. Shen, S. Chen, Y. Chen, D. Liu, and Y. Bo, "UWB NLOS/LOS classification using deep learning method," *IEEE Communications Letters,* vol. 24, no. 10, pp. 2226-2230, 2020.

[52] Q. Liu, Z. Yin, Y. Zhao, Z. Wu, and M. Wu, "UWB LOS/NLOS identification in multiple indoor environments using deep learning methods," *Physical Communication,* vol. 52, p. 101695, 2022.

[53] M. Tabaa, C. Diou, R. Saadane, and A. Dandache, "LOS/NLOS Identification based on stable distribution feature extraction and SVM classifier for UWB On-body communications," *Procedia Computer Science,* vol. 32, pp. 882-887, 2014.

[54] X. Yang, J. Wang, D. Song, B. Feng, and H. Ye, "A novel NLOS error compensation method based IMU for UWB indoor positioning system," *IEEE Sensors Journal,* vol. 21, no. 9, pp. 11203-11212, 2021.

[55] M. Si, Y. Wang, H. Siljak, C. Seow, and H. Yang, "A lightweight CIR-based CNN with MLP for NLOS/LOS identification in a UWB positioning system," *IEEE Communications Letters,* 2023.

[56] I. F. P. M. via MRMSC, "TOA based Indoor Localization and Tracking with Inaccurate Floor Plan Map via MRMSC-PHD Filter," *SENSORS,* vol. 27206, p. 1, 2019.

[57] D. T. A. Nguyen, H.-G. Lee, E.-R. Jeong, H. L. Lee, and J. Joung, "Deep learning-based localization for UWB systems," *Electronics,* vol. 9, no. 10, p. 1712, 2020.

[58] J. Wei, H. Wang, S. Su, Y. Tang, X. Guo, and X. Sun, "NLOS identification using parallel deep learning model and time-frequency information in UWB-based positioning system," *Measurement,* vol. 195, p. 111191, 2022.

[59] N. Dwek *et al.*, "Improving the accuracy and robustness of ultra-wideband localization through sensor fusion and outlier detection," *IEEE Robotics and Automation Letters,* vol. 5, no. 1, pp. 32-39, 2019.

[60] P.-C. Chen, "A non-line-of-sight error mitigation algorithm in location estimation," in *WCNC. 1999 IEEE Wireless Communications and Networking Conference (Cat. No. 99TH8466)*, 1999, vol. 1: IEEE, pp. 316-320.

[61] T. Wang, K. Hu, Z. Li, K. Lin, J. Wang, and Y. Shen, "A semi-supervised learning approach for UWB ranging error mitigation," *IEEE Wireless Communications Letters,* vol. 10, no. 3, pp. 688-691, 2020.

[62] Z. Gao, Y. Jiao, W. Yang, X. Li, and Y. Wang, "A Method for UWB Localization Based on CNN-SVM and Hybrid Locating Algorithm," *Information,* vol. 14, no. 1, p. 46, 2023.

[63] D. Feng *et al.*, "An Adaptive IMU/UWB Fusion Method for NLOS Indoor Positioning and Navigation," *IEEE Internet of Things Journal,* 2023.

[64] Z. Chen *et al.*, "Improved-UWB/LiDAR-SLAM Tightly Coupled Positioning System with NLOS Identification Using a LiDAR Point Cloud in GNSS-Denied Environments," *Remote Sensing,* vol. 14, no. 6, p. 1380, 2022.

[65] F. Liu, X. Li, J. Wang, and J. Zhang, "An adaptive UWB/MEMS-IMU complementary kalman filter for indoor location in NLOS environment," *Remote sensing,* vol. 11, no. 22, p. 2628, 2019.

[66] J. Mi, Q. Wang, and X. Han, "Constrained MEMS-Based INS/UWB Tightly Coupled System for Accurate UGVs Navigation," *Remote Sensing,* vol. 15, no. 10, p. 2535, 2023.

[67] L. Wang, S. Zhang, J. Qi, H. Chen, and R. Yuan, "Research on IMU-Assisted UWB-Based Positioning Algorithm in Underground Coal Mines," *Micromachines,* vol. 14, no. 7, p. 1481, 2023.

[68] H. Zhang *et al.*, "A Dynamic Window-Based UWB-Odometer Fusion Approach for Indoor Positioning," *IEEE Sensors Journal,* vol. 23, no. 3, pp. 2922-2931, 2022.

[69] S. A. Mohamed, M.-H. Haghbayan, T. Westerlund, J. Heikkonen, H. Tenhunen, and J. Plosila, "A survey on odometry for autonomous navigation systems," *IEEE access,* vol. 7, pp. 97466-97486, 2019.

[70] A. Jha and M. Kumar, "Two wheels differential type odometry for mobile robots," in *Proceedings of 3rd International Conference on Reliability, Infocom Technologies and Optimization*, 2014: IEEE, pp. 1-5.

[71] B. Zhou, H. Fang, and J. Xu, "Uwb-imu-odometer fusion localization scheme: Observability analysis and experiments," *IEEE Sensors Journal,* vol. 23, no. 3, pp. 2550-2564, 2022.

[72] J. Li, T. Gao, X. Wang, D. Bai, and W. Guo, "The IMU/UWB/odometer fusion positioning algorithm based on EKF," in *Journal of Physics: Conference Series*, 2022, vol. 2369, no. 1: IOP Publishing, p. 012092.

[73] M. Y. Arafat, M. M. Alam, and S. Moh, "Vision-based navigation techniques for unmanned aerial vehicles: Review and challenges," *Drones,* vol. 7, no. 2, p. 89, 2023.

[74] P.-Y. Tseng, J. J. Lin, Y.-C. Chan, and A. Y. Chen, "Real-time indoor localization with visual SLAM for in-building emergency response," *Automation in Construction,* vol. 140, p. 104319, 2022.

[75] A. Steenbeek and F. Nex, "CNN-based dense monocular visual SLAM for real-time UAV exploration in emergency conditions," *Drones,* vol. 6, no. 3, p. 79, 2022.

[76] C. Shao, L. Zhang, and W. Pan, "Faster R-CNN learning-based semantic filter for geometry estimation and its application in vSLAM systems," *IEEE Transactions on Intelligent Transportation Systems,* vol. 23, no. 6, pp. 5257-5266, 2021.

[77] D. Zhou, Y. Luo, Q. Zhang, Y. Xu, D. Chen, and X. Zhang, "A Lightweight Neural Network for Loop Closure Detection in Indoor Visual SLAM," *International Journal of Computational Intelligence Systems,* vol. 16, no. 1, pp. 1-11, 2023.

[78] J. Xu *et al.*, "Edge assisted mobile semantic visual slam," in *IEEE INFOCOM 2020-IEEE Conference on computer communications*, 2020: IEEE, pp. 1828-1837.

[79] M. Gurturk, A. Yusefi, M. F. Aslan, M. Soycan, A. Durdu, and A. Masiero, "The YTU dataset and recurrent neural network based visual-inertial odometry," *Measurement,* vol. 184, p. 109878, 2021.

[80] L. Yu, E. Yang, B. Yang, Z. Fei, and C. Niu, "A robust learned feature-based visual odometry system for UAV pose estimation in challenging indoor environments," *IEEE Transactions on Instrumentation and Measurement,* 2023.

[81] H. Lee, M. McCrink, and J. W. Gregory, "Visual-inertial odometry for unmanned aerial vehicle using deep learning," in *AIAA Scitech 2019 Forum*, 2019, p. 1410.

[82] L. Xiao, J. Wang, X. Qiu, Z. Rong, and X. Zou, "Dynamic-SLAM: Semantic monocular visual localization and mapping based on deep learning in dynamic environment," *Robotics and Autonomous Systems,* vol. 117, pp. 1-16, 2019.

[83] T. Roddick and R. Cipolla, "Predicting semantic map representations from images using pyramid occupancy networks," in *Proceedings of the IEEE/CVF Conference on Computer Vision and Pattern Recognition*, 2020, pp. 11138-11147.

[84] T. H. Nguyen, T.-M. Nguyen, and L. Xie, "Range-focused fusion of camera-IMU-UWB for accurate and drift-reduced localization," *IEEE Robotics and Automation Letters,* vol. 6, no. 2, pp. 1678-1685, 2021.

[85] B. Yang, J. Li, and H. Zhang, "Resilient indoor localization system based on UWB and visual–inertial sensors for complex environments," *IEEE Transactions on Instrumentation and Measurement,* vol. 70, pp. 1-14, 2021.

[86] H. Obeidat, W. Shuaieb, O. Obeidat, and R. Abd-Alhameed, "A review of indoor localization techniques and wireless technologies," *Wireless Personal Communications,* vol. 119, pp. 289-327, 2021.

[87] S. Monfared, T.-H. Nguyen, L. Petrillo, P. De Doncker, and F. Horlin, "Experimental demonstration of BLE transmitter positioning based on AOA estimation," in *2018 IEEE 29th Annual International Symposium on Personal, Indoor and Mobile Radio Communications (PIMRC)*, 2018: IEEE, pp. 856-859.

[88] D. Hortelano, T. Olivares, M. C. Ruiz, C. Garrido-Hidalgo, and V. López, "From sensor networks to internet of things. Bluetooth low energy, a standard for this evolution," *Sensors,* vol. 17, no. 2, p. 372, 2017.

[89] M. Jürgens *et al.*, "Bluetooth mesh networks for indoor localization," in *2019 20th IEEE International Conference on Mobile Data Management (MDM)*, 2019: IEEE, pp. 397-402.

[90] G. Kia, L. Ruotsalainen, and J. Talvitie, "Toward Accurate Indoor Positioning: An RSS-Based Fusion of UWB and Machine-Learning-Enhanced WiFi," *Sensors,* vol. 22, no. 9, p. 3204, 2022.

[91] M. Kolakowski, "Automatic radio map creation in a fingerprinting-based ble/uwb localisation system," *IET Microwaves, Antennas & Propagation,* vol. 14, no. 14, pp. 1758-1765, 2020.

[92] S. Monica and F. Bergenti, "Hybrid indoor localization using WiFi and UWB technologies," *Electronics,* vol. 8, no. 3, p. 334, 2019.

[93] A. Becker, "Kalman Filter," *Dipetik Juli,* vol. 1, p. 2020, 2018.

[94] Z. Xiang *et al.*, "Object tracking algorithm for unmanned surface vehicle based on improved mean-shift method," *International Journal of Advanced Robotic Systems,* vol. 17, no. 3, p. 1729881420925294, 2020.

[95] S. Jafarzadeh, C. Lascu, and M. S. Fadali, "State estimation of induction motor drives using the unscented Kalman filter," *IEEE Transactions on Industrial Electronics,* vol. 59, no. 11, pp. 4207-4216, 2011.

[96] I. Ullah, X. Su, J. Zhu, X. Zhang, D. Choi, and Z. Hou, "Evaluation of localization by extended Kalman filter, unscented Kalman filter, and particle filter-based techniques," *Wireless Communications and Mobile Computing,* vol. 2020, pp. 1-15, 2020.

[97] R. V. Garcia, H. K. Kuga, and M. C. F. Zanardi, "Unscented Kalman filter for determination of spacecraft attitude using different attitude parameterizations and real data," *Journal of Aerospace Technology and Management,* vol. 8, pp. 82-90, 2016.

[98] A. Giannitrapani, N. Ceccarelli, F. Scortecci, and A. Garulli, "Comparison of EKF and UKF for spacecraft localization via angle measurements," *IEEE Transactions on aerospace and electronic systems,* vol. 47, no. 1, pp. 75-84, 2011.

[99] L. D'Alfonso, A. Grano, P. Muraca, and P. Pugliese, "Extended and unscented Kalman filters in a cells-covering method for environment reconstruction," in *2019 IEEE 15th International Conference on Control and Automation (ICCA)*, 2019: IEEE, pp. 1557-1562.

[100] G. Zhu, D. Liang, Y. Liu, Q. Huang, and W. Gao, "Improving particle filter with support vector regression for efficient visual tracking," in *IEEE International Conference on Image Processing 2005*, 2005, vol. 2: IEEE, pp. II-422.

[101] D.-H. Kim and J.-Y. Pyun, "NLOS identification based UWB and PDR hybrid positioning system," *IEEE Access,* vol. 9, pp. 102917-102929, 2021.

[102] H. Zhang, Z. Zhang, N. Gao, Y. Xiao, Z. Meng, and Z. Li, "Cost-effective wearable indoor localization and motion analysis via the integration of UWB and IMU," *Sensors,* vol. 20, no. 2, p. 344, 2020.

[103] P. K. Yoon, S. Zihajehzadeh, B.-S. Kang, and E. J. Park, "Robust biomechanical model-based 3-D indoor localization and tracking method using UWB and IMU," *IEEE Sensors Journal,* vol. 17, no. 4, pp. 1084-1096, 2016.

[104] W. You, F. Li, L. Liao, and M. Huang, "Data fusion of UWB and IMU based on unscented Kalman filter for indoor localization of quadrotor UAV," *Ieee Access,* vol. 8, pp. 64971-64981, 2020.

[105] L. Marković, M. Kovač, R. Milijas, M. Car, and S. Bogdan, "Error state extended Kalman filter multi-sensor fusion for unmanned aerial vehicle localization in GPS and magnetometer denied indoor environments," in *2022 International Conference on Unmanned Aircraft Systems (ICUAS)*, 2022: IEEE, pp. 184-190.

[106] Q. Zeng, D. Liu, and C. Lv, "UWB/binocular VO fusion algorithm based on adaptive kalman filter," *Sensors,* vol. 19, no. 18, p. 4044, 2019.

[107] C.-H. Li, I. Alexander, C. Lai, and R.-B. Wu, "Accuracy enhancement of Wi-Fi positioning by ranging in dense UWB networks," *Computer Communications,* vol. 213, pp. 179-187, 2024.

[108] C. Wang, A. Xu, J. Kuang, X. Sui, Y. Hao, and X. Niu, "A high-accuracy indoor localization system and applications based on tightly coupled UWB/INS/floor map integration," *IEEE Sensors Journal,* vol. 21, no. 16, pp. 18166-18177, 2021.

[109] P. Sedlacek, M. Slanina, and P. Masek, "An overview of the IEEE 802.15. 4z standard its comparison and to the existing UWB standards," in *2019 29th International Conference Radioelektronika (RADIOELEKTRONIKA)*, 2019: IEEE, pp. 1-6.

[110] J. Park, S. Nam, H. Choi, Y. Ko, and Y.-B. Ko, "Improving deep learning-based uwb los/nlos identification with transfer learning: An empirical approach," *Electronics,* vol. 9, no. 10, p. 1714, 2020.

[111] D. Spano and F. Ricciato, "Opportunistic time-of-arrival localization in fully asynchronous wireless networks," *Pervasive and Mobile Computing,* vol. 37, pp. 139-153, 2017.

[112] R. Kaune, "Accuracy studies for TDOA and TOA localization," in *2012 15th International Conference on Information Fusion*, 2012: IEEE, pp. 408-415.

[113] K. Yu, K. Wen, Y. Li, S. Zhang, and K. Zhang, "A novel NLOS mitigation algorithm for UWB localization in harsh indoor environments," *IEEE Transactions on Vehicular Technology,* vol. 68, no. 1, pp. 686-699, 2018.

[114] Z. Cui, Y. Gao, J. Hu, S. Tian, and J. Cheng, "LOS/NLOS identification for indoor UWB positioning based on Morlet wavelet transform and convolutional neural networks," *IEEE Communications Letters,* vol. 25, no. 3, pp. 879-882, 2020.

[115] K. Wen, K. Yu, and Y. Li, "NLOS identification and compensation for UWB ranging based on obstruction classification," in *2017 25th European signal processing conference (EUSIPCO)*, 2017: IEEE, pp. 2704-2708.

[116] M. Dong, "A Low-Cost NLOS Identification and Mitigation Method for UWB Ranging in Static and Dynamic Environments," *IEEE Communications Letters,* vol. 25, no. 7, pp. 2420-2424, 2021.

[117] S. Tiwari, D. Wang, M. Fattouche, and F. Ghannouchi, "A hybrid RSS/TOA method for 3D positioning in an indoor environment," *International Scholarly Research Notices,* vol. 2012, 2012.

[118] P. Zuo, H. Zhang, C. Wang, H. Jiang, and B. Pan, "Directional Target Localization in NLOS Environments Using RSS-TOA Combined Measurements," *IEEE Wireless Communications Letters,* vol. 10, no. 11, pp. 2602-2606, 2021.

[119] Y. Liu, "UWB ranging error analysis based on TOA mode," in *Journal of Physics: Conference Series*, 2021, vol. 1939, no. 1: IOP Publishing, p. 012124.

[120] H. Lu, T. Wang, F. Ge, and Y. Shen, "A robust UWB array localization scheme through passive anchor assistance," *China Communications,* vol. 18, no. 4, pp. 1-13, 2021.

[121] F. Zhang, L. Yang, Y. Liu, Y. Ding, S.-H. Yang, and H. Li, "Design and Implementation of Real-Time Localization System (RTLS) Based on UWB and TDoA Algorithm," *Sensors,* vol. 22, no. 12, p. 4353, 2022.

[122] W. Chen, "Personnel precise positioning system of coal mine underground based on UWB," in *Journal of Physics: Conference Series*, 2021, vol. 1920, no. 1: IOP Publishing, p. 012115.

[123] A. R. J. Ruiz and F. S. Granja, "Comparing ubisense, bespoon, and decawave uwb location systems: Indoor performance analysis," *IEEE Transactions on instrumentation and Measurement,* vol. 66, no. 8, pp. 2106-2117, 2017.

[124] V. Rayavarapu and A. Mahapatro, "NLOS identification and mitigation in UWB positioning with bagging-based ensembled classifiers," *Annals of Telecommunications,* vol. 77, no. 5, pp. 267-280, 2022.

[125] X. Yang, F. Zhao, and T. Chen, "NLOS identification for UWB localization based on import vector machine," *AEU-International Journal of Electronics and Communications,* vol. 87, pp. 128-133, 2018.

[126] F. Molina Martel, J. Sidorenko, C. Bodensteiner, M. Arens, and U. Hugentobler, "Unique 4-DOF relative pose estimation with six distances for UWB/V-SLAM-based devices," *Sensors,* vol. 19, no. 20, p. 4366, 2019.

[127] N. Zhou, L. Lau, R. Bai, and T. Moore, "Novel prior position determination approaches in particle filter for ultra wideband (UWB)-based indoor positioning," *NAVIGATION: Journal of the Institute of Navigation,* vol. 68, no. 2, pp. 277-292, 2021.

[128] S. Wang, S. Wang, W. Liu, and Y. Tian, "A study on the optimization nodes arrangement in UWB localization," *Measurement,* vol. 163, p. 108056, 2020.

[129] H. Pan, X. Qi, M. Liu, and L. Liu, "Map-aided and UWB-based anchor placement method in indoor localization," *Neural Computing and Applications,* vol. 33, no. 18, pp. 11845-11859, 2021.

[130] X. Kong, L. Liu, T. P. Tran, and K. Sandrasegaran, "Analysis of stakeholder concerns for vehicle navigation system architecture solution," in *2014 IEEE Fifth International Conference on Communicatiosn and Electronics (ICCE)*, 2014: Thomson Reuters.

[131] X. Zhu, J. Yi, J. Cheng, and L. He, "Adapted error map based mobile robot UWB indoor positioning," *IEEE Transactions on Instrumentation and Measurement,* vol. 69, no. 9, pp. 6336-6350, 2020.

[132] H. Zhang, Q. Wang, J. Xu, Z. Li, and Y. Yang, "Time delay characteristics analysis of UWB diffraction propagation in indoor NLOS environment," *IEEE Communications Letters,* 2022.

[133] J. Li, T. Gao, X. Wang, W. Guo, and D. Bai, "Study on the UWB location algorithm in the NLOS environment," in *Journal of Physics: Conference Series*, 2022, vol. 2400, no. 1: IOP Publishing, p. 012043.

[134] C. Chen, Z. Huang, J. Wang, L. Yuan, J. Bao, and Z. Chen, "Channel-quality-evaluation-based anchor node selection for uwb indoor positioning," *Electronics,* vol. 11, no. 3, p. 436, 2022.

[135] W. P. Cully, S. L. Cotton, W. G. Scanlon, and J. McQuiston, "Body shadowing mitigation using differentiated LOS/NLOS channel models for RSSI-based Monte Carlo personnel localization," in *2012 IEEE Wireless Communications and Networking Conference (WCNC)*, 2012: IEEE, pp. 694-698.

[136] A. G. Ferreira, D. Fernandes, S. Branco, A. P. Catarino, and J. L. Monteiro, "Feature selection for real-time NLOS identification and mitigation for body-mounted UWB transceivers," *IEEE Transactions on Instrumentation and Measurement,* vol. 70, pp. 1-10, 2021.

[137] G. Moro, F. Di Luca, D. Dardari, and G. Frisoni, "Human Being Detection from UWB NLOS Signals: Accuracy and Generality of Advanced Machine Learning Models," *Sensors,* vol. 22, no. 4, p. 1656, 2022.

[138] R. Bharadwaj, A. Alomainy, and S. K. Koul, "Experimental investigation of body-centric indoor localization using compact wearable antennas and machine learning algorithms," *IEEE Transactions on Antennas and Propagation,* vol. 70, no. 2, pp. 1344-1354, 2021.

[139] A. Musa, G. D. Nugraha, H. Han, D. Choi, S. Seo, and J. Kim, "A decision tree-based NLOS detection method for the UWB indoor location tracking accuracy improvement," *International Journal of Communication Systems,* vol. 32, no. 13, p. e3997, 2019.

[140] D.-H. Kim, A. Farhad, and J.-Y. Pyun, "UWB positioning system based on LSTM classification with mitigated NLOS effects," *IEEE Internet of Things Journal,* 2022.

[141] K. Dineva and T. Atanasova, "SYSTEMATIC LOOK AT MACHINE LEARNING ALGORITHMS–ADVANTAGES, DISADVANTAGES AND PRACTICAL APPLICATIONS," *International Multidisciplinary Scientific GeoConference: SGEM,* vol. 20, no. 2.1, pp. 317-324, 2020.

[142] P. Peng, C. Yu, Q. Xia, Z. Zheng, K. Zhao, and W. Chen, "An indoor positioning method based on UWB and visual fusion," *Sensors,* vol. 22, no. 4, p. 1394, 2022.

[143] Y. Sun, L. Guan, Z. Chang, C. Li, and Y. Gao, "Design of a low-cost indoor navigation system for food delivery robot based on multi-sensor information fusion," *Sensors,* vol. 19, no. 22, p. 4980, 2019.

[144] Z. Chen, A. Xu, X. Sui, Y. Hao, C. Zhang, and Z. Shi, "NLOS Identification-and Correction-Focused Fusion of UWB and LiDAR-SLAM Based on Factor Graph Optimization for High-Precision Positioning with Reduced Drift," *Remote Sensing,* vol. 14, no. 17, p. 4258, 2022.

[145] B. Venkata Krishnaveni and S. Reddy, "Indoor Tracking by Adding IMU and UWB using Unscented Kalman Filter."
[146] L. Jia, Y. Wang, L. Ma, Z. He, Z. Li, and Y. Cui, "Integrated Positioning System of Kiwifruit Orchard Mobile Robot Based on UWB/LiDAR/ODOM," *Sensors,* vol. 23, no. 17, p. 7570, 2023.
[147] C. Tang, C. He, and L. Dou, "An imu/odm/uwb joint localization system based on modified cubature kalman filtering," *Sensors,* vol. 21, no. 14, p. 4823, 2021.
[148] K. Naheem and M. S. Kim, "A low-cost foot-placed UWB and IMU fusion-based indoor pedestrian tracking system for IoT applications," *Sensors,* vol. 22, no. 21, p. 8160, 2022.
[149] D. Mújica-Vargas, V. Vela-Rincón, A. Luna-Álvarez, A. Rendón-Castro, M. Matuz-Cruz, and J. Rubio, "Navigation of a Differential Wheeled Robot Based on a Type-2 Fuzzy Inference Tree," *Machines,* vol. 10, no. 8, p. 660, 2022.
[150] Z. Wang, J. Tan, and Z. Sun, "Error factor and mathematical model of positioning with odometer wheel," *Advances in Mechanical Engineering,* vol. 7, no. 1, p. 305981, 2015.
[151] J. Tiemann, L. Koring, P. Gorczak, and C. Wietfeld, "Improving the robustness of control-grade ultra-wideband localization," *IFAC-PapersOnLine,* vol. 51, no. 10, pp. 103-108, 2018.
[152] A. Umek and A. Kos, "Validation of UWB positioning systems for player tracking in tennis," *Personal and Ubiquitous Computing,* pp. 1-11, 2020.
[153] Z. Wei, R. Jiang, X. Wei, Y.-A. Cheng, L. Cheng, and C. Wang, "Novel indoor positioning system based on ultra-wide bandwidth," *Visual Computing for Industry, Biomedicine, and Art,* vol. 3, no. 1, pp. 1-6, 2020.
[154] T. Polonelli, Y. Qin, E. M. Yeatman, L. Benini, and D. Boyle, "A flexible, low-power platform for uav-based data collection from remote sensors," *IEEE Access,* vol. 8, pp. 164775-164785, 2020.
[155] H. Yao, X. Wang, H. Qi, and X. Liang, "Tightly Coupled Indoor Positioning Using Uwb/mmwave Radar/imu," *The International Archives of the Photogrammetry, Remote Sensing and Spatial Information Sciences,* vol. 46, pp. 323-329, 2022.
[156] A. Poulose, O. S. Eyobu, M. Kim, and D. S. Han, "Localization error analysis of indoor positioning system based on UWB measurements," in *2019 Eleventh International Conference on Ubiquitous and Future Networks (ICUFN)*, 2019: IEEE, pp. 84-88.
[157] W. Sun, M. Xue, H. Yu, H. Tang, and A. Lin, "Augmentation of fingerprints for indoor WiFi localization based on Gaussian process regression," *IEEE Transactions on Vehicular Technology,* vol. 67, no. 11, pp. 10896-10905, 2018.
[158] Z. Jianyong, L. Haiyong, C. Zili, and L. Zhaohui, "RSSI based Bluetooth low energy indoor positioning," in *2014 International Conference on Indoor Positioning and Indoor Navigation (IPIN)*, 2014: IEEE, pp. 526-533.
[159] Y.-C. Pu and P.-C. You, "Indoor positioning system based on BLE location fingerprinting with classification approach," *Applied Mathematical Modelling,* vol. 62, pp. 654-663, 2018.

[160] A. A. Kalbandhe and S. C. Patil, "Indoor positioning system using bluetooth low energy," in *2016 International Conference on Computing, Analytics and Security Trends (CAST)*, 2016: IEEE, pp. 451-455.

[161] N. Bai, Y. Tian, Y. Liu, Z. Yuan, Z. Xiao, and J. Zhou, "A high-precision and low-cost IMU-based indoor pedestrian positioning technique," *IEEE Sensors Journal,* vol. 20, no. 12, pp. 6716-6726, 2020.

[162] J. Li, W. Gao, Y. Wu, Y. Liu, and Y. Shen, "High-quality indoor scene 3D reconstruction with RGB-D cameras: A brief review," *Computational Visual Media,* vol. 8, no. 3, pp. 369-393, 2022.

[163] S. Karam, V. Lehtola, and G. Vosselman, "Strategies to integrate IMU and LiDAR SLAM for indoor mapping," *ISPRS Annals of the Photogrammetry, Remote Sensing and Spatial Information Sciences,* vol. 1, pp. 223-230, 2020.

[164] L. Chen, L. Pei, H. Kuusniemi, Y. Chen, T. Kröger, and R. Chen, "Bayesian fusion for indoor positioning using bluetooth fingerprints," *Wireless personal communications,* vol. 70, pp. 1735-1745, 2013.

[165] M. Bullmann, T. Fetzer, F. Ebner, M. Ebner, F. Deinzer, and M. Grzegorzek, "Comparison of 2.4 GHz WiFi FTM-and RSSI-based indoor positioning methods in realistic scenarios," *Sensors,* vol. 20, no. 16, p. 4515, 2020.

[166] X. Song *et al.*, "A novel convolutional neural network based indoor localization framework with WiFi fingerprinting," *IEEE Access,* vol. 7, pp. 110698-110709, 2019.

[167] T. Xie, H. Jiang, X. Zhao, and C. Zhang, "A Wi-Fi-based wireless indoor position sensing system with multipath interference mitigation," *Sensors,* vol. 19, no. 18, p. 3983, 2019.

[168] H. Sun, L. G. Chia, and S. G. Razul, "Through-wall human sensing with WiFi passive radar," *IEEE Transactions on Aerospace and Electronic Systems,* vol. 57, no. 4, pp. 2135-2148, 2021.

[169] M. Dong, Y. Qi, X. Wang, and Y. Liu, "A non-line-of-sight mitigation method for indoor ultra-wideband localization with multiple walls," *IEEE Transactions on Industrial Informatics,* 2022.

[170] S. Gezici *et al.*, "Localization via ultra-wideband radios: a look at positioning aspects for future sensor networks," *IEEE signal processing magazine,* vol. 22, no. 4, pp. 70-84, 2005.

[171] W. Wang, J. Huang, S. Cai, and J. Yang, "Design and implementation of synchronization-free TDOA localization system based on UWB," *Radioengineering,* vol. 27, no. 1, pp. 320-330, 2019.

[172] J. B. Kristensen, M. M. Ginard, O. K. Jensen, and M. Shen, "Non-line-of-sight identification for UWB indoor positioning systems using support vector machines," in *2019 IEEE MTT-S International Wireless Symposium (IWS)*, 2019: IEEE, pp. 1-3.

[173] M. Stahlke, S. Kram, C. Mutschler, and T. Mahr, "NLOS detection using UWB channel impulse responses and convolutional neural networks," in *2020 International Conference on Localization and GNSS (ICL-GNSS)*, 2020: IEEE, pp. 1-6.

[174] F. Shaheen, B. Verma, and M. Asafuddoula, "Impact of automatic feature extraction in deep learning architecture," in *2016 International conference on digital image computing: techniques and applications (DICTA)*, 2016: IEEE, pp. 1-8.

[175] T. Feigl, T. Nowak, M. Philippsen, T. Edelhäußer, and C. Mutschler, "Recurrent neural networks on drifting time-of-flight measurements," in *2018 International Conference on Indoor Positioning and Indoor Navigation (IPIN)*, 2018: IEEE, pp. 206-212.

[176] B. Li, Z. Hao, and X. Dang, "An indoor location algorithm based on Kalman filter fusion of ultra-wide band and inertial measurement unit," *AIP Advances,* vol. 9, no. 8, 2019.

[177] D. Feng, C. Wang, C. He, Y. Zhuang, and X.-G. Xia, "Kalman-filter-based integration of IMU and UWB for high-accuracy indoor positioning and navigation," *IEEE Internet of Things Journal,* vol. 7, no. 4, pp. 3133-3146, 2020.

[178] D. Yuan, J. Zhang, J. Wang, X. Cui, F. Liu, and Y. Zhang, "Robustly adaptive EKF PDR/UWB integrated navigation based on additional heading constraint," *Sensors,* vol. 21, no. 13, p. 4390, 2021.

[179] M. Kolakowski, "Comparison of Extended and Unscented Kalman Filters Performance in a Hybrid BLE-UWB Localization System," in *2020 23rd International Microwave and Radar Conference (MIKON)*, 2020: IEEE, pp. 122-126.

[180] B. Gao, G. Hu, Y. Zhong, and X. Zhu, "Cubature Kalman filter with both adaptability and robustness for tightly-coupled GNSS/INS integration," *IEEE Sensors Journal,* vol. 21, no. 13, pp. 14997-15011, 2021.

[181] Z. Long, Y. Xiang, X. Lei, Y. Li, Z. Hu, and X. Dai, "Integrated indoor positioning system of greenhouse robot based on UWB/IMU/ODOM/LIDAR," *Sensors,* vol. 22, no. 13, p. 4819, 2022.

[182] A. Liu, S. Lin, J. Wang, and X. Kong, "A Succinct Method for Non-Line-of-Sight Mitigation for Ultra-Wideband Indoor Positioning System," *Sensors,* vol. 22, no. 21, p. 8247, 2022.

[183] C. Hu, P. Huang, and W. Wang, "Tightly Coupled Visual-Inertial-UWB Indoor Localization System with Multiple Position-Unknown Anchors," *IEEE Robotics and Automation Letters,* 2023.

[184] S. Zheng, Z. Li, Y. Liu, H. Zhang, and X. Zou, "An optimization-based UWB-IMU fusion framework for UGV," *IEEE Sensors Journal,* vol. 22, no. 5, pp. 4369-4377, 2022.

[185] J. Feng, L. Wang, J. Li, Y. Xu, S. Bi, and T. Shen, "Novel LiDAR-assisted UWB positioning compensation for indoor robot localization," in *2021 International Conference on Advanced Mechatronic Systems (ICAMechS)*, 2021: IEEE, pp. 215-219.

[186] F. Liu, J. Zhang, J. Wang, H. Han, and D. Yang, "An UWB/vision fusion scheme for determining pedestrians' indoor location," *Sensors,* vol. 20, no. 4, p. 1139, 2020.